Novel Antiferromagnetic Materials

John Sinclair

Doctor of Philosophy

University Of York
Physics

August 2018

Abstract

There is intense interest in new antiferromagnetic materials due to the development of antiferromagnetic spintronics. Currently, the material IrMn is used, however, Iridium is one of the scarcest and most expensive elements. In this work, a number of novel, thin film antiferromagnetic materials were produced using sputter deposition and then assessed using magnetic and structural characterisation techniques as well as a temperature dependent resistivity technique developed during the project. Initially work was focussed on the ternary Heusler alloys Ni_2MnAl and Ru_2MnGe. Both alloys were shown to crystallise in their predicted antiferromagnetic phases, however they had low thermal stability due to limited magnetocrystalline anisotropy. Ru_2MnGe was demonstrated to be the superior alloy, due to the anisotropy generated by its (111) sheet antiferromagnetic spin structure allowing the median blocking temperature to be determined for a Ru_2MnGe (30 nm) / CoFe (2.5 nm) sample as $T_B = (126 \pm 3)$ K.

Subsequent work focussed on the compound MnN. Using similar growth and measurement techniques, MnN thin films were shown to have a median blocking temperature as high as (374 ± 4) K and an effective anisotropy constant up to 6.6×10^6 ergs/cm^3. These values indicate MnN may have the potential to be integrated into spintronic devices, if it is possible to reduce the antiferromagnet layer thickness, whilst maintaining the stoichiometry and tetragonal distortion.

Contents

List of Tables

List of Figures

Acknowledgements

This thesis and the work within it would never have been possible without the help and support of many people. First, I would like to acknowledge my supervisors Prof. Kevin O'Grady and Prof. Atsufumi Hirohata as well as Dr. Gonzalo Vallejo Fernandez. Their guidance, help and support has made this possible.

Additionally I'd like to thank research collaborators and both Bielefeld and Tohoku Universities for their contributions towards, and discussions of the research presented in this thesis, which have been invaluable.

There are too many to name individually, but I'd like to sincerely thank all the members of the magnetism group based in A/O/12 without whom, the last three years would not have been nearly as enjoyable. A special mention to William Frost whom I have had to put up with for the entirety of my study here. I wish you all the best with your future work!

Finally I'd like to thank my parents, for without them, none of this would have been possible.

Declaration

I declare that the work presented in this thesis is based purely on my own research, unless otherwise stated and properly referenced, and has not been submitted for a degree in this or any other university.

Signed:

John Sinclair

August 2018

Chapter 1: Introduction

Since the discovery of giant magnetoresistance (GMR) by Fert and Grünberg in 1988 [1, 2] the field of spin transport electronics or 'spintronics' has been subject to considerable research and commercial interest. Antiferromagnetic materials play a large role in this field, they are primarily used to fix the orientation of a neighbouring ferromagnetic layer in thin film devices through exchange bias. This makes them critical to the production of magnetic sensors used in data storage. More recently, antiferromagnets have been applied to next-generation spintronic devices due their resistance to perturbation from external magnetic fields, lack of any stray and therefore demagnetising fields, ultrafast dynamics and generation of large magneto-transport effects [3].

Currently, the antiferromagnet used for many of these applications is IrMn. However the metal Iridium is one of the scarcest elements on the planet [3], meaning that there is significant demand to replace this material with a lower cost alternative so that production does not depend on any critical resources. In this work, the current state of field and required physical properties for materials with the potential to replace IrMn are examined in detail. Following on from this, the characterisation methods for antiferromagnetic materials are described and developed. Finally a number of novel antiferromagnetic materials are characterised using a variety of structural and magnetic measurement techniques and their applicability to the field of spintronics is discussed.

1.1 Exchange Interactions

The physical origin of magnetic ordering in materials was not well understood until after the combination of Heisenberg's theory of quantum mechanics (1927) with the earlier molecular field theory postulated by Weiss (1907). First considering a pair of atoms, there are a number of classical attractive and repulsive electrostatic forces present between the constituent protons and electrons of the atoms. The direction and magnitude of these forces can be calculated using Coulomb's law. In addition to these forces, there is a non-classical force that is dependent on the relative orientation of the electron spins. This force, called the exchange force, is a consequence of the Pauli Exclusion Principle, which states that two electron

orbitals of equal energy cannot occupy the same location if they have equal spin. Initially, considering a hydrogen molecule, this means that if the spins are parallel, the exchange force is repulsive, whereas if they are antiparallel it is attractive, leading to the formation of a stable molecule. The effect of this force on formation can be expressed as the exchange energy. For two atoms i and j with spin angular momentum $S_i\hbar$ and $S_j\hbar$ the exchange energy (E_{ex}) between them is given by:

$$E_{ex} = -2J_{ex}\,\overrightarrow{S_i}\,\overrightarrow{S_j} = -2J_{ex}\,S_iS_j\cos\theta_{ij} \tag{1.1}$$

where J_{ex} is the exchange integral and θ_{ij} is the angle between the spins [4]. If J_{ex} is positive then E_{ex} is at a minimum when the spins are parallel ($\cos\theta_{ij} = 1$), if J_{ex} is negative then exchange energy is minimised by an antiparallel spin arrangement ($\cos\theta_{ij} = -1$). These spin orientations result in ferromagnetic and antiferromagnetic order respectively. Equation 1.1 however only applies to a two atom system. In order to extend this, it must be summed over all atom pairs within a material. Only considering nearest neighbour pairs, due to the short range of the exchange force, results in a Hamiltonian of the form:

$$\langle H\rangle = -2\,J_{ex}\sum_{i>j}\overrightarrow{S_i}\,\overrightarrow{S_j} \tag{1.2}$$

Figure 1.1 shows the variation of J_{ex} as a function of the ratio r_a/r_{3d} where r_a is the atomic radius and $r_{3d}$is the radius of the 3d electron shell. The spacing between the atoms is taken to be the atomic diameter ($2r_a$), this relationship is known as the Bethe-Slater curve.

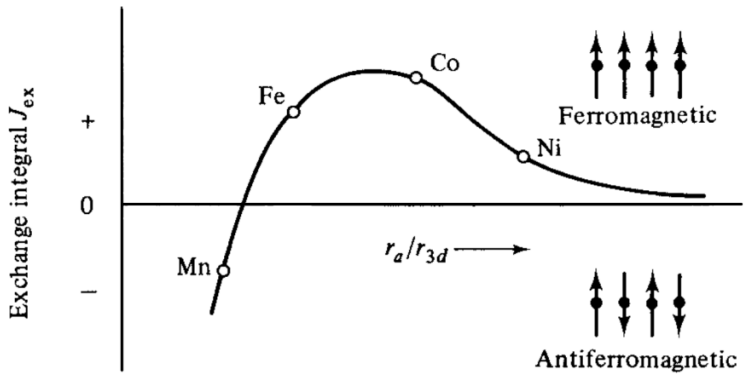

Figure 1.1 - Schematic diagram of the Bethe-Slater curve [4].

When the ratio r_a/r_{3d} is large, the exchange integral is small and positive. As the atoms are brought closer together, the ratio r_a/r_{3d}will decrease and the 3d electrons approach each

other, giving an enhancement in the positive exchange interaction causing strong ferromagnetic ordering. Further reduction in the atomic spacing begins to cause overlap of the 3d electron shells, meaning that their spins must become antiparallel to avoid violating the Pauli Exclusion Principle, in turn, leading to antiferromagnetic order [4].

The positions of the four elements Mn, Fe, Co and Ni are labelled in Figure 1.1, since these four elements have the highest individual magnetic moments of all of the elements. As a result, at least one of these atoms is present in almost all common magnetic alloys and compounds. On further inspection of Figure 1.1, it is clear that materials with a r_a/r_{3d} ratio between those of Mn and Fe will experience a large change in the value of the exchange integral for a small change in lattice spacing.

This relationship explains how, when metals are alloyed together, the resulting alloy can have magnetic ordering different to any of the constituent elements. For example, many of the Mn-based ternary Heusler alloys exhibit ferromagnetic and antiferromagnetic order, when the spacing between the Mn atoms is varied by control of the crystal structure.

Longer-range exchange interactions including indirect exchange and superexchange, are explored in chapter 2 in the context of classical antiferromagnetic materials.

1.2 HARFIR Project

The majority of work presented in this thesis was done as part of the joint EU/JST Heusler Alloy Replacement for Iridium (HARFIR) project. This project was a collaboration between 6 institutions using both theoretical and experimental approaches to discover and refine antiferromagnetic alloys which do not contain the rare earth metal Iridium. These institutions were: The University of York, The University of Bielefeld, The University of Konstanz, Budapest University of Technology and Economics, Tohoku University and KEK High Energy Accelerator Research Organisation.

In magnetic data storage, an antiferromagnetic layer is used to pin the orientation of a neighbouring ferromagnetic layer to produce a spin-valve type device. These devices have a resistance that is dependent on an applied magnetic field. Modern tunnelling magneto-resistance (TMR) devices can exhibit changes in resistance in excess of 600% at room temperature [5]. Furthermore, antiferromagnetic layers also have been found to induce a

spin-polarised electric current leading to their application in many next generation spintronic devices [6].

Currently, the antiferromagnet IrMn is used in all hard disk drive (HDD) read heads [7] and many prototypes of next generation solid state magnetic random access memory (MRAM) [8]. Unfortunately, Iridium is one of the most scarce elements (~10^{-3} ppm [9]) in the earth's crust and has been repeatedly identified by the European Commission as a critical raw material [3]. This means the price of Ir is highly volatile and due to increasing demand has almost tripled in the last two years alone. Figure 1.2 shows both the volatility and increase in the price of Iridium in recent years.

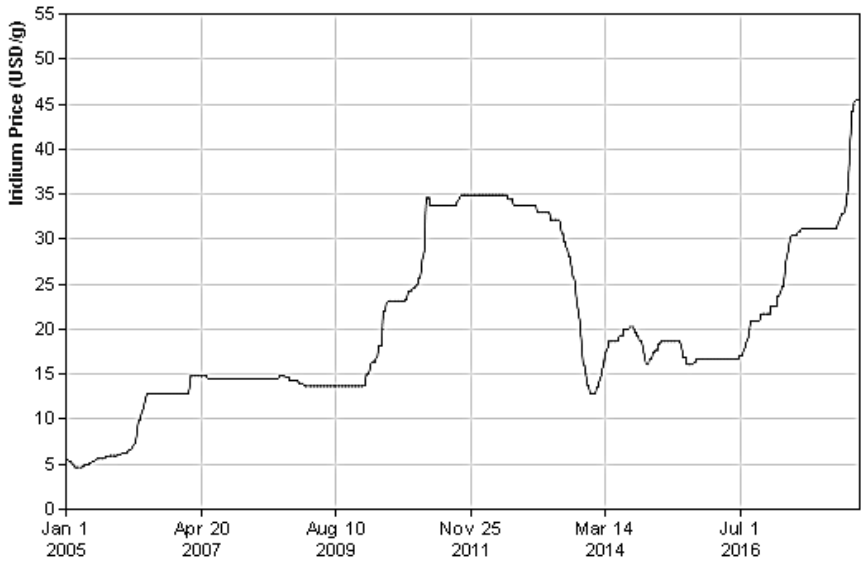

Figure 1.2 - Average price of Ir (USD/g) between 2005 and 2018 [10].

The HARFIR research programme aimed to reduce the cost of future spintronic devices by exploring whether the replacement of the antiferromagnetic alloy IrMn with a ternary Heusler alloy could result in materials with equal or improved antiferromagnetic properties. This was realised by the growth and characterisation of both polycrystalline and epitaxial Heusler alloy thin films. These films were characterised structurally using synchrotron beamlines, high resolution electron microscopy and X-ray diffraction and characterised magnetically using sensitive electrical and magnetic measurement facilities available within the HARFIR partner institutions.

1.3 Requirements for an IrMn Replacement

Just as with Moore's Law [11], which describes the exponential increase in the number of transistors in integrated circuits with time, the demand for and consequently the density of digital data storage has also been increasing exponentially over the last 30 years as shown in Figure 1.3. This rapid increase in storage density, to over 1.3 Tbit/in^2 [12], has necessitated a decrease in bit size to sub 10 nm lateral diameter in the case of HDDs. This introduces technical challenges in both the thermal stability of the bit and the accurate reading and writing of data.

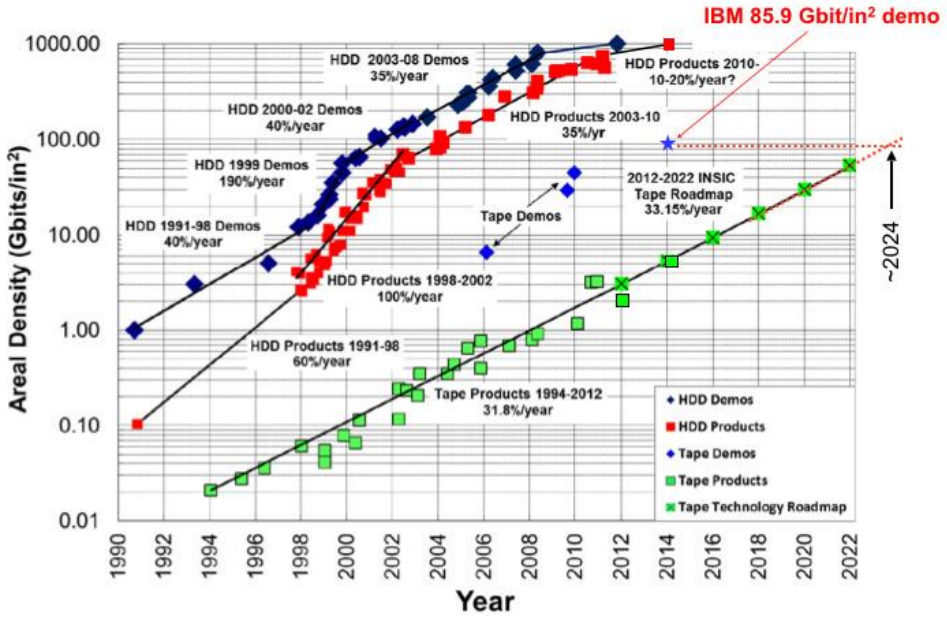

Figure 1.3 - Increase in areal bit density in magnetic HDD and tape storage over the last 30 years [13].

Currently IrMn is the only antiferromagnetic material that has sufficient thermal stability and exchange coupling to neighbouring ferromagnetic layers to allow the production of magnetic sensors capable of reading back the change in magnetisation observed between bits in modern hard drives.

Any potential replacement for IrMn would need to demonstrate room temperature exchange bias in excess of 1 kOe, with a blocking temperature above 380 K in thin film form and with a layer thickness below 10 nm. To effectively search for Heusler alloys that might meet these criteria, a comprehensive literature review and theoretical work were undertaken by the

HARFIR partner institutions to shortlist potential candidate materials with predicted antiferromagnetic ground-states at room temperature.

1.4 Potential Novel Antiferromagnetic Materials

Antiferromagnetic materials have been subject to intense research for the last 60 years [14]. In this time several types of antiferromagnetic materials have been identified. These include: metallic alloys, transition metal oxides and more recently semi-metallic compounds and synthetic antiferromagnets. The variation of properties and exchange coupling mechanisms in these materials are discussed in detail in chapter 2. This work focuses on two types of materials:

1. Ternary Heusler alloys with the structure X_2YZ, where elements X and Y are transition metals, and Z is a metalloid or non-metal [15]. This group contains thousands of alloys with diverse magnetic properties, many with predicted antiferromagnetic or ferrimagnetic ordering. For this reason, the Heusler alloys were chosen as the primary source of candidate materials for the HARFIR project.
2. The compound manganese nitride (MnN) which, exists in a wide variety of phases, depending on its stoichiometry [16]. The magnetic ordering in MnN was first measured using neutron powder diffraction [17, 18] and showed antiferromagnetic order in the equiatomic θ-phase MnN. New interest in the material was generated after work from Meinert et al. in 2015 showed polycrystalline MnN films could be used to generate exchange bias effects in excess of 1 kOe at room temperature.

1.5 Notes on the Thesis

For much of the background theoretical work presented in this thesis, the textbooks on magnetic materials by B.D. Cullity [4] and R. O'Handley [19] have provided the primary source of information. To prevent repeatedly referencing these texts it can be assumed that where no direct reference is given, the information may be found in these books. As the Gaussian cgs (centimetre gram second) unit system is widely used by the magnetic recording industry and applied magnetism research community it was deemed appropriate to use in the majority of this work.

Chapter 2: Classical Antiferromagnets

An antiferromagnet is defined as a material with an antiparallel arrangement of strongly coupled atomic dipoles. Néel originally developed the theory of antiferromagnetism in a series of papers starting in 1932 [20] in which he applied Weiss' molecular field theory to the problem. He envisaged an antiferromagnetic (AF) material as being composed of two equal sublattices arranged antiparallel to each other, resulting in a material with no net magnetic moment. Since Néel's initial hypothesis, the term antiferromagnetism has been extended to include materials with more complex spin arrangements. These can contain more than two sublattices with spiral, canted or triangular spin arrangements [19]. Figure 2.1 shows one of the simplest spin arrangements possible in an antiferromagnet. This arrangement is known as a sheet antiferromagnet due to atoms from each of the sublattices being arranged in a layered structure.

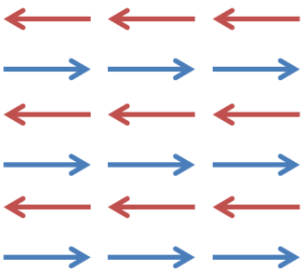

Figure 2.1 - Alignment of spins in an AF material with two equal sublattices.

As antiferromagnetic materials do not have any net moment, direct measurement of their magnetic properties is difficult. Initially, the first antiferromagnetic materials were only characterised by their susceptibility. Using molecular field theory, it was possible to predict the temperature variation of susceptibility of an antiferromagnet above the ordering (Néel) temperature (T_N). Agreement between experimental and theoretical susceptibility data lead to MnO being recognised as antiferromagnetic materials in 1938 [21]. It was not until the development of neutron diffraction, that the first direct measurements of the spin structure of AF materials were possible. In 1949, it was shown that MnO consisted of two Mn ion sublattices with an antiparallel spin arrangement [22], confirming Néel's initial hypothesis. Methods of measurement of magnetic properties of antiferromagnetic materials, including:

magnetometry, neutron scattering, polarised neutron reflectometry, X-ray magnetic dichroism and magneto-optical imaging techniques are discussed later in this chapter.

Initially after their discovery, antiferromagnets saw no application until the discovery of exchange bias by Mieklejohn and Bean in 1956 [23, 24]. However, even after this discovery, they remained a scientific curiosity for many years, until finding widespread use in the read heads of hard drives after the shift from anisotropic magneto-resistance (AMR) heads to GMR heads in the late 1990s [25]. More recently antiferromagnetic materials are of increased interest due to solid state spintronics [14]. This more recent use in information technology has prompted considerable theoretical and experimental research into antiferromagnetic materials and exchange coupling.

2.1 Temperature Dependence of Magnetism

To understand the temperature-dependent properties of an antiferromagnetic material it is first necessary to understand the properties of each of the constituent quasi-ferromagnetic sublattices. The magnetic moment of a ferromagnetic material is generated by the alignment of the atomic spins within it. A perfectly aligned spin structure as shown in Figure 2.2 is only achievable at $T = 0$ K where no thermal effects are present. As temperature is increased, thermal energy allows fluctuations of the spins away from perfect parallel alignment. Above a critical temperature, the magnetic order of the material will vanish. This temperature is called the Curie temperature (T_C).

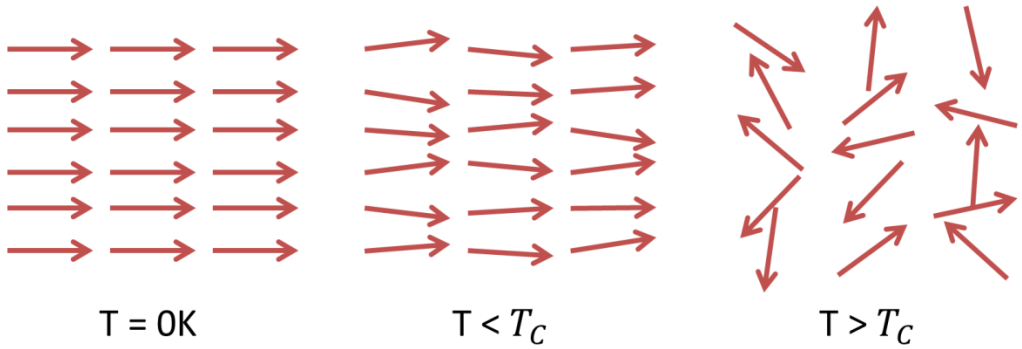

Figure 2.2 - Alignment of spins in a ferromagnetic material at 0 K, below the Curie temperature, and above the Curie temperature.

This type of behaviour is predicted by Curie's law, which is based on the Langevin theory of paramagnetism. This theory relies on the assumption that the individual atomic spins do not interact with each other. This has been shown not to be true. In 1907 Weiss proposed that

there were interactions between neighbouring spins which could be represented by a fictitious internal field called the molecular field H_m [26]. Weiss proposed the intensity of this field was directly proportional to the magnetisation:

$$H_m = \gamma_m M \tag{2.1}$$

where γ_m is the molecular field constant and M is the magnetisation. For ferromagnetic materials, the value of this constant must be high, to account for a significant proportion of the observed saturation at room temperature. This effect is clearly not magnetic, as the magnitude of the molecular field is orders of magnitude higher than any magnetic field produced. For example in iron, the molecular field is found to be $\approx 10^6$ Oe [19]. The origin of this field was not explained until Heisenberg introduced the concept of exchange interactions in 1928 [27]. This molecular field works in addition to the applied field *H*, by combination with Curie's Law:

$$\chi_m = \frac{M}{DH} = \frac{C}{T} \tag{2.2}$$

where χ_m is the mass susceptibility, D is the density and C is the Curie constant. Thus, the magnetic susceptibility (χ_s) of the material can then be expressed as the Curie-Weiss law:

$$\chi_s = \frac{C}{T - DC\gamma_m} = \frac{C}{T - T_C} \tag{2.3}$$

where T_C is the temperature at which the spontaneous magnetisation becomes zero. The magnetisation of the material can then be given by incorporating equation 2.1 into the normal Brillouin function:

$$\frac{M}{M_0} = B\left(J, \frac{\mu_B \gamma_m D M_s}{k_B T}\right) \tag{2.4}$$

where M_0 is the maximum magnetisation at 0 K, J is the total angular momentum and μ_B is the Bohr magneton. Figure 2.3 shows a plot of this function with Brillouin functions corresponding to $J = \frac{1}{2}$ and $J = \infty$. If $J = \frac{1}{2}$, the magnetic moment is due entirely to spin, therefore the fit to the experimental data in Figure 2.3(b) shows the ferromagnetism in nickel is due to the electron spin, with little or no contribution from the orbital motion of the electrons. This statement is also true of Fe and Co and explains why ferromagnetism is generally only observed in metals due to the availability of conduction electrons.

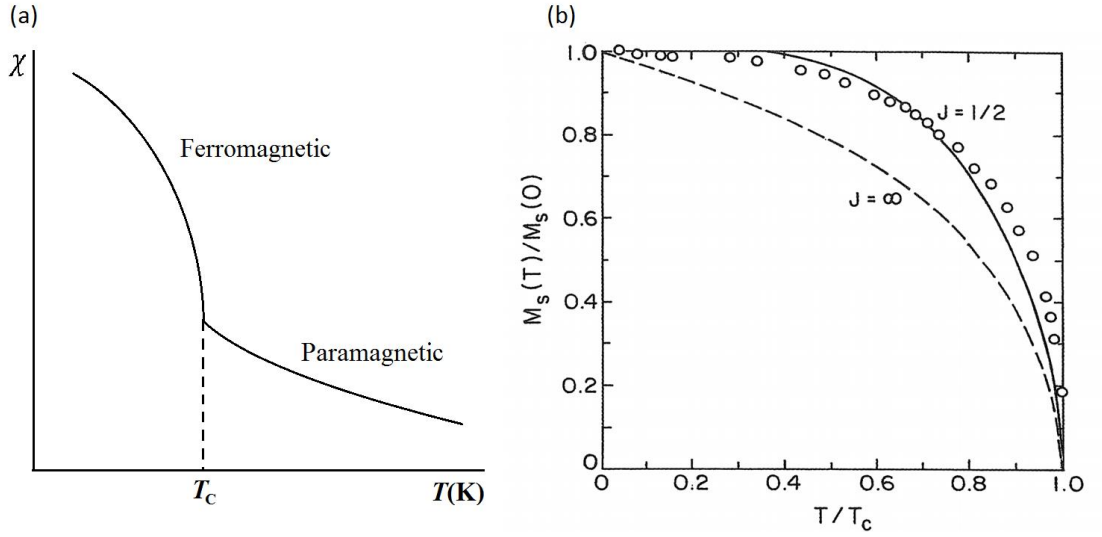

Figure 2.3 - (a) Variation of ferromagnetic susceptibility with temperature showing the transition point T_C [28] (b) Relative magnetisation of Ni as a function of relative temperature [29]. Solid line - Brillouin function where $J = \frac{1}{2}$, dashed line - classical solution where $J = \infty$. Open points represent experimental data from Weiss [19].

2.2 Antiferromagnetic Materials

Antiferromagnetic ordering occurs commonly in transition metal compounds as well as in certain metals, metal oxides and other compounds. It would be reasonable therefore to expect that all of the 3d transition metal elements that do not show ferromagnetic behaviour would show AF behaviour below their critical temperatures. However, only Mn and Cr have been shown to be antiferromagnetic. Due to the length-dependent nature of the exchange interaction, many alloys and compounds containing transition metal elements, which modify the spacing between the metal atoms can be antiferromagnetic. In this section, a number of these materials are discussed in more detail, in the context of their magnetic structure and their applicability to device applications.

As with ferromagnetic materials, the alignment of spins in an antiferromagnetic material is also lost after a critical temperature called the Néel temperature (T_N). Below this temperature, the magnetisation of each of the two sublattices in the AF material can be represented by the Brillouin function given in equation 2.4. Figure 2.4 shows a plot of the two opposing spontaneous sublattice magnetisations.

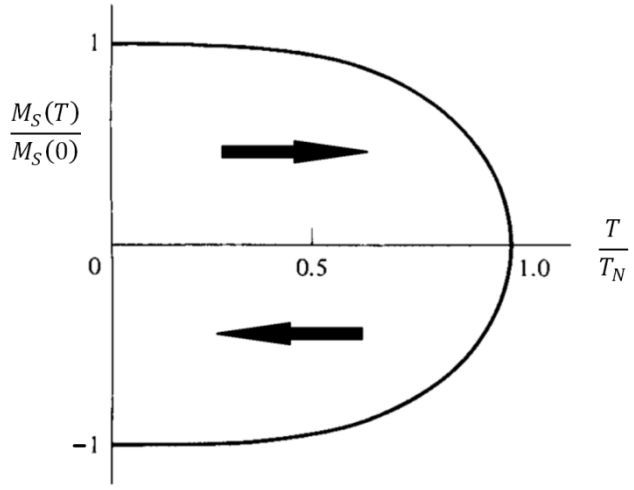

Figure 2.4 - Schematic diagram of the spontaneous opposing magnetisations of the two sublattices in an AF compound.

In polycrystalline materials, or when external fields are applied, torques exist on the moments leading to canting and therefore a non-zero susceptibility. This susceptibility will obey the Curie-Weiss law as given in Equation 2.3 but with a negative value of the ordering parameter (T_0) as shown schematically in Figure 2.5.

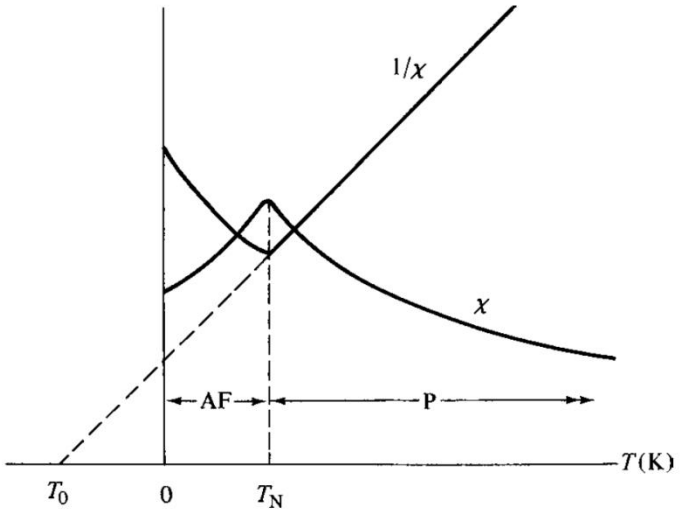

Figure 2.5 - Temperature dependence of susceptibility and inverse susceptibility for an antiferromagnetic material below and above the Néel temperature [4].

It follows from molecular field theory that T_0, the temperature at which the spontaneous magnetisation becomes zero, will also be the temperature at which the susceptibility of the material will become extremely high. Comparing Figure 2.5 to Figure 2.3(a), it is clear to see

that both ferromagnetic and antiferromagnetic materials behave identically above their ordering temperatures, as they are both in a paramagnetic state. However, the decrease in susceptibility below the critical temperature is unique to antiferromagnetic materials; meaning measurement of this relationship in bulk materials could be used as a method of identification of antiferromagnetic materials. Using sensitive equipment such as a vibrating sample magnetometer (VSM) or Faraday balance, it is possible to measure the susceptibility as a function of temperature and to observe the peak in the susceptibility at the Néel temperature.

The second widely-accepted technique for the determination of antiferromagnetic order is neutron diffraction. As the neutron only interacts weakly with matter and has a small magnetic moment of around 10^{-3} Bohr magnetons, its scattering will be dependent on both the positions of the nuclei and the magnetic moments of the atoms or ions in the material being probed. As neutrons are uncharged, they can penetrate into the bulk of the sample but this means that large amounts of sample are necessary. Unfortunately, even with modern equipment and averaging techniques, the sensitivity necessary to use these measurement techniques on thin film samples is not achievable or would result in counting times being unreasonable. As a result, a number of techniques are currently being developed for measurement of antiferromagnetic thin films, due to the increased interest in these materials in the field of spintronics. These techniques are discussed in Chapter 4.

2.2.1 Transition Metal Oxide Antiferromagnets

The transition metal monoxides were the first group of materials to be shown experimentally to be antiferromagnetic. Initially, this was done indirectly using susceptibility measurements and then later directly by neutron diffraction [30]. They all have a ‘rocksalt’ or face-centred cubic (FCC) type crystallographic structure and are quasi-ferromagnetically ordered within the (111) planes but antiferromagnetically coupled between the planes. This is possible since the relative orientation of the spins to each other is determined by the range of the exchange interaction. The main factor responsible for this type of ‘sheet’ arrangement is a type of indirect exchange interaction called superexchange. The two transition metal ions are separated by an oxygen ion as shown in Figure 2.6.

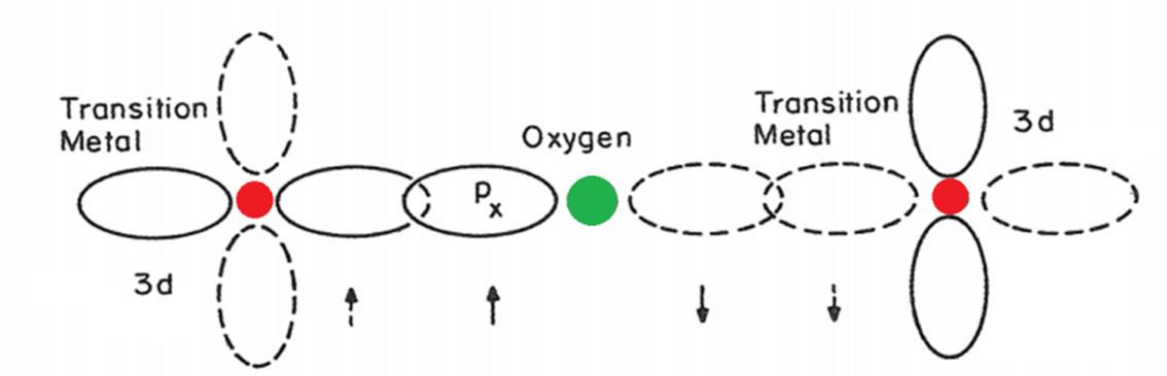

Figure 2.6 - Schematic diagram of d and p orbitals of the transition metal cations (red) and oxygen anion (green) responsible for the superexchange interaction [19]**.** The positive and negative parts of each orbital are represented by solid and dashed lines respectively.

At the separation illustrated in Figure 2.6, the two metal cations, which carry the magnetic moments, are too far apart ($R_a/R_{3d} \gtrsim 3$) for direct exchange forces to be of consequence. Instead, this interaction works indirectly by coupling the next nearest neighbour spins through the neighbouring oxygen anion. The strength of this bond is dependent on the angle between the two transition metal ions through the oxygen atom. The strength of the antiparallel coupling is generally greatest at 180˚. Superexchange applies to transition metal monoxides of the rocksalt structure, as shown in Figure 2.7, as well as many of the more complex spinel, garnet and perovskite oxides.

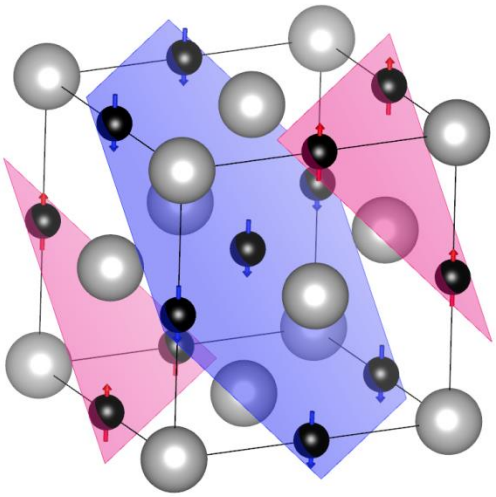

Figure 2.7 - Schematic diagram of the typical spin structure in the transition metal monoxides, oxygen atoms shown in grey, transition metal atoms in black.

In these more complex structures, the cancellation of the magnetic moments can be imperfect leading to materials with two opposing but unequal sublattices giving a measurable net moment. These materials are called ferrimagnets.

Whilst the basic spin structure is the same for MnO, NiO, FeO and CoO the orientation of the spins relative to the crystallographic axes varies [31]. In MnO and NiO the spins are oriented along the $(11\bar{2})$ direction [32, 33], in FeO in the (111) direction and in CoO slightly tilted away from the (100) direction [34] as shown in Figure 2.6. These data are summarised in Table 2.1.

Table 2.1 - Physical properties of the transition metal monoxides [31-35]:

Material	Structure	Spin ordering	Spin axis	Néel Temperature (K)	θ (K)
MnO	FCC	(111)	$(11\bar{2})$	122	610
FeO	FCC	(111)	(111)	198	570
CoO	FCC	(111)	(100)	293	280
NiO	FCC	(111)	$(11\bar{2})$	523	3000

The first of these oxides to be studied in detail was CoO. This was prompted by Co/CoO nanoparticles showing an exchange anisotropy effect, first observed by Mieklejohn & Bean in 1956 [23]. This effect is explored in much greater detail in chapter 3. NiO is of particular technological significance as it was the first AF used in a hard drive read head. It was chosen for this application due to the ~9.7% giant magnetoresistance (GMR) signal achievable at the time [36], its ease of production using sputtering techniques and moderate thermal stability. It has remained of interest, as its magnetic properties can be changed using control of the growth and particle size, or doping with other transition metals.

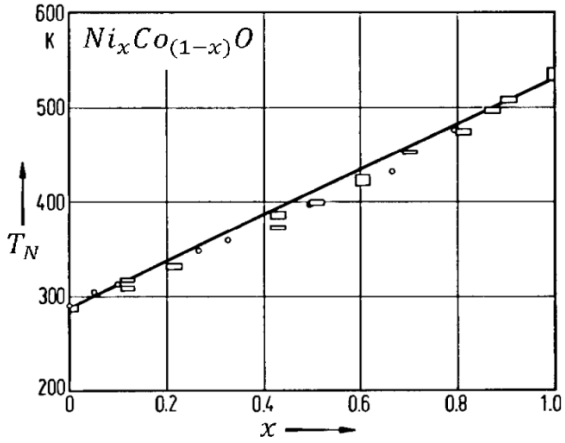

Figure 2.8 - Variation of T_N in $Ni_xCo_{(1-x)}O$ as a function of cobalt concentration [37].

Figure 2.8 shows a method of control of the Néel temperature through variation of the concentration of Nickel and Cobalt within the material, giving a linear relationship between the elemental concentrations and T_N. This relatively easy control of their magnetic properties has meant that the transition metal oxides have been used for many device applications ranging from electrochromic displays to chemical sensors [38, 39]. In the case of data storage, the complex behaviour of oxides is undesirable. Furthermore, when applied to spintronics the insulating / semiconducting electrical transport of oxides can lead to higher device resistances resulting in increased power consumption.

2.2.2 Elemental Antiferromagnets

As predicted by the Bethe-Slater curve in Figure 1.1 Manganese and Chromium are antiferromagnetic in their elemental form due to the negative value of the exchange integral caused by a lower interatomic distance than the other transition metal elements. Chromium has a body-centred cubic (BCC) arrangement with the corner atoms carrying spins orientated antiparallel to the body centre atoms along the (100) direction. This is shown below in Figure 2.9.

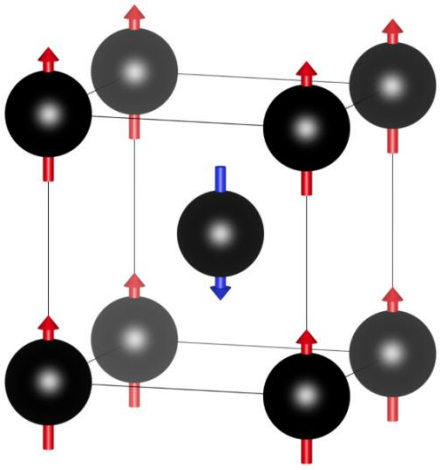

Figure 2.9 - Schematic diagram of Cr unit cell showing spin directions.

Interestingly, this ground state has an unusual structure which forms a spin density wave in which the local moment on each atom alternates direction and is sinusoidally-modulated in amplitude over around 20 BCC lattice constants [40]. The mechanism for this type of antiferromagnetism was explained in 1998 and exists to compensate for the internal strain energy present in the chromium lattice [41]. As a consequence, the antiferromagnetism in chromium is extremely sensitive to pressure. Chromium has seen no real world applications for its antiferromagnetic properties due to its low magnetocrystalline anisotropy. However, as

it has a well-defined Néel temperature, similar to that predicted for many novel antiferromagnetic compounds, ($T_N = 311$ K [42]), it is used in this work as a calibration material.

Manganese has a Néel temperature of 100 K [43] and has a complex unit cell with 29 atoms. Due to its low Néel temperature, it has seen no applications and is not relevant to this work.

2.2.3 Alloy Antiferromagnets

When antiferromagnetic materials were first applied to data storage as the 'pinning' layer in spin-valves (see Ch. 3.7) the only antiferromagnetic materials in use were the transition metal oxides and NiO was chosen. As technology improved, the low thermal stability of NiO due to its low anisotropy and small grain size became a problem meaning read heads in early hard drives needed to be re-set by passing a current through the head to generate a magnetic field and heat it during normal operation. This issue prompted research into a new group of antiferromagnetic materials. These new materials were alloys containing at least one transition metal element. Alloying with a second element allowed control of the spacing between the atoms carrying the magnetic moment and therefore the magnetic order. Through control of the stoichiometry and structure of magnetic alloy materials the type of coupling as well as anisotropy and thermal stability can be specified. For these reasons transition metal alloys have become the most diverse and widely-applicable group of antiferromagnetic materials currently in use.

FeMn was the first commercially-adopted alloy antiferromagnet. It has a FCC structure with a metastable antiferromagnetic phase with a Néel temperature between 390 to 520 K depending on composition [44]. Similar to many of the transition metal oxides, the Mn spins are quasi-ferromagnetically ordered within the (111) planes with each plane orientated antiparallel to its neighbours, resulting in a sheet antiferromagnet structure. Growth of this phase is achievable using a seed layer to induce (111) texture and using growth techniques such as sputtering or ion beam deposition, as these can yield higher adatom mobility during deposition, allowing access to the metastable antiferromagnetic phase. Typically, FeMn is grown on top of a permalloy magnetic layer as this serves as both the seed layer and pinned layer in a spin valve stack. Although widely adopted in magnetic data storage in the mid 1990's, after its initial discovery in 1966 [45], FeMn was not ideal since it had limited

anisotropy, due to its cubic structure and was also prone to corrosion when exposed to air [46].

Alloys such as PtMn and NiMn can have a greater crystalline anisotropy than FeMn. This is possible, using high temperature post growth annealing, since a fully-ordered $L1_0$ face centred tetragonal (FCT) phase can be formed from the FCC phase obtained during deposition [47]. For PtMn, an annealing temperature of 533 K for 8 hours is sufficient to crystallise the FCT phase [48]. Although the tetragonal distortion is subtle (<1% measured using XRD [48]) this increase in structural anisotropy greatly increases the thermal stability of the magnetic order. $Pt_{50}Mn_{50}$ has been shown to have a Néel temperature of 975 K [47]. Additionally, PtMn is antiferromagnetic over a wide composition range that allows control of the Néel temperature. For this reason, PtMn has been used in thermally-assisted magnetic random access memory (MRAM) [49] which uses current-induced heating to bring the temperature of the magnetic layers in an MRAM cell above their ordering temperatures, thus greatly reducing the necessary writing field.

Due to the demand for higher storage densities, many antiferromagnetic alloys were researched extensively during the 1980s and 1990s. The antiferromagnetic alloy IrMn stood out for its excellent magnetic properties, ease of growth, corrosion resistance and thermal stability. Additionally, compared to FeMn/NiFe bilayers, IrMn/CoFe bilayers have been shown to have excellent resistance to interdiffusion between layers. This meant GMR ratios over 5% and exchange bias are observable at temperatures over 500 K [50]. A comparison between the thermal stability of FeMn and IrMn spin valves is shown in Figure 2.10 (a).

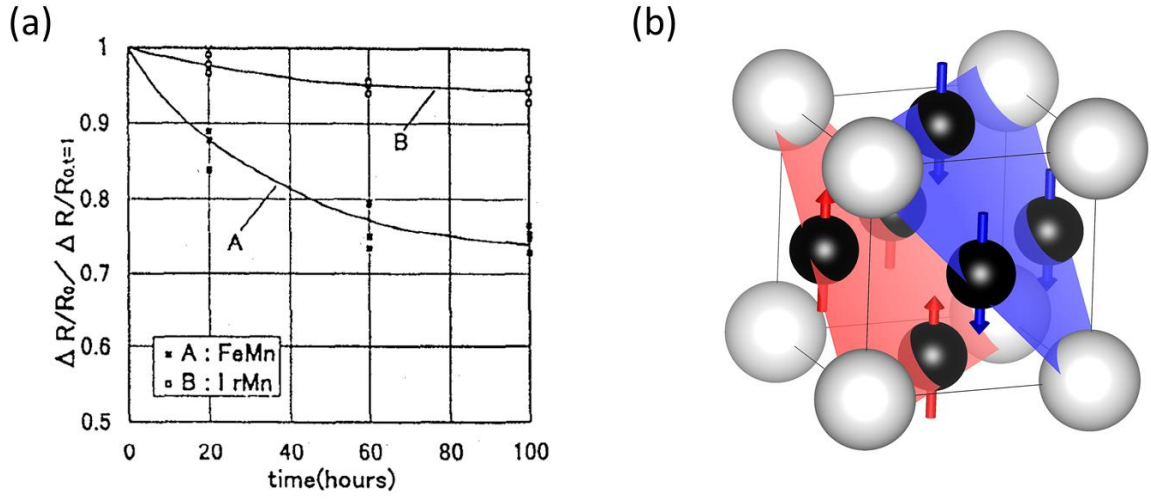

Figure 2.10 - (a) Exchange bias as a function of annealing time at 543 K for FeMn and IrMn bilayers [50] (b) FCC unit cell showing (111) sheet antiferromagnetic structure in IrMn.

Comparing the data for FeMn and IrMn shown in Figure 2.10(a), it is clear that the IrMn based spin valve has a far higher thermal stability and retains a ~20% higher magnetoresistance (MR) ratio after annealing for 100 hours. This improvement is due to the higher effective anisotropy in the IrMn than FeMn. The anisotropy is increased due to the relatively larger size of the Ir atoms as illustrated in Figure 2.10 (b) and the disorder in the structure of IrMn thin films when sputtered.

The $L1_2$ ordered $IrMn_3$ has been shown to exist in a triangular (T1) spin structure in bulk from both first principles [51] and using neutron diffraction [52]. The disordered phases, referred to as γ-Ir_xMn_{1-x}, have been predicted to have spin structures described as multiple-Q spin density waves [53]. Theoretically, it has been demonstrated that the 3Q spin structure can be stabilised in γ-Ir_xMn_{1-x} [54]. When considering polycrystalline sputtered films, it is important to recognise that there will be some compositional variation between grains meaning there is unlikely to be a single spin structure or mechanism responsible for the antiferromagnetic properties of the material.

In addition, it has been shown that sputtered IrMn films do not have the expected composition of the bulk $IrMn_3$, but instead have a disordered structure with a composition closer to $IrMn_4$. The maximum achievable exchange bias for these disordered structures has been demonstrated to be almost twice that achievable using $IrMn_3$ [55].

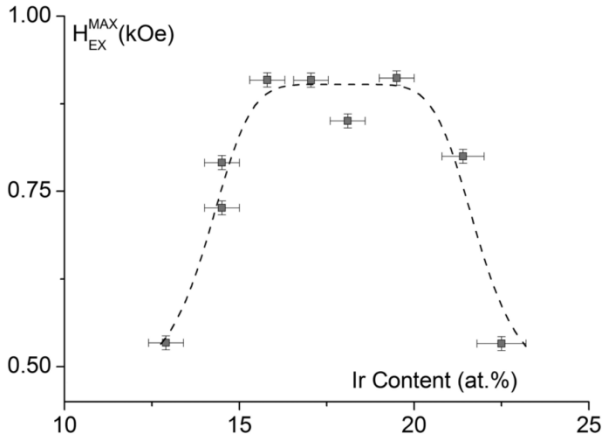

Figure 2.11 - Maximum exchange bias as a function of Ir content in $Ir_xMn_{(1-x)}/Co_{35}Fe_{65}$ bilayer samples [55].

As seen in Figure 2.11 the maximum achievable exchange bias occurs for IRMN alloys with Iridium contents between 16 and 20%, Aley et al. [55]. In a similar experiment using an ultra-

clean, ultra-high vacuum (UHV) sputtering system, Tsunoda et al. found the maximum achievable exchange bias for iridium concentrations between 22 and 32% [56]. It is likely that the difference observed in these two experiments is primarily explained by the error associated with measuring iridium content accurately. As iridium is the most corrosion resistant material known to date [57], chemical analysis cannot be used to determine the stoichiometry. Instead, less accurate techniques such as energy dispersive X-ray spectroscopy (EDX) were used to determine the composition.

Many theoretical models exist to predict the achievable exchange bias from exchange coupled ferromagnetic/antiferromagnetic systems. Of these models, the York model is the only model capable of fitting to the variation of the film thickness, lateral grain size and setting rate of the antiferromagnet at temperatures below T_N [58]. This model and the measurement protocols necessary to control the magnetic and thermal history of the sample, allowing reproducible measurements of exchange bias, are described in detail in chapter 3.

IrMn is now widely used in all commercial spin electronic devices including hard disk drives and next-generation magnetic memories. Although currently satisfying most technical demands, for the reasons outlined in section 1.4 there is interest in developing alternative antiferromagnetic materials that do not include critically scarce elements.

2.2.4 Synthetic Antiferromagnets

Synthetic antiferromagnets do not contain any antiferromagnetic materials, instead they contain two or more ferromagnetic layers separated by non-magnetic spacer layers. This type of thin film stack was researched extensively in the late 1980s [59-61]. The metallic spacer layers or tunnel barriers in these stacks are often over 1 nm thick meaning direct or superexchange mechanisms cannot be responsible for the magnetic order.

The longer range indirect coupling interaction responsible for this is known as the Ruderman–Kittel–Kasuya–Yosida (RKKY) interaction, named after the 4 authors who independently developed the model during the 1950s [62-64]. This theory is based on the coupling of atomic spins through conduction electrons, limited by the spin diffusion length of electrons in the material. The direction and magnitude of the RKKY interaction is oscillatory in nature as a function of separation.

As the spacing between the ferromagnetic layers increases, the sign of the exchange integral changes meaning the ferromagnetic layers switch between ferromagnetic and antiferromagnetic coupling as shown in Figure 2.12.

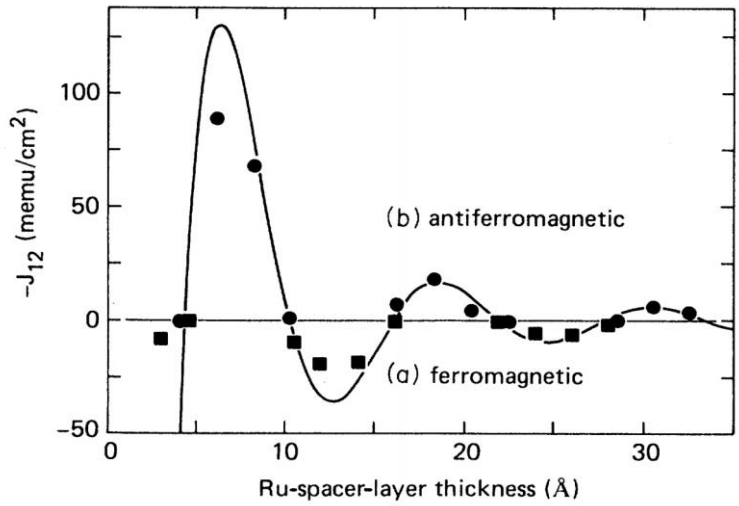

Figure 2.12 - The oscillatory nature of the RKKY exchange integral as a function of Ru spacer layer thickness between ferromagnetic $Ni_{80}Co_{20}$ layers [65].

This antiferromagnetic coupling was crucial for the discovery that the resistance of metallic multilayers was dependent upon the relative orientation of the magnetisation of neighbouring layers [66, 67]. This phenomenon is called giant magnetoresistance (GMR) when using a metallic spacer layer and tunnelling magnetoresistance (TMR) when using an electrically insulating tunnel barrier. This finding started the field of spin-polarised electronics or spintronics. These devices and their applications are discussed in detail in Chapter 3.

2.3 Imaging of Antiferromagnetic Structure and Domains

Imaging the structure of antiferromagnetic materials has remained a challenge since their initial discovery. Many of the techniques used to study ferromagnetic materials cannot be used, as they rely on measurement of the net moment generated by the material, whereas in antiferromagnetic materials this macroscopic magnetisation is compensated. As a result, the understanding of the underlying physics of antiferromagnets and exchange coupling remains unsatisfactory. It has been recognised that by imaging the antiferromagnetic spin structure a better understanding of antiferromagnetic exchange can be achieved.

Recently a number of techniques have been developed to do this. X-ray magnetic dichroism is a technique that uses the difference between two either linearly-polarised (XMLD) or circularly polarised (XMCD) X-ray absorption spectra to obtain information about the spin and orbital angular moments of the material. This is possible as the X-ray absorbance will be polarisation-dependent with respect to the spin and structure of the material. In the case of transition metals, the X-ray absorption spectra (XAS) are usually measured at the L-Edge, since at this excitation energy an electron will be promoted from the 2p to 3d band which is the electron energy level responsible for the origin of the magnetic properties of the element.

As XMLD does not require uncompensated spins, meaning it is applicable for the fully compensated antiferromagnetic layer. Used in combination with XMCD, these techniques can yield information on the coupling between antiferromagnetic and ferromagnetic layers.

Figure 2.13 shows XMCD images obtained for the ferromagnetic Co L_3 edge and antiferromagnetic Cr L_3 edge in Co/Cr_2O_3 films. Note that the XMCD signal generated from the antiferromagnetic Cr_2O_3 layer is due to uncompensated spins at the surface. To gain this spatial resolution the XMCD technique has been combined with photoemission electron microscopy (PEEM). Comparison of the images obtained for the ferromagnetic and antiferromagnetic layers show a clear indication of coupling between the layers, with a far sharper contrast in the antiferromagnetic domains achievable at 205 K below the Néel temperature of the Cr_2O_3 [68].

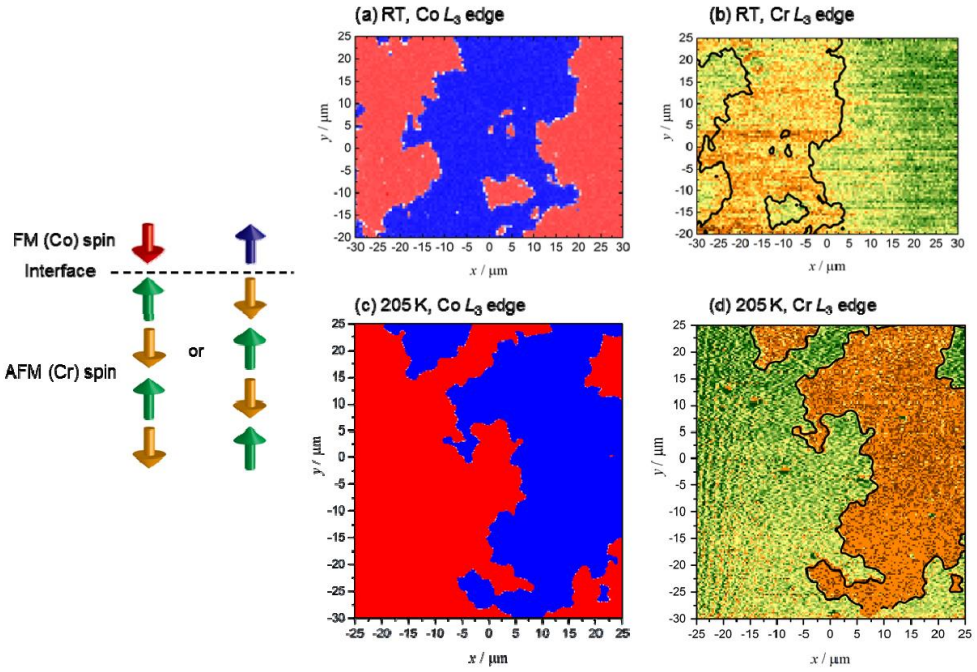

Figure 2.13 - XMCD/PEEM of Co/Cr_2O_3 Film at photon energy of 778 eV corresponding to the Co-L_3 edge and 576 eV corresponding to the Cr L_3 edge at room temperature and 205 K [68].

Similarly Arenholz et al. have demonstrated imaging of antiferromagnetic domains by combining XMLD and PEEM [69]. By imaging the same area using XMCD on the Co edge it was possible to demonstrate perpendicular coupling between the layers, this is shown below in Figure 2.14.

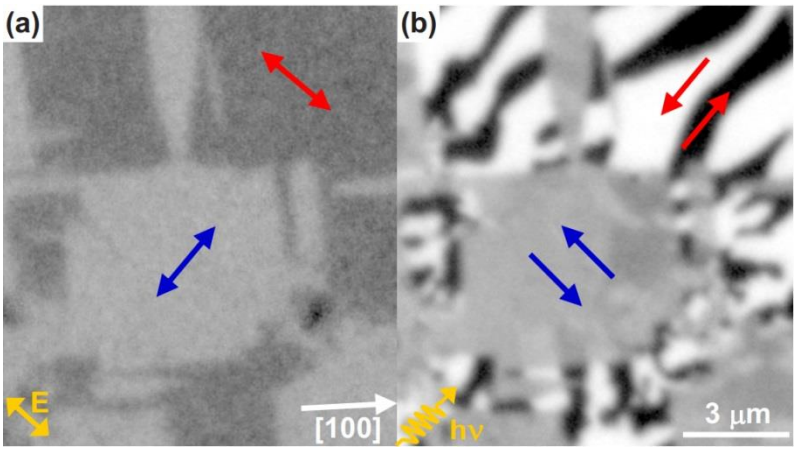

Figure 2.14 - PEEM images of 2.3nm Co film on a NiO (001) single crystal substrate (a) XMLD at the Ni L_2 edge. (b) XMCD at Co L_3 edge [69].

An alternative technique developed specifically for imaging antiferromagnetic domain structure uses a Magneto-Optical Indicator Film (MOIF). This technique requires a Bi-

substituted yttrium iron garnet (YIG) film placed directly above the sample. This enables the observation of stray magnetic fields at the sample surface through the magneto-optical double Faraday effect in the garnet film [70]. This image of the stray magnetic field is observed using polarised light in a modified optical microscope. By imaging using both polarisations of light and then quantitatively analysing the difference between the images it is possible to visualise the magnetisation dynamics of the antiferromagnetic domains in real time.

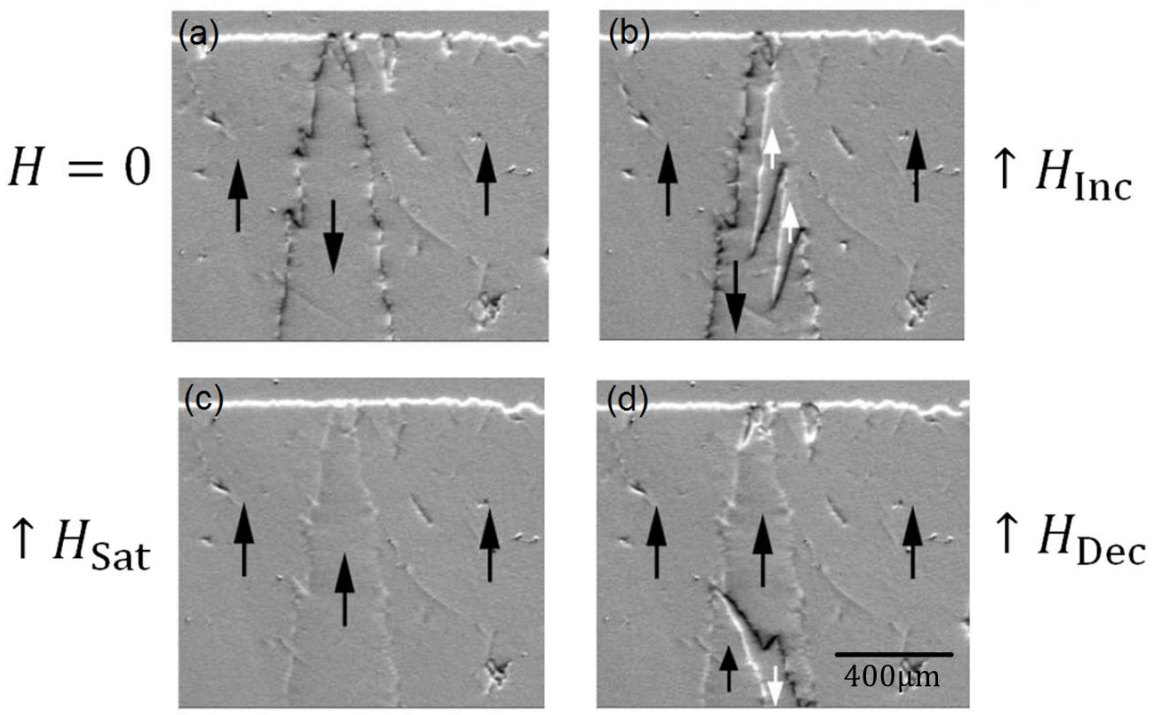

Figure 2.15 - MOIF images of domain patterns of a NiFe (16 nm) / FeMn (30 nm) bilayer film [70]. (a) At zero field (b) magnetising the film (c) at saturation (d) during reversal of the magnetisation of the film. Black arrows indicate the magnetisation direction of the ferromagnetic domains, white arrows indicate the direction of growing reversed domains.

Figure 2.15 shows an example of this type of measurement, (a) shows the sample after demagnetisation in an AC field at 400 K. (b) shows the invasion of 'up' domains into the central 'down' domain. (c) shows the sample at saturation in the 'up' direction. (d) shows the nucleation of reversal of the central domain back to the 'down' direction. This result is particularly interesting, as in an isolated ferromagnetic film, the domain patterns should be identical at symmetric points of the hysteresis loop. However, through comparison of Figures

2.15 (a) and (d) it is clear the reversal nucleates at different sites during magnetisation and demagnetisation of the sample; indicating that the underlying antiferromagnetic spin structure must not be static. Additionally, by comparing the slant of the growing domains during forward and backward reversal, it is clear that there is a chiral nature to the ferromagnetic reversal.

2.4 Exchange and Anisotropy

In antiferromagnetic materials, as there is no magnetic moment there is no shape anisotropy term and therefore the anisotropy is strictly magnetocrystalline in origin. Other effects such as strain will generally only give rise to a small change in the total anisotropy of the material.

In general, the common AFs such as transition metal oxides have a cubic structure and are therefore only weakly anisotropic. However, many of the commonly used AFs, whilst still cubic, have greater effective anisotropy since the atoms carrying the high magnetic moment lie on the body diagonal plane in the crystal. Within the plane, the spins are aligned parallel in a quasi-ferromagnetic order but the plane-to-plane orientation is anti-parallel giving rise to a relatively large anisotropy.

As mentioned previously, the measurement of the physical properties of antiferromagnetic materials including their magnetocrystalline and effective anisotropies is challenging. Techniques for the measurement of these properties are discussed in Chapters 3 and 6.

2.4.1 Magnetocrystalline Anisotropy

Due to the magnetocrystalline nature of the anisotropy in antiferromagnets, generally the anisotropy constant is single valued. However defects and inclusions in the crystal lattice can give rise to a narrow distribution of the anisotropy constants (K_{AF}). Because the anisotropy is magnetocrystalline in origin, it is temperature-dependent, generally varying in the form [71]:

$$K_{AF}(T) = K_{AF}(0)\left(1 - \frac{T}{T_N}\right)^n \tag{2.5}$$

The exponent n is taken to be 1 based on $K_{AF} \propto [m_{AF}(T)/m_{AF}(0)]^3$, and the approximation $m_{AF}(T) \propto (T - T_N)^{1/3}$ [72]. In conventional sheet antiferromagnets the anisotropy is generally uniaxial even though the crystal structure may be cubic. This arises because of the

orientation of the spins along a diagonal plane. Conveniently for polycrystalline films where each grain contains a single antiferromagnetic domain, this leads to a Stoner-Wohlfarth type reversal where the energy barrier to reversal (ΔE) is given by [73]:

$$\Delta E = K_{AF} V \left(1 - \frac{H^*}{H_K^*}\right)^2 \tag{2.6}$$

where V is the grain volume, H^* is the exchange field acting on the AF from the ferromagnetic (F) layer and H_K^* is a pseudo anisotropy field representing the resistance of the anisotropy of the AF to having its orientation reversed.

2.4.2 Anisotropy in Polycrystalline AF Films

Due to the distribution of grain volumes in polycrystalline films this gives rise to a distribution of energy barriers within the sample as a whole. By determining the distribution of blocking temperatures (T_B), the temperature at which an individual grain will reverse under the application of the exchange field and the grain size distribution within the sample, it is then possible to determine both the median value of the anisotropy constant and its distribution. This is achieved by progressively reversing the AF at incrementally higher temperatures until the loop shift is zero. At this temperature, the grain size currently being activated is that with the median volume, hence K_{AF} can be calculated [74]. This concept and measurement technique applies only to the case where the grains within a polycrystalline film contain a single AF domain. The exact size up to which a polycrystalline AF film will contain single domain AF grains is not known but it is assumed that all samples studied in this work will have grain volumes below this limit.

2.4.3 Domain Effects in Epitaxial AF Films

AF films that are grown epitaxially in the form of a single crystal or having large grains are known to have an AF domain structure [75]. This AF domain structure arises because of the domain structure in any adjacent ferromagnet that can be transferred into the AF via exchange coupling.

The nature of such an AF domain structure and its behaviour is generally not known and there exists a significant controversy as to the actual behaviour. However, work from our laboratory, some years ago, has shown that whatever the true nature of AF domains and their

behaviour, they can be well represented by a simple, strong domain wall pinning model [76]. In this model, AF domain walls become strongly pinned at defects or inclusions in the large grain or single crystal sample. For example, in the case of a large grain (>25 nm), the domain walls will become irreversibly pinned at grain boundaries because of the absence of intergranular coupling in a large grain AF system. However, relatively minor defects such as inclusions, even down to the atomic scale, will tend to pin domain walls because of the absence of magnetostatic energy in the AF layer itself.

It has been shown that introducing a relatively low level of Cu atom impurities into a conventional AF can more than double the resulting exchange bias due to the pinning of the domain walls. This is because where the pins are sufficiently strong, they effectively break up the magnetic domains in the large grains into smaller magnetic domains which, when sufficiently small, can become thermally unstable. Thus, at high levels of impurity doping, the exchange bias will fall [76]. Similar behaviour is observed when ion bombardment is used to induce defects into single crystal AF films [77]. Other reversal models can be found in [78]. The detailed measurement procedures used to obtain the values of K_{AF} and to determine the distribution of the domain wall pinning strengths are described in section 3.5.

2.5 Electrical Conduction in Antiferromagnets

The electrical transport properties of magnetic materials are governed by the valence electrons in the material. These electrons can become polarised by exchange with the electrons responsible for the magnetic order. This means that the electronic transport phenomena observed in magnetic materials can be useful as both probes into the magnetic properties of the material as well as for technological applications in the field of spintronics. Compared to the neutron techniques outlined in chapter 4, resistivity measurements can be conducted without the use of specialised research facilities. Primarily for this reason, a resistivity based measurement technique for antiferromagnetic materials has been adopted and developed in this work.

In rare earth elements and alloys the magnetic properties are associated with the 5*f* electron states. These states are capable of polarising the 5*d* and 6*s* states responsible for electronic conduction providing a spin and orbital angular momentum dependent conduction process. In transition metals, this process is simpler, as *d* states are shared between conduction electrons and those responsible for the magnetic properties.

The magnetic scattering of conduction electrons typically only provides a small contribution to the total resistivity. Thermal and grain boundary scattering along with scattering due to dislocations and impurities account for the majority of the total resistivity, especially in thin film polycrystalline materials. Matthiessen's rule states that if the origins of these scattering mechanisms are independent from each other, the resistivity of a material is the sum of the individual contributions [79]. Therefore the total resistivity (ρ) can be represented as:

$$\rho = \rho_0 + \rho_T + \rho_x + \rho_g + \rho_m \tag{2.7}$$

where ρ_0 is the intrinsic resistivity, ρ_T is the contribution due to thermal or electron-phonon scattering, ρ_x to impurities and dislocations, ρ_g to grain boundary scattering and ρ_m due to magnetic scattering. The intrinsic resistivity of metals can be represented by the free electron model. This model was first proposed by Drude in 1900 and assumes the transport of electric charge is by free electrons regarded as non-interacting point like objects [80]. This is analogous to the Boltzmann kinetic theory of gases, meaning the resistivity can be expressed as a function of the charge carrier density. This is shown in equation 2.8.

$$\rho_0 = \frac{m_e v_F}{N e^2 l} \tag{2.8}$$

Where m_e is the mass of an electron, v_F the Fermi velocity of the electrons, N the charge carrier density, e the electron charge and l the electron mean free path. Equation 2.8 predicts resistivity of simple metals very well, however in many other cases the model will not work, due to electrons being treated as classical particles. The Free Electron Model developed by Sommerfeld in 1927 [81], adds quantum mechanical Fermi-Dirac statistics to the Drude model. This was further improved by the Nearly Free Electron Model, which uses a similar quantum mechanical model of electrons but considers their interaction with the periodic crystal lattice in which they move. This model is therefore applicable to a much wider range of materials including semiconductors.

The second contribution to the total resistivity in equation 2.7 is the resistivity due to electron-phonon scattering. At most temperatures this contribution can simply be calculated by using the thermal coefficient of resistance (α_T), this is shown below in equation 2.9.

$$\rho_T = \alpha_T T \tag{2.9}$$

At low temperatures, this relationship does not hold and the thermal scattering process becomes more complex. This is explained by Bloch-Grunstein electron-phonon scattering, however this is not relevant to this work as at the measurement temperatures used electron-phonon scattering can be adequately described by equation 2.9.

Scattering due to impurities is usually proportional to the impurity concentration and can be represented as:

$$\rho_x = \frac{d\rho}{dx}x \tag{2.10}$$

where x is the impurity concentration. Similarly grain boundary scattering will vary as a function of the grain size, but will also be controlled by the film thickness, as scattering will also occur at the interfaces. It has been shown that when the film thickness becomes comparable to the electron mean free path within the material, it will exhibit a significant contribution to the total resistivity, due scattering at the interfaces. This contribution was described in detail by Mayadas and Shatzkes in 1970 [82].

The final term expressed in equation 2.7 is the contribution due to magnetic scattering. When considering this contribution in the case of antiferromagnets Mott's two current model can be adapted to represent the spin-up and spin-down channels. In the 1930s Mott recognised that electrical currents could be thought of as consisting of two separate currents of electrons each having up or down spin directions [83]. At temperatures below the Curie temperature or Néel temperature of a material, the spin direction of most conduction electrons is preserved in scattering events. Mott proposed a simple two-channel model that can be represented by the parallel circuit shown in Figure 2.16.

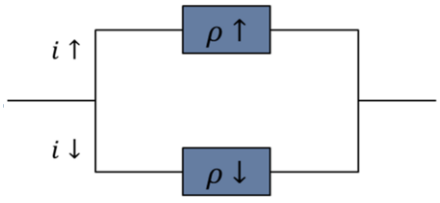

$$\rho_m = \frac{\rho\uparrow \,.\, \rho\downarrow}{\rho\uparrow + \rho\downarrow} \tag{2.11}$$

Figure 2.16 - Schematic representation of the Mott two-channel conduction model.

The resistivity of each channel is the total sum of all the scattering contributions described above. Although the electrical transport properties of antiferromagnets alone have not lead

to any technological applications, they provide a useful way to measure properties such as the Néel temperature, which is explored in detail in section 4.3. The most interesting phenomena concerning electrical transport in antiferromagnetic materials arise when an antiferromagnet is used to fix the orientation of a ferromagnetic layer in a thin film stack to produce a spin valve structure. By doing this giant magnetoresistance values can be generated. Spin valve structures and their applications are described in detail in section 3.7.

Chapter 3: Exchange Bias

Since its initial discovery in 1956 [23], the phenomenon of exchange bias has been a subject of considerable interest. However, exchange bias did not produce any technological applications until much later in 1986 [84], when it was applied to GMR devices to 'pin' the orientation of one of the ferromagnetic layers to a neighbouring antiferromagnetic layer. After its discovery, this pinning technique has now been incorporated into the design of hard drive read heads from 1998 onwards [85] and is also critical to the emerging field of spintronics.

After over 60 years of research there is still no complete theory that can accurately account for all observed effects of exchange bias in single crystal and granular systems. This chapter briefly summarises the strengths and weaknesses of the most significant models of exchange bias, and describes the York model of exchange bias for polycrystalline materials in detail.

3.1 Origin of Exchange Bias

In 1956 Meiklejohn & Bean [23] first observed that the magnetic hysteresis loops of small, partially oxidised cobalt particles could be shifted in the applied field axis by field cooling the sample prior to measurement. This effect was attributed to a thin layer of CoO on the surface of the particles. CoO is an antiferromagnet with a Néel temperature of 290 K [19] so when field cooled to below its Néel temperature in contact with a ferromagnetic layer, it will align its magnetisation axis to minimise the interaction energy across the interface as shown in Figure 3.1.

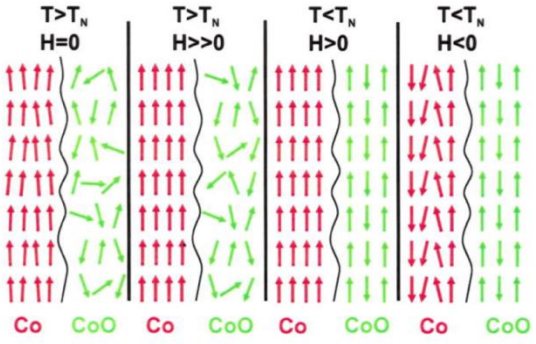

Figure 3.1 - Schematic diagram showing spin ordering across an exchange biased Co / CoO interface.

When the system is kept below the Néel temperature of the CoO, the magnetisation of the Co particles will now have a preferential, or 'biased' direction of magnetisation. This 'biasing' effect results in a shifting of the hysteresis loop in the applied field axis, shown schematically in Figure 3.2

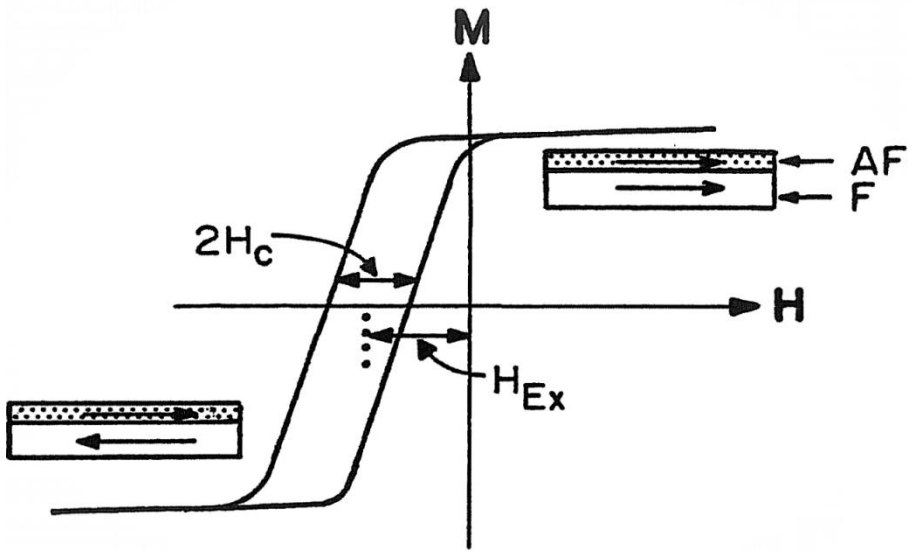

Figure 3.2 - Schematic diagram of an exchange biased hysteresis loop, showing the magnitude of the exchange bias (H_{EX}), coercivity (H_C) and the magnetisation orientations of the antiferromagnetic and ferromagnetic layers at saturation [19].

Apart from the shift in the hysteresis loop, it was observed that exchange biased systems displayed a unidirectional anisotropy and an additional enhancement to the coercivity which could not be explained using the existing Stoner–Wohlfarth rotational magnetisation model.

3.2 Theories and Models of Exchange Bias

A number of models have been developed to attempt to predict the variation of exchange bias (H_{EX}) and coercivity (H_C) in exchange coupled systems. This has proven challenging for a number of reasons. Primarily, many of the early data obtained were inconsistent due to the variation in the magnetic and thermal history of the sample prior to measurement. This is especially apparent for measurements taken at room temperature as thermal activation of the antiferromagnet can cause the sample to change over time [58]. Secondly, it is now recognised that there is not a single interaction mechanism responsible for exchange bias.

Instead, exchange bias can be considered as a combination of a number of mechanisms, including:

- Ferromagnet / antiferromagnet interface interaction, depending on the system there will be a varying degree of interface disorder leading to frustration at the interface.
- Self-interaction
- Cluster / Cluster interaction
- Dipole / Dipole interaction

Additionally there will be variation of the interface order during the reversal of the ferromagnetic layer. This level of complexity has meant that computational models have not been able to accurately predict exchange biased hysteresis loop parameters. Table 3.1 provides a brief summary of the some of the most significant models of exchange bias in order of publication date.

Table 3.1 - Summary of previous exchange bias models (all symbols are defined in the list of symbols):

Model	**Comments**
Meiklejohn & Bean (1956) [23]	$$H_{EX} = -\frac{J_{int}}{M_s . t_F}$$ – Directions of spins in AF & F are independent of distance to interface. – Uniaxial particles with a perfectly uncompensated AF spin structure at the interface. – All areas of the system behave identically. – Effect of applied field on AF is negligible compared to the exchange interaction with the F layer.
Néel (1967) [86]	– Spin structure of the AF at the interface subject to deformation and experiences irreversible changes during reversal of F layer. – H_{EX} and H_c will be affected by reversal of the system. – Roughness is considered leading to a partially compensated spin structure at the interface.
Fulcomer & Charap (1972) [87]	$$H_{EX} = \pm H_C - \left(\frac{N_{AF}}{M_S V_F}\right) \int_0^\infty \int_0^\infty m(t) \Delta e G(e_a, \Delta e) de_a d\Delta e$$

	– Thermal Fluctuation Aftereffect Model: – AF consists of small non-interacting particles coupled to an underlying F layer. – Numerical model based on a Stoner-Wohlfarth type reversal. – Large range of particle size and shape considered meaning large variations in anisotropy and coupling energy. – Each AF particle subject to thermal fluctuations in the orientation of its moment above its blocking temperature. – Uniaxial magnetocrystalline anisotropy was assumed for both the AF particles and underlying F layer. – First model to explain temperature and frequency dependence of H_{EX} and H_C.
Mauri (1987) [88]	$$H_{EX} = \frac{\sqrt[2]{A_{AF}K_{AF}}}{M_s t_F}$$ – Domain wall formation occurs parallel to the F / AF interface. – This domain wall lowers energy requirement of reversal by spreading the exchange energy over the domain wall width rather than a single atomic layer. – Relies on thick AF layers with perfectly flat interfaces.
Malozemoff (1987) [89]	$$H_{EX} = \frac{2z\sqrt{A_{AF}\ K_{AF}}}{\pi^2 M t_F}$$ – Assumes the F/AF interface is random on the atomic scale due to surface roughness and structural defects. – Results in the formation of AF domains with walls perpendicular to the interface, hence is only applicable in single crystals. – Interface is a mix of compensated and uncompensated areas, leading to prediction of H_{EX} two orders of magnitude lower than Meiklejohn & Bean.
Koon (1997) [90]	– Uses micromagnetic simulations to model exchange bias in an epitaxial single crystal system on a microscopic scale. – Predicts exchange bias for fully compensated and uncompensated interfaces. – H_{EX} arises in fully compensated system due to spin-flop coupling

	by AF spins canted away from the easy axis. – Model is flawed as predicts F magnetisation tended to orient perpendicular to the AF easy axis and that compensated / uncompensated interfaces lead to similar values of H_{EX}.
Stiles & McMichael (1999) [91]	– Model produced to describe polycrystalline exchange bias systems. – Assumes properties of the F layer are temperature independent, therefore only applicable when $T_C \gg T_N$. – AF grains have randomly oriented, non-uniform magnetisation coupled by direct and spin-flop coupling. – Coupling between F and AF is solely due to direct exchange. – AF grains must be large enough to sustain a partial domain wall formed during alignment of AF magnetisation. – Proposes two separate contributions to coercivity enhancement due to an inhomogeneous reversal and irreversible transitions.
Stamps (2000) [92]	Based on the existence of two different exchange bias mechanisms: Compensated interface: $$H_{EX} = \frac{\sigma}{2t_F M}\sqrt{1-\left(\frac{\sigma}{4J_2}\right)^2}$$ Uncompensated interface: $$H_{EX} = \frac{J_1}{Mt_f}\frac{cos\theta}{\sqrt{1+\frac{J_1}{2\sigma}\lvert sin\theta\rvert+\left(\frac{J_1}{2\sigma}\right)^2}}$$ – Predicts the existence of higher-order coupling terms when more than one AF sublattice is present at the interface – Magnetic and thermal stability of F & AF layers are crucial to the control of exchange bias.
Domain State Model (2001) [93]	– Proposes that a domain state forms in an AF layer diluted with non-magnetic impurities after field cooling in intimate contact with an F layer. – The imbalance of impurities in the AF layer will give a net magnetisation that couples to an applied magnetic field making the formation of this domain state energetically favourable.

	– Domain walls will preferentially pass through the sites of the non-magnetic dilutions. – K_{AF} is taken to be very large hence domain wall width can be assumed to be zero. – Original predictions made using Monte Carlo simulations were performed on an atomic monolayer of F material coupled to nine atomic layers of AF. – Predicted time and temperature dependencies as well as a strong dependence of H_{EX} on non-magnetic impurities and AF layer thickness.

Many of the models presented in Table 3.1 are able to predict qualitatively certain behaviours in either polycrystalline or single crystal materials, however none are able to provide quantitative agreement with a multiple sets of experimental data.

When considering polycrystalline materials, the thermal fluctuation aftereffect model of Fulcomer and Charap was the first to describe the temperature and frequency dependence of H_{EX} and H_C. Although it shows good agreement with experimental data for the exchange bias, the fit for the coercivity is poor. Fulcomer and Charap suggested this discrepancy could have occurred for a number of reasons. These include variation of shape and size distribution, variation of K_{AF} in small particles when compared to bulk and finally boundary effects dependent on the antiferromagnetic particle location on the underlying ferromagnetic film. Additionally, it is important to consider that although the model uses a distribution of particle volumes, it is stated that the shape of the distribution is irrelevant which has been shown to be untrue [58]. This model has formed a basis which has been used to further explain the temperature variation of exchange bias [94] and blocking temperature [95] in granular systems and forms the basis of the York Model.

3.3 The York Model of Exchange Bias

The work described in this thesis is interpreted using the York Model of Exchange Bias. This model is based on the interaction between sputtered polycrystalline ferromagnetic and antiferromagnetic thin films. The York model can be used to obtain the lateral grain size and

thickness dependence of H_{EX}, the value of the effective antiferromagnetic anisotropy and the contribution of interface effects. This is possible as the model was developed using data obtained using a set of measurement protocols which ensure that the magnetic and thermal history of the sample remain consistent between measurements and that measurements are only carried out at temperatures where no thermal activation occurs.

3.3.1 Energy Barrier and Reversal

The magnetic moment of a ferromagnetic single domain particle fluctuates around the equilibrium position [96]. The reversal of the moment is possible when the thermal energy ($k_B T$) exceeds the anisotropy energy barrier ($\Delta E = KV$). This reversal is described by the Néel-Arrhenius law which gives the relaxation time τ:

$$\tau^{-1} = f_0 \exp\left(-\frac{KV}{k_B T}\right) \tag{3.1}$$

where f_0 is the oscillation attempt frequency of the magnetic moment due to thermal fluctuations. This attempt frequency is often taken to be ~10^9 Hz which was calculated by Kneller as the gyromagnetic precession frequency in the anisotropy field [97]. Subsequently the attempt frequency has been measured in a fine particle system as 9.5×10^{11} Hz [98] and later as 2.1×10^{12} Hz in a CoFe/IrMn based exchange bias system in 2010 [99]. As the relaxation time is a function of the exponent of particle volume and temperature, it is strongly dependent on these parameters. Hence if a value of τ = 100s ($\ln(\tau f_0) > 25$) is chosen to define stable behaviour, as this is roughly the time needed to measure the remanence of a sample, the minimum energy barrier for superparamagnetic behaviour can be expressed as $\Delta E = 25 k_B T$ [100].

The energy barrier to reversal in antiferromagnets has previously been defined in chapter 2 in equation 2.6 and is reproduced below.

$$\Delta E = K_{AF} V \left(1 - \frac{H^*}{H_K^*}\right)^2 \tag{2.6}$$

The values of the exchange field (H^*) and the pseudo-anisotropy field (H_K^*) are not known however their ratio is assumed to be small. It is important to consider that in polycrystalline materials a distribution of the magnetocrystalline anisotropy and volume is expected, hence the energy barriers will also be distributed.

3.3.2 Time Dependence

When a ferromagnetic material is subjected to an external magnetic field, its magnetisation does not change instantaneously, instead it will change over a period of time due to its magnetic viscosity. This effect was first measured by Street and Woolley in 1949 [101, 102] who showed that in most materials the magnetisation had a logarithmic time dependence:

$$M(t) = S(H)\ln(t) + const. \tag{3.2}$$

where S is the magnetic viscosity coefficient. Street and Woolley suggested this coefficient should be proportional to absolute temperature. Later, Gaunt calculated the full dependence of the viscosity coefficient as [103]:

$$S(H) = \frac{dM}{dln(t)} = 2M_s k_B T f \Delta E_{(\Delta E_c)} \tag{3.3}$$

where M_s is the saturation magnetisation of the ferromagnet and $\Delta E_{(\Delta E_c)}$ is the critical energy activated at field H. This dependence will hold for antiferromagnetic materials though as they have no saturation magnetisation, it must instead be defined in terms of an antiferromagnetic order saturation value A_s:

$$S(H) = \frac{dM_{AF}}{dln(t)} = 2A_s k_B T f \Delta E_{(\Delta E_c)} \tag{3.4}$$

Often it is not possible to field cool antiferromagnetic materials from above their Néel temperature for measurements of exchange bias, as this would damage the sample structure. Instead, the antiferromagnet has to be 'set' at a lower temperature via a thermal activation process. This is achieved by heating up to an activation temperature under an applied field sufficient to saturate the neighbouring ferromagnetic layer. The antiferromagnet is then aligned by the exchange field from the ferromagnetic layer. The magnitude of the exchange bias observed after setting is both time and temperature dependent. When these dependencies are measured, the magnetic viscosity of the antiferromagnet can be calculated as a function of either parameter using equation 3.4.

The time dependence and magnetic viscosity of an IrMn(10nm) / CoFe(3nm) sample is shown in Figure 3.2 (a) and (b). In this experiment, the sample was initially set at a temperature of 498 K for 90 minutes in an external field of -1 kOe to ensure a known initial state of the antiferromagnet.

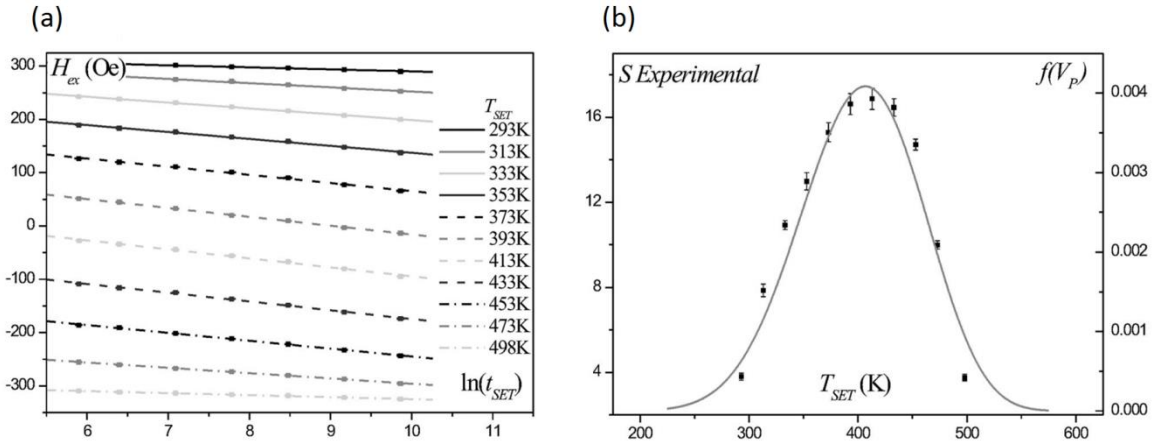

Figure 3.3 - (a) Setting time dependence of the of the exchange bias (b) Calculated magnetic viscosity as a function of setting temperature [104].

This linear behaviour of the $\ln(t)$ relationship shown in Figure 3.3 (a) is a special case. In 1985 Aharoni highlighted that the time dependence of magnetisation could not always be adequately described by linear $\ln(t)$ behaviour [105]. He suggested that by averaging over the actual distribution of energy barriers, rather than assuming the distribution remains constant, the variation of magnetisation could be calculated more accurately. Figure 3.4 shows the calculated time dependencies of the magnetisation by fixing the temperature and sweeping through the volume distribution by increasing the applied field. In this work El-Hilo et al. calculated similar data for different distribution widths and showed that non-linearity in $\ln(t)$ is greatest when the distribution of energy barriers is small.

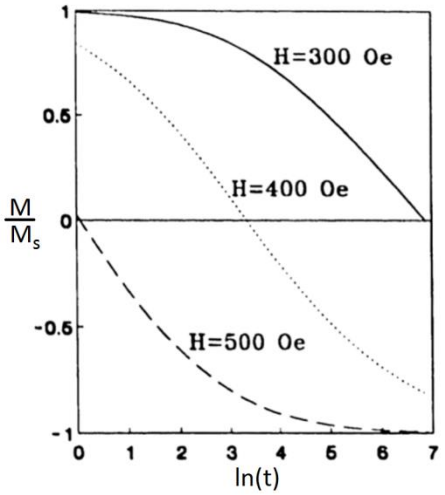

Figure 3.4 - Calculated variation of the reduced magnetisation with $\ln(\mathrm{t})$ for a narrow lognormal distribution of energy barriers over 1000s at $T = 20$ K for fields $H = 300$, 400 and 500 Oe [106].

This work shows that it is possible to infer information about the width of the energy barrier distribution from the magnitude of the non-linearity of the $\ln(t)$ data. For example the IrMn (10 nm) / CoFe (3 nm) films measured in Figure 3.3 must have a wide distribution of energy barriers, which will be caused by a large distribution of grain volumes.

3.3.3 Blocking Temperature

The blocking temperature (T_B) is defined as the temperature at which the exchange bias falls to zero. This temperature is conventionally found by measuring hysteresis loops at increasing temperatures until the exchange bias falls to zero. This measurement procedure results in the determination of the maximum blocking temperature, corresponding to the largest grains with the highest energy barrier [58]. A comparison between this conventional method and the York Protocol is shown below in Figure 3.5.

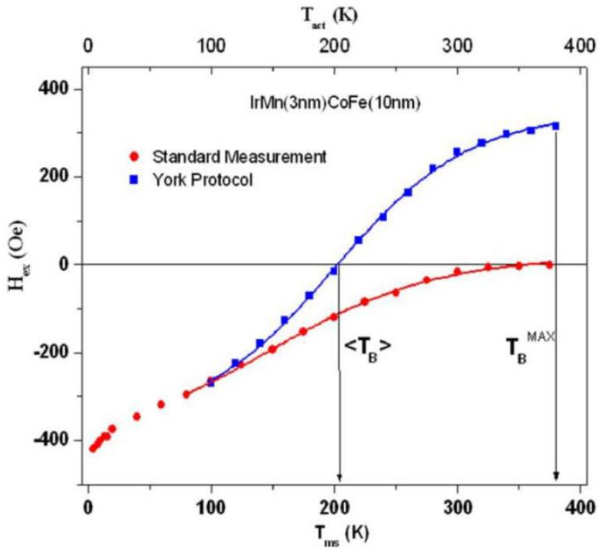

Figure 3.5 - Comparison of methods of measurement of the blocking temperature via standard thermal activation process and via the York Protocol [107].

From inspection of Figure 3.5 it is clear the York Protocol measurement gives a blocking temperature around 170 K lower than the conventional method. This occurs as when the conventional measurement procedure is used, the antiferromagnet is subject to thermal activation during the measurement time. By comparison, measurement via the York Protocols outlined in section 3.3.4, leads to the determination of the median blocking temperature which occurs at the point at where equal fractions of the energy barrier distribution are orientated in opposite directions. This method has been shown to be highly reproducible and not subject to thermal activation or measurement timescale effects.

3.3.4 Measurement Protocols

All measurements of exchange bias and blocking temperature in this work follow the York measurement protocols for exchange bias described by O'Grady et al. in 2010 [58]. The key requirements of these measurement protocols are to set the antiferromagnet in a reproducible manner and then to measure the sample at a temperature where no thermal activation occurs (T_{NA}). This is shown schematically in Figure 3.6.

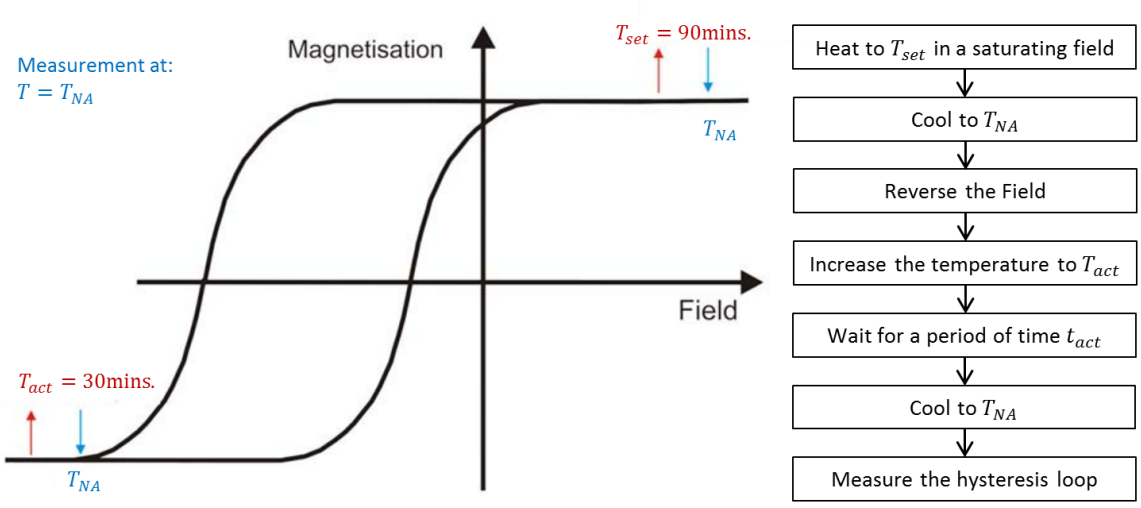

Figure 3.6 - Schematic diagram of the York protocol measurement procedure [58].

Before measurement of the blocking temperature as shown in Figure 3.5, a number of parameters must be determined. These include, the setting temperature (T_{set}), setting time (t_{set}) and temperature of no thermal activation (T_{NA}). These parameters have all been previously determined for IrMn / CoFe systems buy may differ for novel antiferromagnet systems. The activation time (t_{act}) is typically taken to be 30 minutes and the activation temperatures (T_{act}) will lie between T_{NA} and T_{set}.

T_{set} and t_{set}can be found experimentally by incrementally setting the antiferromagnet at increasing temperatures and times until the obtainable exchange bias reaches a saturation point. From these data it is possible to determine the time dependence as described in section 3.3.2.

T_{NA} can be found by incrementally measuring two hysteresis loops at decreasing temperatures until no change between the loops is observed after removal of any training effect.

3.3.5 Calculation of Magnetocrystalline Anisotropy

In polycrystalline magnetic materials, the energy barrier to reversal is proportional to the grain volume and anisotropy (Equation 3.5). As the York Protocol provides a measurement of the median blocking temperature, at which exactly half of the energy barrier distribution has been activated, through combination with an accurate measurement of the mean grain volume, it is possible to calculate the magnetocrystalline antiferromagnetic anisotropy constant:

$$K_{AF}(T_B) = \frac{\ln(t_{act} f_0) k_B T_B}{t_{AF} \pi (D_m/2)^2} \tag{3.5}$$

where t_{AF} is the thickness of the antiferromagnetic layer and D_m is the mean lateral grain size obtained from TEM analysis of more than 500 grains. Using this technique, the anisotropy of IrMn has been measured to be $(5.5 \pm 0.5) \times 10^6$ ergs/cm^3, significantly higher than measured by other techniques [58]. In subsequent work, the anisotropy of textured IrMn was measured to be $(2.0 \pm 0.5) \times 10^7$ ergs/cm^3 [108] demonstrating measurements of K_{AF} using this technique must be regarded as effective anisotropy values. It is important to note that the anisotropy is temperature dependent as it is magnetocrystalline in nature and will take the form:

$$K_{AF}(T) = K_{AF}(0)\left(1 - \frac{T}{T_N}\right) \tag{3.6}$$

3.3.6 Grain Size and Film Thickness Dependence

In polycrystalline antiferromagnetic materials the relationship between grain size and exchange bias does not follow any definitive trend, instead H_{EX} has been observed to both increase and decrease with grain size [109]. The York model proposes that this arises due to variation in the ratio of 'set' and 'unset' grains after the setting and field cooling process. A schematic frequency distribution showing the proportions of 'set' and 'unset' grains as a function of the grain volume is shown in Figure 3.7.

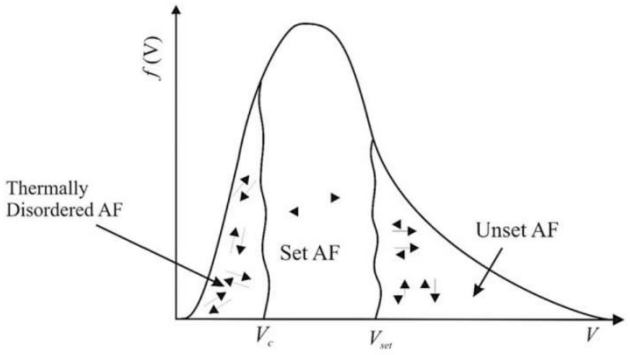

Figure 3.7 - Schematic diagram of the grain volume distribution in the antiferromagnetic layer after setting at temperature $\boldsymbol{T_{set} < T_N}$ [58].

The grain volume distribution shown in Figure 3.7 is split into three areas. The large grains with $V > V_{set}$ will not become thermally activated and therefore will not align with the ferromagnetic layer. Grains with size $V_c < V < V_{set}$ are set and responsible for exchange bias effects, finally small grains with $V < V_c$ are thermally unstable and disordered and will therefore not contribute to H_{EX}. These limits can be calculated using Equation 3.1 [110], the higher limit due to unset grains is given by:

$$V_{set}(T) = \frac{\ln(t_{set} f_0) k_B T_{set}}{K_{AF}(T_{set})} \tag{3.5}$$

where $K_{AF}(T_{set})$ is the value of the anisotropy at the setting temperature (T_{set}). Similarly the lower limit due to thermally active grains can be calculated using

$$V_c = \frac{\ln(t_{ms} f_0) k_B T}{K_{AF}(T_{ms})} \tag{3.7}$$

where $K_{AF}(t_{ms})$ is the value of the anisotropy at the measurement temperature T_{ms} and t_{ms} is the measurement time. These limits were calculated for an IrMn based system by Vallejo-Fernandez et al. in 2008; V_{set} = 757 nm^3 and V_c = 400 nm^3 [110]. In a 10 nm thick film these correspond to grain diameters of 9.8 and 4.9 nm respectively. As different fractions of the grain volume distribution fall between these limits the resulting exchange bias can both increase and decrease. This is shown in the 12nm thick IrMn sample shown in Figure 3.8(a).

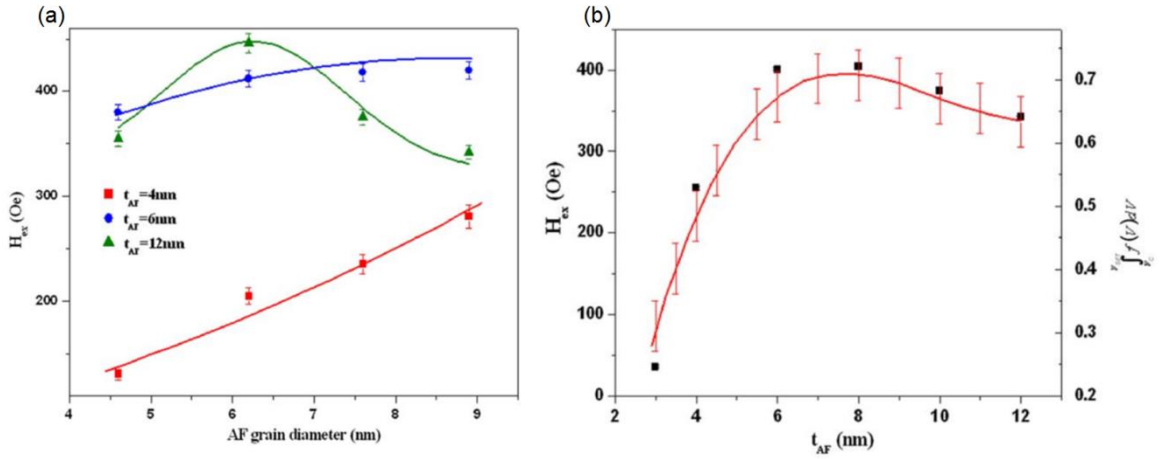

Figure 3.8 – Experimental data (points) and calculated fits (solid lines) for (a) Variation of $\boldsymbol{H_{EX}}$ with grain diameter for three samples with $\boldsymbol{t_{AF} = 4, 6, 12}$ nm. (b) Variation of $\boldsymbol{H_{EX}}$ with $\boldsymbol{t_{AF}}$ [110].

Figure 3.8 (a) and (b) differ mainly by the process by which the grain volume is varied. In (a) the grain volume is varied by lateral grain size, controlled by variation of the bias voltage in the HiTUS deposition system used. In (b) the grain volume is controlled by layer thickness alone.

This interpretation of the role of the antiferromagnetic grain volume in polycrystalline exchange bias systems is unique to the York model of exchange bias and has been shown to consistently fit experimental data.

3.4 Spintronics

Spintronics, a portmanteau of spin transport electronics, is the study of spin polarised electric currents. The origin of the field of spintronics can be traced back to initial experiments on magnetic tunnel junctions by Julliere in the 1970s [111]. However, spintronics began to play a significant role in the development of nanoscale devices after the discovery of GMR by Fert and Grünberg in 1988 [1, 2] for which they were awarded the Nobel Prize in 2007 [112].

Due to constant demand for higher data storage densities, the read heads in hard drives have needed to increase in sensitivity as well as decrease in size. After the introduction of GMR read heads in 1997, over 5 billion drives were produced [85], until the incorporation of TMR read heads into hard drives around 2005 [113]. In this section, a brief summary of the underlying theory and structure of GMR, TMR and future spintronic devices is presented.

3.4.1 GMR Devices

Magnetoresistance effects were first reported by Lord Kelvin in 1857 [114] when a relationship between the resistance and magnetisation of a conductor was observed. This anisotropic magnetoresistance (AMR) effect is due to electron spin-orbit coupling, which results in a difference of the scattering cross section, when the current is applied either parallel or perpendicular to the magnetisation.

Although the mechanisms responsible for AMR and GMR are different, they are both derived from the interaction of conduction electrons with the magnetic order of the material through which the current is being passed. GMR is based on spin-dependent scattering, first described by Mott in 1936 [83] who stated that the current flowing in a transition metal could be separated into two spin channels. A GMR device is purposely designed to exploit the spin-dependent scattering. It consists of two ferromagnetic layers separated by a conductive, non-magnetic spacer layer. This can be represented by a simple parallel resistor network as shown in Figure 3.9.

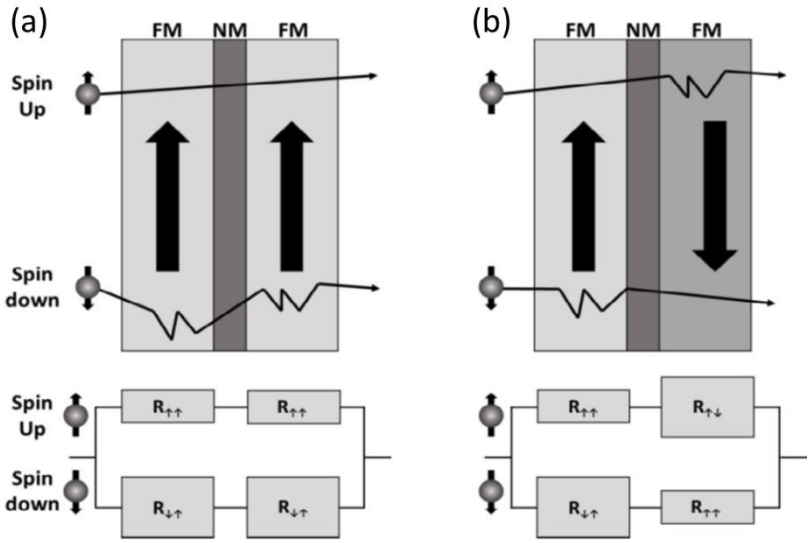

Figure 3.9 - Schematic representation of the GMR effect and spin dependent scattering using a resistor network model in (a) low resistance (parallel) state, (b) high resistance (antiparallel) state [85].

In Figure 3.9(a) spin up is the majority channel in both the ferromagnetic layers resulting in a low resistance device. Conversely, in Figure 3.9(b) the majority spin channels in the ferromagnetic layers are antiparallel resulting in both channels having higher resistance. The

structures shown in Figure 3.9 include the only layers necessary for the operation of a GMR device however the application of an external field is likely to rotate the magnetisation of both ferromagnetic layers. To solve this, researchers at IBM developed the spin-valve structure in the early 1990s [25, 115]. This structure uses an additional antiferromagnetic layer to 'pin' the orientation of the ferromagnetic (fixed) layer whilst allowing the rotation of the remaining (free) ferromagnetic layer. An example of a full spin valve assembly for a hard drive read head is shown in Figure 3.10.

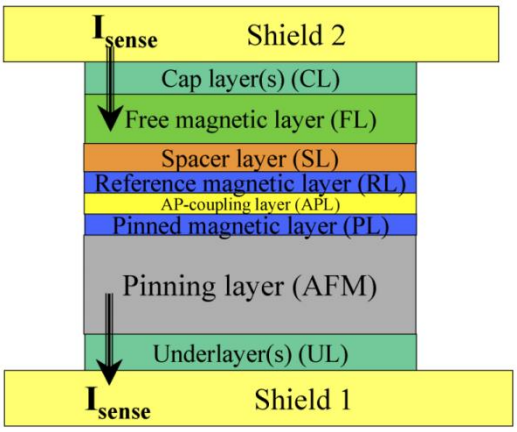

Figure 3.10 - Schematic diagram of the thin film multilayer stack used in a GMR read head sensor [7].

Typically in this structure the pinned and reference layers will be coupled antiferromagnetically while the free layer has an easy axis oriented perpendicular to these layers to produce a linear response of the sensor.

3.4.2 TMR Devices

Tunnelling magnetoresistance (TMR) devices are similar to GMR devices however the non-magnetic conductive spacer layer is replaced with a non-magnetic insulating oxide layer. This change in spacer layer necessitates a conduction process mediated by quantum tunnelling of electrons through the spacer layer. Compared to GMR devices this results in a much higher resistance area (RA) product which would result in higher power consumption, however as TMR devices are capable of displaying far higher magnetoresistance ratios they can be operated at much lower current densities. The flow of current across the spacer layer is dictated by the tunnelling potential between the layers as shown in Figure 3.11.

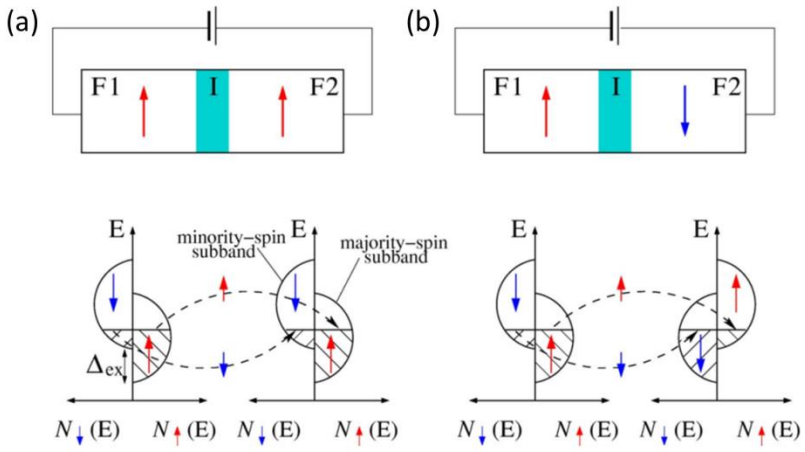

Figure 3.11 - Schematic diagram of a magnetic tunnel junction in (a) low and (b) high resistance states and the corresponding availability of empty states for spin tunnelling. F1 and F2 are the ferromagnetic layers and I is the non-magnetic insulating layer. Dashed lines depict spin-conserved tunnelling [116].

Figure 3.11 shows that the TMR conduction process is dependent upon the availability of states, when the magnetisations of the ferromagnetic layers are parallel there are a large number of majority conduction and valence states resulting in a high flow of electrons across the tunnel barrier. Whereas for the antiparallel arrangement there are fewer available states resulting in a higher device resistance [116].

This structure is commonly known as a magnetic tunnel junction (MTJ). Similar to the spin valve assembly previously described, an antiferromagnetic layer is used to pin the direction of one of the ferromagnetic layers. The availability of these states is described by the density of states (DOS) of the ferromagnetic layers.

By using *ab inito* electronic band structure calculations, it is possible to predict which materials will exhibit high spin polarisations. Combined with experimental work, this technique has led to magnetoresistance ratios in excess of 600% at room temperature and 1000% at low temperature in CoFeB / MgO / CoFeB MTJs [5].

3.4.3 MRAM

Considerable effort has been made by a number of companies to develop solid-state magnetic random access memory (MRAM). This type of memory would combine the non-volatility and radiation hardness of existing magnetic data storage with the access and write

speed of dynamic random access memory (DRAM). A simplified MRAM architecture is shown below in Figure 3.12.

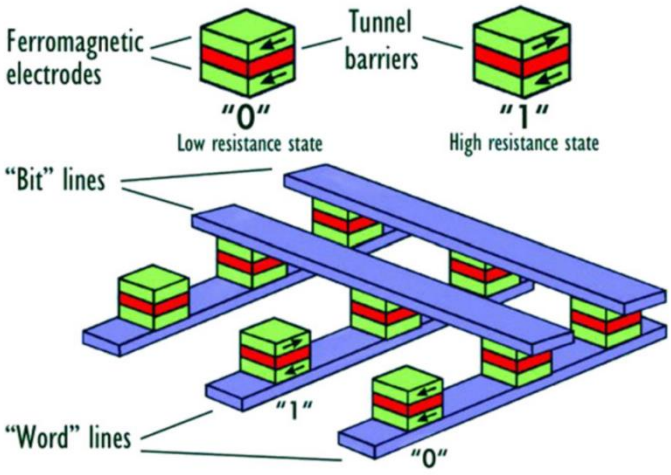

Figure 3.12 - Simplified schematic diagram of MRAM architecture [117].

In this architecture, a single MTJ is used as both the storage and read element. Early MRAM prototypes used magnetic field switching induced by a current passing through the word and bit lines, however this results in high power consumption and limits the density of the memory due to switching of neighbouring cells due to stray fields. The most extensively researched method to improve this involves the writing of data to an MRAM cell through the use of spin transfer torque (STT). This mechanism relies on the transfer of angular momentum from a spin-polarised current to the ferromagnetic free layer in order to reverse the magnetisation. In 2016 a functioning 4 Gbit STT-MRAM chip consisting of 8 x 512 Mbit banks was demonstrated by SK Hynix and Toshiba [118]. More recently, Deiny et al. have demonstrated a new nano-patterning technique which uses reactive ion etching to produce sub 30 nm undercut pillars onto which the MTJ devices can be deposited [119].

Chapter 4: Material Selection

In this chapter a number of materials with potential to replace IrMn in the field of spintronics are discussed. The criteria that these materials must meet are outlined in section 1.5. The majority of these materials are ternary alloys with the composition X_2YZ belonging to the Heusler alloy family. Work on these materials was conducted as part of the EU/JST HARFIR project in collaboration with other universities and research facilities listed in section 1.4. Additionally, the novel antiferromagnetic material MnN is described in detail along with recent results published by researchers at Bielefeld University.

To assess the applicability of these materials it is necessary to characterise their antiferromagnetic order and to measure the temperature at which magnetic phase changes occur. In bulk materials the conventional techniques used for these measurements are neutron diffraction and susceptibility measurements. However for reasons discussed later in this chapter, these techniques are not applicable to thin films. Additionally polarised neutron reflectometry (PNR) is described in detail.

4.1 Heusler Alloys

Heusler alloys are a family of ternary intermetallic compounds, first described by Friedrich Heusler in 1903 [120]. There are two main groups of ternary Heusler compounds classified according to their stoichiometry. They consist of three elements with the composition X_2YZ in the case of Full-Heusler alloys and XYZ in the case of Half-Heusler alloys, where elements X and Y are transition metals, and Z is a metalloid or non-metal [15]. In this work, only Full-Heusler structures are investigated. The first material investigated in this family was Cu_2MnAl, which was remarkable at the time of its discovery due to its ferromagnetic nature, despite none of its constituent elements being ferromagnetic [121]. Examples of the most common full Heusler alloy structures are shown in Figure 4.1.

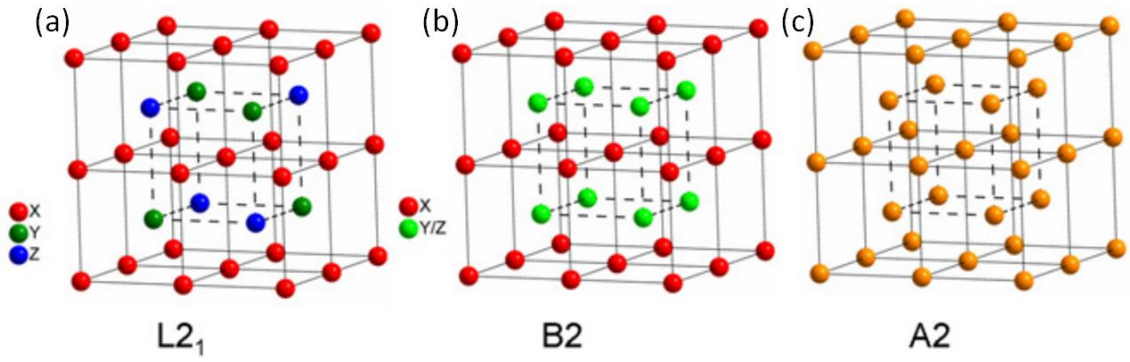

Figure 4.1 - Schematic diagrams of the unit cell of: (a) The fully-ordered *L*2_1 Heusler alloy structure. (b) The partially ordered *B*2 Heusler alloy structure. (c) The disordered *A*2 Heusler alloy structure [122].

This diverse group of materials has now grown to include an almost endless number of alloys with a huge variation in properties [123]. Alongside ferromagnetic alloys such as Cu_2MnAl, Heusler alloys have also been shown to demonstrate almost every type of magnetism. For example, Ni_2MnAl has been shown to be both ferro and antiferromagnetic in different phases [124], Co_2MnAl shows half-metallic ferromagnetism [125] and Mn_2VAl has been demonstrated to be ferrimagnetic [126]. Additionally, other properties such as superconductivity, shape memory effects, magneto-caloric behaviour and topological insulation have recently been shown to exist in Heusler alloys [127-130]. Due to this large variety of properties, Heusler alloys have attracted considerable interest. In the field of spintronics, Co-based ferromagnetic Heusler alloys have been studied extensively [131] due to their high spin polarisation resulting in extremely large TMR effects in devices of up to 1995% at 4.2K and 394% at room temperature being observed [132].

4.1.1 Magnetic Ordering and Properties

Heusler alloys consist of four interpenetrating FCC sublattices and have two magnetic sublattices. Full-Heusler alloys crystallise into a centre-symmetric cubic structure belonging to space group $Fm\bar{3}m$ [15]. As these materials consist of two magnetic sublattices they have been shown to exist with both parallel and antiparallel alignment of the spins in ferromagnetic, antiferromagnetic and ferrimagnetic structures. Since the magnetic ions occupy the NaCl type sublattice, their separation is large, hinting at a magnetic interaction based on a combination of direct and RKKY exchange coupling.

It is well known that the properties of Heusler alloys depend strongly on the degree of atomic order. Band structure calculations have shown that inducing small amounts of disorder within the distribution of atoms within the lattice sites causes distinct changes in their electronic structure [133, 134]. Figure 4.1 shows two levels of increasing disorder compared to the fully-ordered $L2_1$ state. The $B2$ structure is characterised by the mixing of the Y and Z atoms leading to a reduction in symmetry, space group $Pm\bar{3}m$. The $A2$ structure is a complete intermixing of the three elements resulting in a BCC unit cell with a structure belonging to space group $Im\bar{3}m$. It should be noted that the measurement of lattice site disorder is non-trivial. Conventional X-ray Diffraction is often not sufficient to characterise the degree of disorder, instead requiring further structural and electronic characterisation.

The properties of Heusler alloys can often be characterised more accurately by their valence electron count than they can by their constituent elements. Slater and Pauling discovered that the magnetic moment of the 3d transition metals and their alloys can be estimated on the basis of the average valence electron number per atom [135, 136]. This relationship holds for full-Heusler alloy structures as demonstrated in Figures 4.2 (a) and (b).

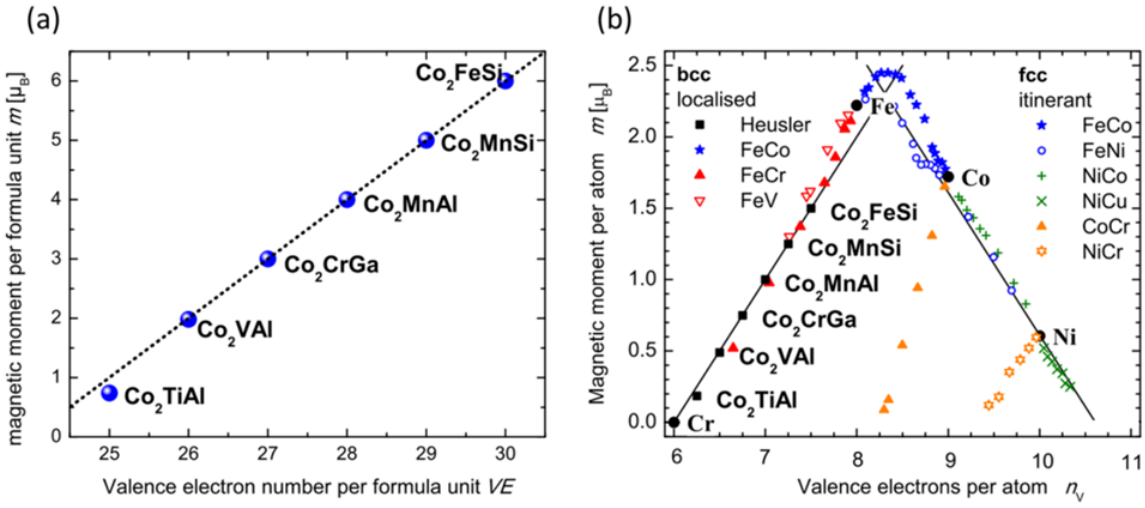

Figure 4.2 - (a) The magnetic moment per formula unit of Co-based Heusler alloys (b) The magnetic moment per atom of Co-based Heusler alloys and of the 3d transition metals and their alloys for comparison [15].

4.1.2 Screening for Antiferromagnetic Heusler Alloys

As an extension to the HARFIR project, researchers at the Bielefeld University conducted a theoretical screening process to attempt to identify potential antiferromagnetic Heusler alloys. The Automatic FLOW for materials discovery (AFLOW) library is a high throughput framework utilising the Vienna ab-initio simulation package (VASP) [137] and density functional theory (DFT) to calculate the ground-state properties of materials such as lattice parameters, formation energies and magnetic configurations [138] . This library was filtered using three simple criteria [139]:

1. Suitable elements – Elements not suitable for thin film deposition and processing are omitted.
2. Magnetism – At least one atom must have a non-zero magnetic moment.
3. Stability – The material must be stable against decomposition into other phases.

Calculations were then performed on compounds that met these criteria to determine the magnetic ground state and the Néel temperature. From over 80,000 full-Heusler alloys in the AFLOW library, 21 were found with an antiferromagnetic ground state and T_N > 290 K.

4.1.3 Antiferromagnetic Heusler Alloys

At the start of the HARFIR project a number of Heusler alloys were selected to allow experimental work to start immediately. These alloys were chosen based on a comprehensive review of literature. The materials, Fe_2VAl, Cr_2MnSb, Ni_2MnAl and Ru_2MnGe have all either been demonstrated or predicted to exist in at least one stable antiferromagnetic phase [124, 140-145]. Only Ni_2MnAl and Ru_2MnGe were selected for use in York, with other partners in the HARFIR project focussing on the remaining alloys.

Both Ni_2MnAl and Ru_2MnGe are manganese based Heusler alloys. Individual manganese atoms have a large magnetic moment of 5.92 μ_B [146] and contribute all of the magnetic moment in Ru_2MnGe and the majority in Ni_2MnAl.

Ni_2MnAl is interesting in that it has been predicted to exist in both ferromagnetic and antiferromagnetic states depending upon the order of the structure. In its $L2_1$ structure, Ni_2MnAl behaves ferromagnetically, however this phase is difficult to crystallise and requires hours of annealing at temperatures above 650 K [124]. The antiferromagnetic $B2$ phase is

more easily accessible and can be crystallised by annealing at temperatures below 500 K. In this phase, the Ni atoms form a cubic lattice while the Mn and Al atoms randomly occupy the other sites as shown in Figure 4.1 (b). The difference of magnetic ordering between these phases can be explained by considering the Mn-Mn nearest neighbour distance in each case. Using the experimental lattice constant of $a = 5.812$ Å determined by Acet et al. [124], the $L2_1$ structure has a Mn-Mn nearest neighbour distance of $a\sqrt{2}/2 = 4.110$ Å, whilst in the $B2$ structure, the closest spacing is $a/2 = 2.906$ Å. This change in coupling distance is significant enough to change the sign of the direct exchange integral, resulting in a switch to antiferromagnetic coupling between the Mn atoms. The predicted ground-state of this antiferromagnetic phase occurs with adjacent moments along the cube edges aligned parallel in one direction and antiparallel along the other. This is referred to as the AF3 state shown in Figure 4.3(c).

Ni_2MnAl has a theoretical Néel temperature of 313 K [141], the Néel temperature has been measured experimentally in a bulk single crystal and epitaxially grown single crystal thin film as 313 K and 300 K respectively [147, 148]. This Néel temperature means that although it can be set easily, it is unlikely to possess the thermal stability necessary for device applications. To rectify this, a number of techniques to increase the anisotropy such as doping and growth on seed layers were considered.

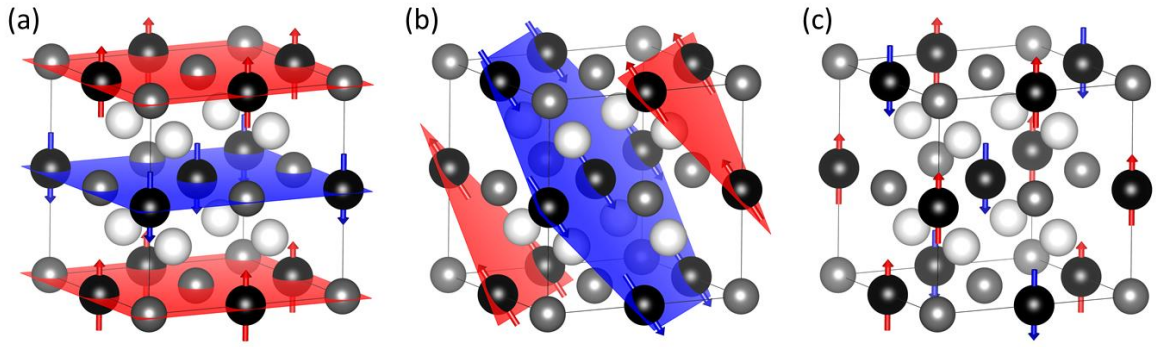

Figure 4.3 - Predicted antiferromagnetic spin structures for the magnetic ions in Heusler alloys, atoms: X_2 - white, Y-black, Z- grey (a) AF1 (100) Sheet antiferromagnetic structure (b) AF2 (111) Sheet antiferromagnetic structure (c) AF3 Alternating parallel / antiparallel spin arrangement [144].

Ru_2MnGe was the second of the prototype antiferromagnetic Heusler alloys investigated in this work. It has a bulk Néel temperature of 316 K [149] in its $L2_1$ ordered structure. The

calculation of ground-state energies for Ru_2MnGe have shown that the total energy is lowest in the AF2 state in a (111) sheet antiferromagnetic structure [144] with the Mn spins aligned in the (1-21) direction as shown in Figure 4.3(b). It has been demonstrated that when grown as a thin film subjected to compressive in-plane strain from a lattice matched substrate, a tetragonal distortion can be induced increasing the Néel temperature to 353 K [145]. It is expected that by controlling the growth and annealing conditions of these materials, it may be possible to optimise their antiferromagnetic properties.

4.2 Manganese Nitride

The manganese nitrides exist in a number of phases with a large variation in stoichiometry [150] ranging from 0 to 60% nitrogen [16], in paramagnetic ferromagnetic and antiferromagnetic states. The antiferromagnetic ordering in MnN was first investigated using neutron powder diffraction [17, 18]. Recently the equiatomic θ phase, θ-MnN has attracted more interest due to the volatility of the prices of iridium and the recent report of large exchange bias effects at room temperature in MnN/CoFe bilayer systems [151].

θ-MnN has a tetragonal structure shown in Figure 4.4 (b) with lattice constants of a = 4.256 Å, c = 4.189 Å at room temperature [152]. Although the structural anisotropy of MnN is small in bulk crystals (c/a =0.984), it may be possible to increase this ratio using growth techniques for thin film structures. The literature suggests that the θ-phase of MnN can be grown using reactive sputtering techniques at temperatures below 673 K with a nitrogen concentration over 40% [17, 153]. The phases of MnN as a function of growth temperature and nitrogen concentration are shown in the phase diagram in Figure 4.4 (a).

Neutron powder diffraction measurements have shown that the magnetic order is that of a sheet antiferromagnet with spins aligned along (100) planes. Interestingly, the collinear moment orientation has been shown to change as a function of temperature. At room temperature the moments are tilted at 23° to the c axis, as temperature increases to $T \cong T_N$ the moments align along the c axis [17].

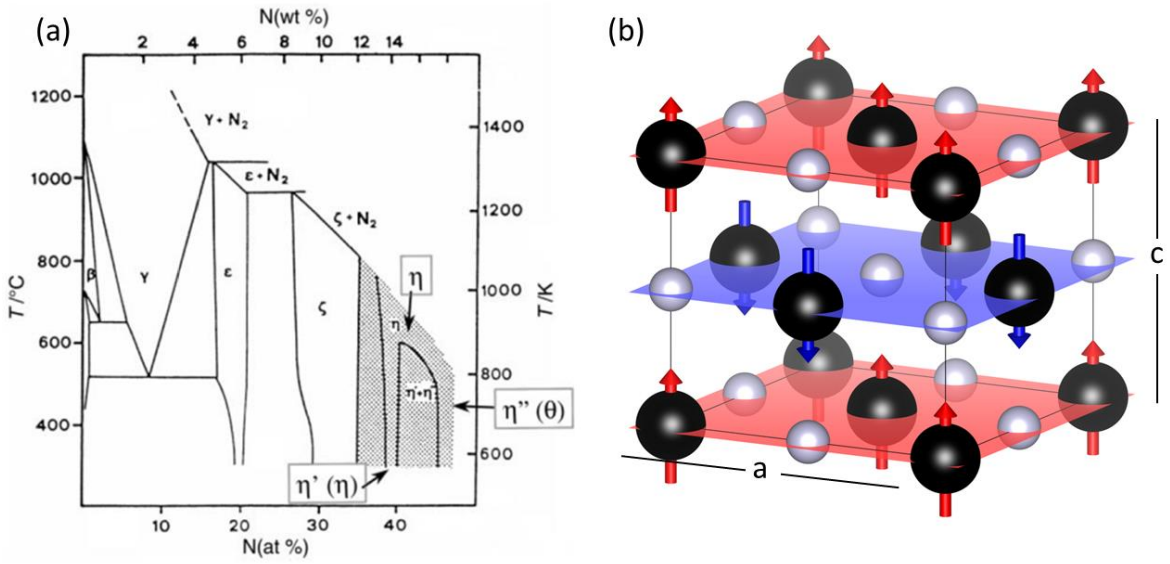

Figure 4.4 - (a) Phase diagram for the MnN system as suggested by literature. Phase of interest labelled η"(θ) [17]. (b) Tetragonal unit cell of θ-phase MnN, *a* = 4.256 Å, *c* = 4.189 Å [152], N atoms grey, Mn atoms black.

In 2015 researchers at Bielefeld University published a thorough report on the material θ-MnN demonstrating that it could in principle be integrated into GMR devices. In this report the exchange bias was explored as a function of film thickness and the crystallinity of the MnN layer. The crystallinity was controlled using a number of methods, both during growth and by post annealing. It was found that extremely large exchange bias fields up to 2.6 kOe [154] could be obtained at room temperature when using a 48nm antiferromagnetic layer and high temperature post growth annealing. Although this value of exchange bias obtained is remarkable, many industrial applications require much lower layer thicknesses typically below 10nm [155]. Previous work has shown that reducing the MnN layer thickness below 30 nm causes a sharp decrease in the obtainable exchange bias as shown in Figure 4.5 (a).

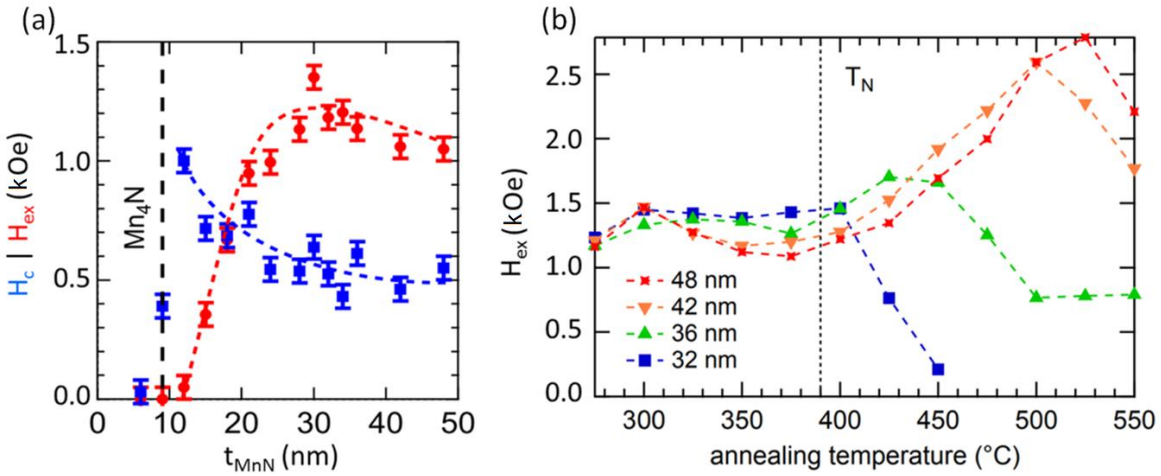

Figure 4.5 - (a) Coercivity (H_c) and exchange bias (H_{EX})as a function of MnN thickness (t_{MnN}) for a CoFe / MnN Bilayer system after annealing at 325°C for 15 minutes [151]. (b) Exchange bias as a function of post annealing temperature for CoFe / MnN Bilayers with MnN thicknesses above 32 nm [154].

The sharp decrease in the exchange bias shown in Figure 4.5(a) for MnN layers below 30 nm thickness is probably due to a number of factors. These include nitrogen desorption, microstrain, grain size and anisotropy. As the layer thickness is reduced, the grain size is also reduced. As the thermal stability of the antiferromagnet is a function of the grain volume this will lead to a large reduction in the observed exchange bias. Additionally, when annealing the films, nitrogen desorption into neighbouring layers will occur. In thinner films, sufficient nitrogen can diffuse out of the MnN layer to change the phase to Mn_4N as shown in Figure 4.5(a). Thicker films have sufficient nitrogen to resist desorption effects to higher temperatures. This is supported by the data shown in Figure 4.5(b) where the increased thickness of the MnN layer from 32 nm to 48 nm increases the critical annealing temperature above which the exchange bias decreases. From these data, it can be concluded that the exchange bias varies significantly as a function of the nitrogen content in the film. This variation is explained by the reduction of the lattice parameter as nitrogen content decreases, increasing the tetragonal distortion and therefore the magnetocrystalline anisotropy.

4.3 Characterisation of Antiferromagnetic Order

In this section, a number of techniques for the direct and indirect measurement of antiferromagnetic order are discussed. Due to its significance to this work, characterisation of antiferromagnetic order using electrical resistivity measurement has been omitted from this chapter. Instead, it is discussed from a theoretical perspective in Chapter 2 and from an experimental perspective in Chapter 5.

4.3.1 Susceptibility Measurement

Antiferromagnetic materials have a positive susceptibility at almost all temperatures. As a consequence, some antiferromagnetic materials were initially incorrectly classified as paramagnetic. Upon closer inspection, the variation of antiferromagnetic susceptibility with temperature is more complex than that of a paramagnetic material. As the temperature increases, at first the susceptibility increases until the Néel temperature is reached. At this point susceptibility reaches a maximum meaning any further increase in temperature causes a decrease in susceptibility. This peak in the susceptibility at the Néel temperature was one of the first experimental results pointing towards the existence of antiferromagnetic materials. The earliest example of this type measurement is shown below in Figure 4.6, and led to MnO being the first compound clearly recognised as being antiferromagnetic.

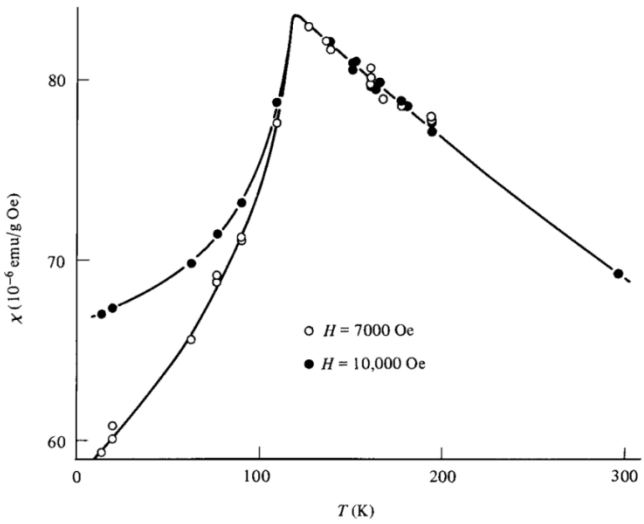

Figure 4.6 - The susceptibility of MnO powder as a function of temperature [156].

This technique for measuring the Néel temperature, although simple, relies on having a large mass of sample due to the low mass susceptibility of antiferromagnetic materials even when

using modern time averaged, lock-in amplifier based measurement techniques. This restriction makes this type of measurement unsuitable for samples with mass below 0.1 g when using equipment as described in chapter 6.3. For thin film samples however, the mass of the antiferromagnetic material sputtered onto a 5 mm substrate may be as little as 1 µg.

4.3.2 Neutron Diffraction

Although antiferromagnetic spin alignment can be inferred from susceptibility measurements, the first direct measurement of antiferromagnetic order was provided by neutron diffraction [22]. Neutrons, like all quantum particles, exhibit wave phenomena including diffraction. Crystal diffraction occurs when the wavelength of incoming radiation is comparable to the lattice spacing within the crystal. According to the de Broglie equation, the wavelength of a neutron is proportional to its momentum. By selecting neutrons emitted from a reactor by their speed, it is possible to create a neutron beam with wavelength near 1 Å. This beam will scatter according to Bragg's law and is described in detail in section 6.2.

Neutrons scatter predominantly from the nuclei of the atoms unlike electrons. This allows detection of diffraction peaks even at high angles, as the scattering intensity does not decrease as a function of the scattering angle, as it does for X-rays [157]. Additionally, neutrons carry a magnetic moment meaning they interact with the atomic spin of the incident material. This extra type of interaction means that neutron diffraction can be used to reveal further information about the magnetic structure of a material. An example of a neutron diffraction measurement on chromium is shown in Figure 4.7.

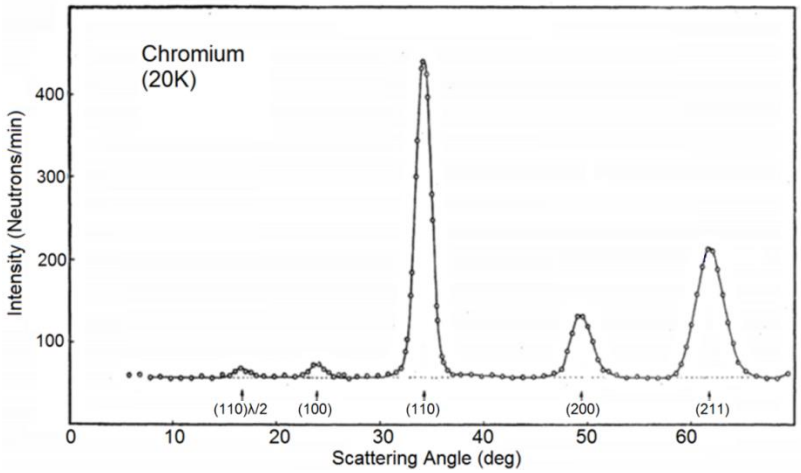

Figure 4.7 - Neutron diffraction spectrum for single crystal of chromium at T = 20 K [43].

To understand the significance of this spectrum, the nuclear and magnetic scattering must be considered separately. Chromium has a BCC unit cell so therefore it has a plane consisting of the body-centred atoms at the midpoint between (100) planes. First considering the nuclear scattering, the path difference for neutrons reflected from the atoms in this midplane compared to the (100) planes will be $\lambda/2$ meaning destructive interference will occur and no (100) diffraction peak will be observed in the spectrum. When considering the magnetic scattering this would also be true if these planes possess identical magnetic order, however if they are ordered antiparallel the scattering intensity will differ for each plane meaning complete cancellation will no longer occur and the (100) peak will be visible.

The presence of the (100) peak in Figure 4.7 can therefore be considered a direct observation of the antiferromagnetic order in chromium. The development of this technique in the 1950s earned Shull the Nobel prize for physics in 1994, shared with Brockhouse for the development of neutron spectroscopy [158]. Since its inception, neutron diffraction has become the preferred technique for characterisation of magnetic structure. Advances in detector sensitivity, source brightness and analysis techniques have reduced measurement times significantly and allowed spatial resolutions below 200 μm to be achieved [159]. Despite these advances, due to the high penetration depth of neutrons, neutron diffraction is not applicable for the analysis of magnetic thin films. Additionally, due to the requirement of a fission or spallation neutron source this technique can only be used at large research facilities.

4.3.3 Polarised Neutron Reflectometry

Polarised neutron reflectometry (PNR) was developed during the 1980s and allows depth-resolved analysis of magnetisation in magnetic films with thicknesses from 0.2 to 200 nm [160]. Although this technique shares some similarities with neutron diffraction, there are a number of key differences. Primarily, neutron diffraction makes the assumption that the magnetic moments of the incident neutron beam are randomly oriented. In PNR the polarisation of the incident neutron beam is controlled, meaning the intensity of the reflected beam can be measured allowing the determination of whether the spin state of the neutron was changed by reflection from the magnetic film or not. By measuring the intensity as a function of polarisation angle, it is possible to determine detailed vector information about the magnetisation direction in the film. Secondly, by using glancing angles of incidence and

meeting the criteria for specular reflection, depth resolution within the sample can be achieved.

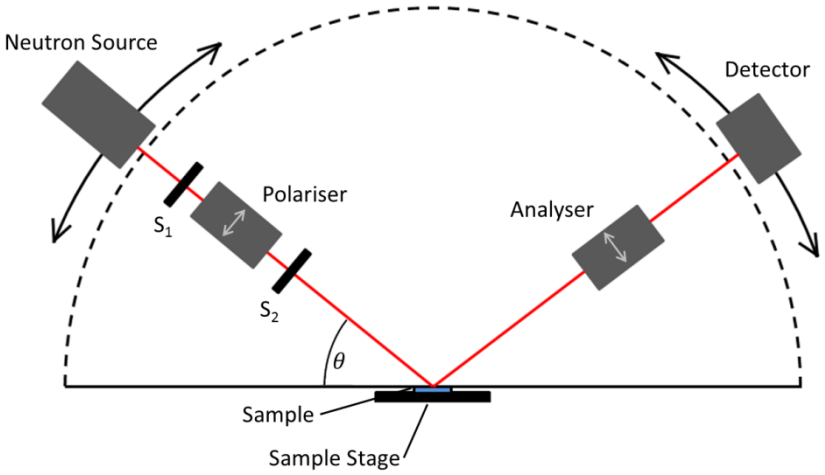

Figure 4.8 - Schematic diagram of the general components used in PNR apparatus.

Neutron reflectometers can operate in both fixed wavelength and broadband modes, depending on the source used. Figure 4.8 shows a general beamline arrangement for PNR apparatus. The two slits on the incident arm S_1 & S_2 define the incident beam width and collimation whilst incident beam and exit-beam polarisers control polarisation. The detectors used can either be position sensitive or actuated as shown above.

The data produced using this technique will be the total reflectivity of all layers of the sample, meaning the measured intensity will be a combination of multiple sets of interference fringes. Analysis of these data is non-trivial and must be done using comparison to modelled data. A similar technique is described in greater detail for XRR in section 6.2.2.

PNR has been used to observe a large number of phenomena in magnetic thin films. For example it has been used to monitor magnetisation reversal and domain formation in exchange bias systems [161-163], and to characterise magnetic phase transitions and antiferromagnetic coupling in the Heusler alloy Co_2MnGe [164, 165].

Chapter 5: Development of the Magnetoresistance Apparatus

The development of new antiferromagnetic materials for applications in devices requires the accurate characterisation of physical properties. In this chapter the experimental techniques developed for the measurement of electrical and thermal properties of thin film materials are described in detail. From the measurement of these properties it is possible to deduce further information, not available through conventional magnetic measurements, about the magnetic state of an antiferromagnetic material. Thus allowing continued improvement of the physical properties of thin film materials, leading towards device applications.

Magnetoresistance (MR) measurements work by measurement of the resistance in a temperature and field controlled environment. The overall accuracy of the measurement depends on many parameters. When determining the Néel temperature (T_N), temperature control and resistance measurements are critical. In this work, temperature was controlled through the use of closed-loop, proportional, integral, derivative (PID) control in an Oxford Instruments CF1200 cryostat. Resistance measurements were carried out using a 4 point Van der Pauw [166] geometry with a swept current controlled using a Keithley 2182a nanovolt-meter and 2635 source-meter. Measurement of T_N using magnetoresistance is possible due to the decrease in the resistivity caused by the transition from an antiferromagnetic to paramagnetic state, explained in detail in the previous chapter.

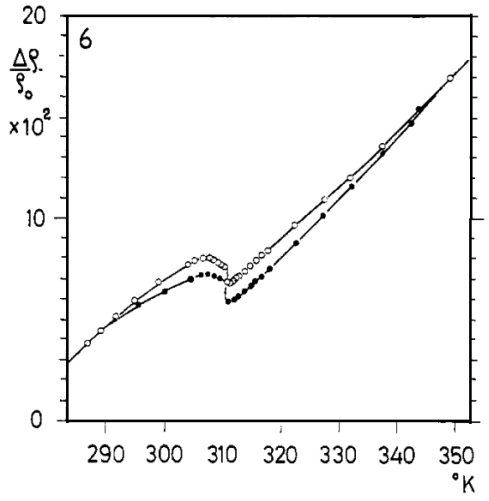

Figure 5.1 - Differential resistivity of single crystal Cr near the Néel Temperature [167].

Figure 5.1 shows an example of this type of measurement for a single crystal of Chromium measured over 17 days. This anomaly in the resistivity data is clearly visible at 311 K in both the increasing and decreasing temperature sweeps. It is possible to observe these anomalies independent of the direction of current flow during measurement as the current path within the material will be diffuse. The hysteretic behaviour in this transition was attributed to residual strain in the crystal.

5.1 Temperature Control

In this section, the method developed for temperature control accurate to < 0.5 K and stable to 0.1 K over the range 100 to 500 K is discussed. As the temperature range for many of the predicted Néel transitions in Heusler alloys is below room temperature, it was necessary to house the experiment in a cryostat. Additionally, to prevent oxidation of the sample, it was necessary to perform measurements in either a vacuum or an inert atmosphere.

5.1.1 Cryostat and Control Instruments

The experiment was housed in an Oxford Instruments CF1200 continuous flow, single stage, cryostat with a custom probe and heater allowing closed-loop feedback control from multiple temperature sensors. This is shown schematically in Figure 5.2.

Continuous flow cryostats are cooled by liquid cryogens pumped from a storage Dewar. As the cryogen (typically Nitrogen or Helium) is pumped into the cryostat, it is sprayed onto a hollow copper block with a thermal mass of ~30 J/K containing the sample space. This removes a large amount of thermal energy from the sample space in the cryostat, after which the cryogen vapours are pumped out through a return line. Temperature can be controlled by both the flow of the cryogen and a heater coil wound around the thermal mass surrounding the sample space.

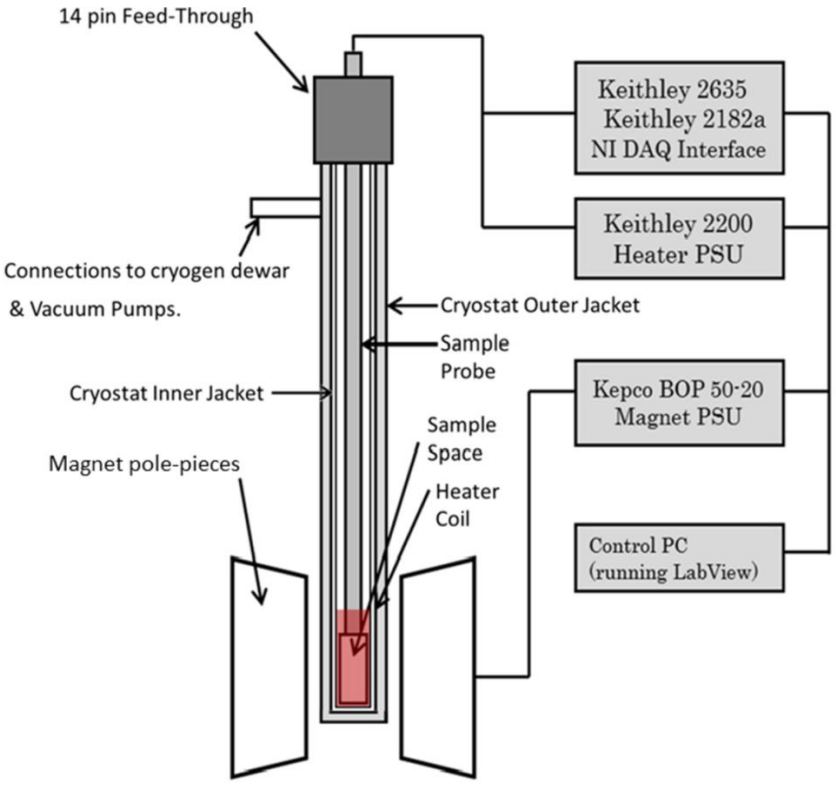

Figure 5.2 - Schematic diagram of the cryostat and control instruments.

The cryostat used in this work has been modified to allow separate pumping of both the sample space and inner/outer jackets. This allows the outer jacket to be pumped out to isolate the system from the environment. The cryogen can be managed in the inner jacket and the sample space can either be kept under vacuum or filled with an inert thermal exchange gas. Three pumps were used in conjunction with the system: a rotary roughing pump and turbo pump used for the outer jacket and sample giving a base pressure of $\sim 10^{-6}$ mbar and a diaphragm pump with a manual flow control valve, which was used to regulate the flow of the cryogen through the system.

There were a total of 14 electrical connections to the cryostat: 4 to the heater block (2 heater, 2 Platinum resistance thermometer (PRT)) and 10 to the sample probe (2 thermocouple, 8 electrical measurement). All connections were shielded.

The heater coil consists of $\sim$2 m of Ni-Cr heater wire wrapped counter-wound around the thermal mass surrounding the sample space. It was necessary to wind the coil in opposition so that when current flows, no net magnetic field was generated in the sample space. The coil has a total resistance of 50 Ω allowing almost the full power of the Keithley 2200 DC power supply to be utilised.

5.1.2 Feedback Control of Temperature

Temperature Sensor Selection

There are 3 common types of temperature sensor, mechanical, electrical and optical. Due to the small amount of space available in the cryostat, and ease of integration with computers, mechanical and optical sensors were not considered. This leaves electrical sensors, namely resistance temperature detectors (RTDs), thermocouples, and thermistors. Before construction of the MR apparatus, it was necessary to evaluate the specifications and performance of each sensor type in order to assess their applicability.

RTDs consist of a planar film or wire wrapped around a ceramic core where the resistance of the element has a linear response to temperature. Platinum is used to give the highest accuracy, although other metals such as nickel and copper can be used. The usable temperature range can be as large as 14 K to 1234 K [168]. At temperatures below 50 K the limiting factor is number of phonons present meaning the resistance is dominated by impurities and boundary scattering. At high temperatures the range is also limited, by increasing likelihood of contamination of the sensor element [169].

Thermocouples are bimetallic devices consisting of two conductors that produce a temperature-dependent voltage at their junction as a result of the thermoelectric effect. The properties of the thermocouple can be adapted by changing the two constituent metals. The most common thermocouple is chromel-alumel (type K) and has a sensitivity of 41 μV/K [170] in the range 90 K to 1500 K. Chromel-constantan (type E) thermocouples have a similar operating range and are commonly used in cryogenic applications due to their higher sensitivity of 68μV/K. Additionally, type E thermocouples are non-magnetic. The main limitation of thermocouples is their accuracy with system errors smaller than 1 K, often difficult to achieve over a ~300 K range.

Negative temperature coefficient (NTC) thermistors are again based on resistance, but use a semiconducting sensor element made of a sintered metal oxide. A NTC thermistor exhibits an inverse non-linear relationship between resistance and temperature, this can give high sensitivity but requires the calculation of the temperature using the temperature coefficient of resistance, or to maintain accuracy over a larger range, the use of the Steinhart-Hart equation [171]. Whilst the exponential nature of the resistance / temperature relationship

gives a higher precision than any other type of temperature sensor, it also means that at temperatures below 200 K, resistances become too large to measure accurately, making NTC thermistors unsuitable for cryogenic use.

There are two large copper thermal masses in the cryostat. One mass is for the heater / chiller block, and the other one is for the sample holder. A PRT was selected for the heater block as it could give the most accurate (<0.1 K error) temperature measurements over the desired temperature range. Due to space constraints and its completely non-magnetic nature, a type E thermocouple was used in the sample holder as shown in Figure 5.5. By incorporating two types of thermal sensor, both high accuracy and field invariance were possible. It was also notable that by having the sensors at two different locations, it was trivial to measure the system response time and latency when tuning the heater control algorithm as both sensors can be read simultaneously. Both temperature sensors were read using a National Instruments 6010 data acquisition (DAQ) interface.

Temperature Response Time

The design of the cryostat required a ~1 mm air gap between the heater/chiller block and the sample holder. When the inner jacket of the cryostat was pumped, this gap led to very low thermal transfer between the two thermal masses. As a result, the sample block takes over 20 minutes to respond to a temperature change of the heater/chiller block. Whilst this can lead to temperature stability better than 0.1 K, if the measurement is as a function of temperature, measurement times would be prohibitive.

To decrease the thermal response time of the sample block, it was decided to fill the inner chamber with an inert gas. Helium was chosen as it has a very high thermal conductivity due to its low molecular mass. This reduced the response time to less than 1 minute making tuning of the temperature control system easier and measurement times up to 25 times quicker.

LabView PID Control

PID control is a closed-loop feedback mechanism widely used in a large range of control systems. A PID control algorithm continuously calculates an error value $\epsilon(t)$, the difference between the set point and measured value. It then applies a correction to the control variable

$P(t)$ based on the sum of the three control terms. The addition of the three control terms is tuned using the proportional gain K_p. The overall control function can be expressed as: [172]

$$P(t) = K_p\left(\epsilon(t) + \frac{1}{T_i}\int_0^t e(t_i)dt_i + t_d\frac{de(t)}{dt}\right) \tag{5.1}$$

where t_i and t_d are the integral and derivative time constants. The proportional term produces an output proportional to the error signal. The integral term reduces steady-state errors and oscillations through low frequency compensation of the control variable by producing an output proportional to both the magnitude and duration of the error. Finally the derivative term monitors the rate of change of the error value to dampen any potential overshoot of the system when approaching the set point.

For optimal performance, the three values proportional (gain) and integral and derivative time constants must be tuned. However, as they are all mutually dependent and experience a degree of nonlinearity with temperature, this is a non-trivial problem. There are several methods for tuning a PID loop, with the more effective methods requiring the development of a process model to allow dynamic changes of the tuning parameters. The Ziegler-Nichols method was chosen as it is one of the most widely-used, straightforward methods since its inception in 1942 [173].

The Ziegler-Nichols method is a heuristic approach to PID tuning which works by inducing oscillations into the system by removing the integral and derivative terms. When only using proportional control, the proportional gain is increased to a value (K_u) where oscillations around the set point appear, at this point the time period (t_u) of the oscillations is measured. This value along with the value of K_u can be used to calculate loop parameters using the table below: [173]

Table 5.1 - Summary of optimum tuning parameters using Ziegler - Nichols method.

Ziegler – Nichols Method			
Control Type	K_p	t_i	t_d
Classic PID	$0.6K_u$	$t_u/2$	$t_u/8$
Some Overshoot	$0.33K_u$	$t_u/2$	$t_u/3$
No Overshoot	$0.2K_u$	$t_u/2$	$t_u/3$

By implementing the control and tuning algorithms in LabView it is possible to change the gain values depending on the temperature, allowing more accurate control over the full temperature range. The output to the heater coil was then supplied using a Keithley 2200 DC power supply.

Figure 5.3 shows an example of the control achievable using this technique. A temperature step of 2.5 K at 10 minute intervals between 225 K and 325 K was chosen. The temperature was measured using the thermocouple mounted in the sample space and shows that after a mild overshoot (~0.6 K) the temperature was within $\pm$ 0.1 K of the set point after 2.6 minutes until the next temperature step.

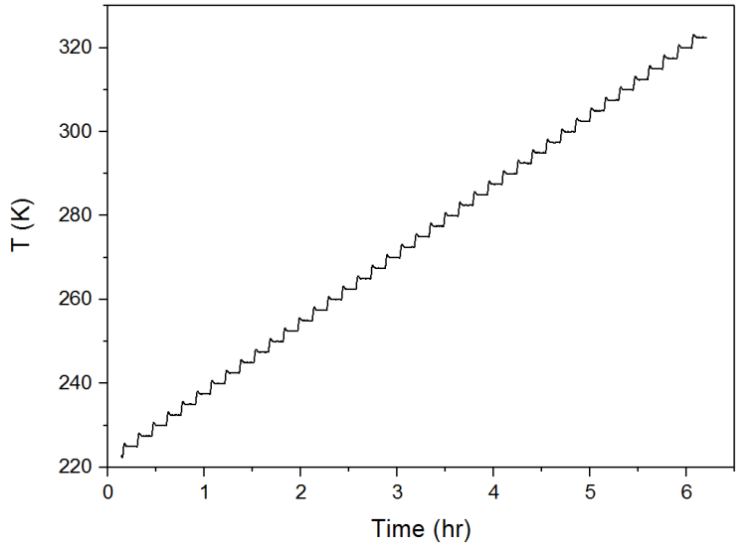

Figure 5.3 - Temperature as a function of time after optimisation of the tuning parameters for the PID system.

5.2 Magnetic Field Control

Although Néel temperature measurements do not require an external field, to improve the applicability of the MR apparatus to other measurements the equipment was mounted in a 5" Newport Instruments water-cooled electromagnet. A rack-mounted Kepco BOP50-20 bipolar 50 V, 20 A supply powers the magnet and can be either operated in an open loop current or voltage controlled, or closed loop feedback-controlled manner. The peak field obtainable using this power supply is 12 kOe with a resolution better than 1 Oe. Field is measured using a custom built Hall probe connected to the National Instruments DAQ

interface calibrated using a Lakeshore 425 Gaussmeter with a certified calibration traceable to the National Institute of Standards and Technology (NIST).

5.3 Electrical Measurement

The objective of the majority of the MR measurements in this work were to measure Néel temperatures of antiferromagnetic thin films. As shown in section 5.4.2 the change in resistance observed at the Néel transition due to the reordering of the spins from an AF to paramagnetic state is of the order 10^{-7} Ω. To resolve changes of this order it is necessary to employ a number of techniques to improve the precision of the apparatus. These methods are discussed in detail in this section.

5.3.1 Four Point and Van der Pauw Configurations

The four point probe technique, also known as Kelvin sensing, is a resistance measurement technique that uses separate pairs of current-carrying and voltage-sensing contacts. The separation of the source and sensing contact pairs eliminates the lead and contact resistances from the measurement. When measuring low resistances in thin films, this is essential, as lead and contact resistances can be up to 7 orders of magnitude larger than the film resistance.

The two current source connections generate a voltage drop across the impedance to be measured according to Ohm's law. This voltage drop is then measured using the two voltage-sensing connections. As almost no current flows through the sensing connections, the voltage drop is negligible. The applied current must be chosen to produce a large voltage drop so that it can be measured but must also be small enough not to produce localised heating effects in the sample over the timescale of the measurement. Figure 5.4(a) shows the measurement geometry used for a 4 point measurement, with the outer connections as the current source and inner connections as the voltage sensing connections. This method of measurement only yields a truly quantitative result when applied to a pseudo one-dimensional system, as it makes the assumption that all current flowing between the source contacts passes the sense contacts. If any alternative current path is available then this is not true.

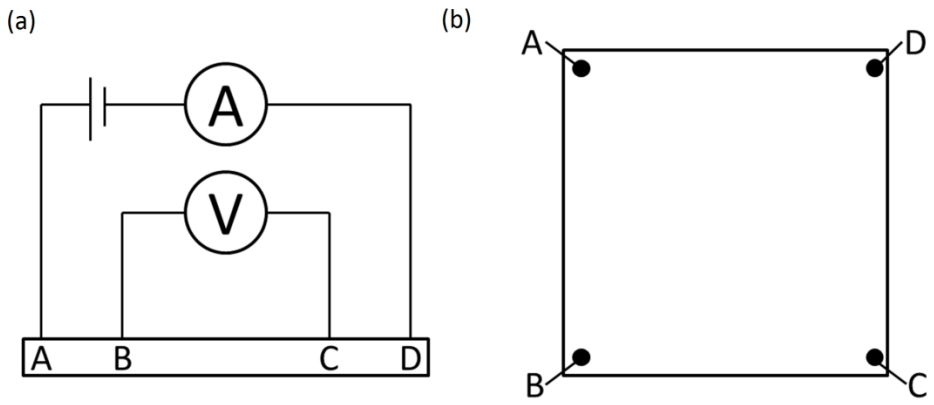

Figure 5.4 - (a) 4 point and (b) Van der Pauw measurement geometries.

Resistivity measurements by their nature are geometry dependent. Consequently, techniques have been developed to account for this. The Van der Pauw method of determining the resistivity in thin films is one of the most effective and widely-used techniques. In theory it can work for any sample shape [166, 174]. There are however preferred geometries used to reduce error [175] such as that shown in Figure 5.4(b) for a square geometry. In this case current is passed along one edge of the sample (A to D) and voltage drop measured along the opposite edge (B to C). Using these measurements in conjunction with an accurate measurement of the sample thickness, it is possible to obtain a value for the film resistivity. When the thicknesses or measured area are not exactly known it is possible to repeat the measurement passing the current between points A & B and measuring between points C & D. The two values obtained for the resistance (R_{BC} and R_{CD}) can then be used to calculate the sheet resistance R_s using: [176]

$$exp\left(\frac{-\pi R_{BC}}{R_s}\right) + exp\left(\frac{-\pi R_{CD}}{R_s}\right) = 1 \tag{5.2}$$

Equation 5.2 requires a numerical solution, though this is trivial to complete in a number of software packages. A VBA (Visual Basic for Applications) script was written allowing for solutions of R_S to be calculated for full data sets automatically in Excel. Once solved the sheet resistance, with units Ω/square, allowed direct comparison between samples of different sizes as it is independent of the sample dimensions.

5.3.2 Probe Head Design

There are two commonly used methods for making electrical contact to thin films: the use of spring contact probes or by wire bonding. Due to the high throughput of samples required as part of the HARFIR project and the excellent repeatability achievable, spring contact probes were chosen. To allow for either linear 4 point or Van der Pauw measurements to be conducted using the same probe, a total of 8 spring contact probes were used. The arrangement of these probes is shown in Figure 5.5.

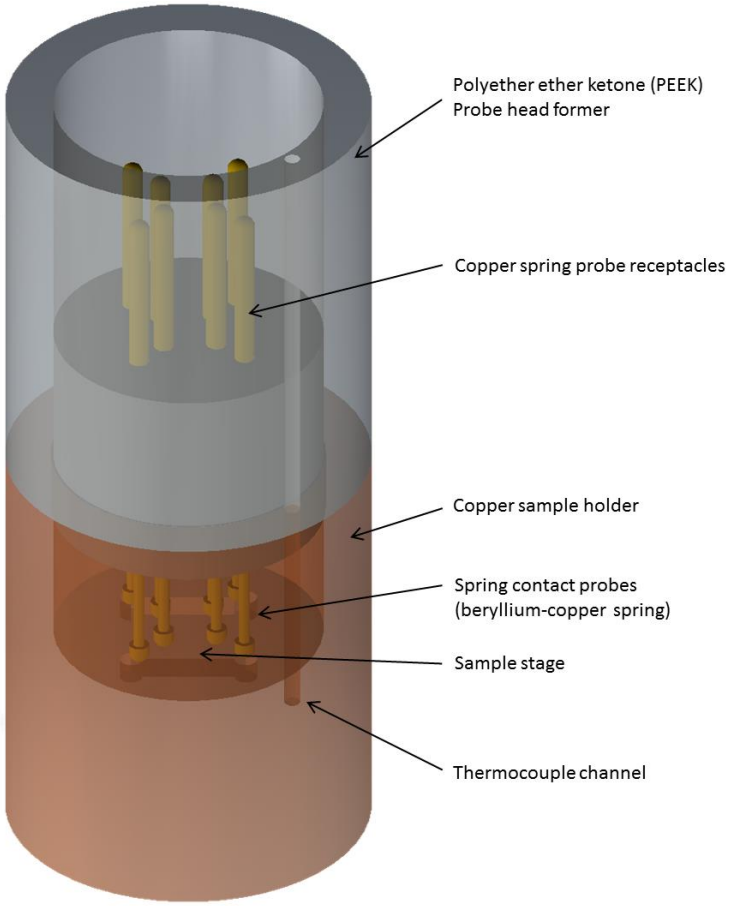

Figure 5.5 - Schematic drawing of the spring probe contact head that was developed for the MR apparatus.

The spring probes chosen were PA1JL-NF probes from Coda Systems. These probes have a diameter of 0.53 mm and have a copper body with a beryllium copper spring with a full travel of 2.54 mm. As the probes are non-ferrous there should be minimal distortion of applied fields at the surface of the sample. To prevent damage to the thin films, the probes were specified with a rounded tip and the lightest spring available, which has an initial spring force of 0.17 N. The copper sample holder was designed to sit the sample at the mid-point of the

working travel of the probes. To make an electrical connection to the probes a receptacle tube was mounted into the probe head former. This allowed solder connections to be made to the receptacle without the heat damaging the spring probe and for probes to be replaced if worn or broken.

When designing the probe head, a number of additional considerations had to be made for the temperatures it would experience. As the upper part of the head houses the spring probe receptacles, it must be electrically insulating. As such it was machined in polyether ether ketone (PEEK). The thermocouple was inserted through a machined channel in the wall of the copper block to locate it as close as possible to the sample. Additionally, all electrical connections to the probes were made using Kapton-insulated wire.

5.3.3 Sample Preparation

The measured resistivity is a combination of a number of different factors. On a fundamental level these are: background scattering due to point defects and phonons, grain boundary scattering and surface scattering. These factors can all be affected by sample preparation, so an understanding of the effects of growth parameters is essential.

The background scattering is controlled mainly by the purity and crystallisation of the film; grain boundary scattering is controlled by the grain size. Both of these factors can be modified through use of deposition parameters such as growth rate, bias voltage, process pressure and substrate choice. This is discussed in more detail in section 6.1.

In bulk crystals, surface scattering has a negligible contribution to the total resistance. However, as the thickness of the sample decreases below the length of the mean free path of electrons in the material, the contribution due to surface scattering will increase rapidly. This increase can be approximated as $\Delta_\rho \propto 1/t_{AF}$ where Δ_ρ is the change in resistivity and t_{AF} is the film thickness [177]. A much more accurate model for the resistance increase in thin films, taking into account random scattering at the interfaces, was presented by Fuchs in 1937 [178]. When preparing samples, it was determined that by making $t_{AF} \geq 50$nm, the contribution due to surface scattering would be sufficiently small as to have no effect on the measurement of T_N.

Additionally, when preparing samples for MR measurements, considerations must be given to the nature of the substrate and the presence of any seed or capping layers. If any of these are

conductive, they could contribute to the sample resistance. Therefore samples produced for MR measurements were grown on insulating substrates such as quartz or SiO_2.

5.3.4 Measurement Control

Using LabView, it is possible to control the two Keithley source-meters for the electrical measurement in addition to the sensors and power supply used for temperature control. The Keithley 2635 is used as a current source due to its wide source range of 1 nA to 10 A, allowing samples of almost any resistance to be measured. The source current must be matched to the sample resistance to provide a voltage drop measureable by the Keithley 2182a nanovolt meter, but not so large as to produce localised heating in the sample.

Current Control and Localised Heating

Traditionally resistance is measured in 4 point probe measurements by applying a continuous current to the source connections and measuring a voltage drop across the sense connections. Through the use of computer automation, it is possible to either pulse or sweep the applied current whilst measuring the voltage drop. This has a number of advantages. By pulsing current, the amount of time that the current is applied is reduced, therefore minimising any heating effects. Using a swept technique and measuring multiple points can increase the accuracy of the result as well as highlighting phenomena such as localised heating, random noise or poor contacts. This is shown in Figure 5.6.

The maximum measurement current (I_{max}) was chosen for each sample to give a voltage drop across the sense contacts >1 μV. This value was chosen as it was the lowest value that the Keithley 2182a nanovolt meter could read reliably to four significant figures. As the sample resistances ranged from $\sim 1\ \mu\Omega$ in bulk single crystals to $\sim 5\ \Omega$ in polycrystalline thin films, I_{max} was set between 1 A and $1\ \mu$A.

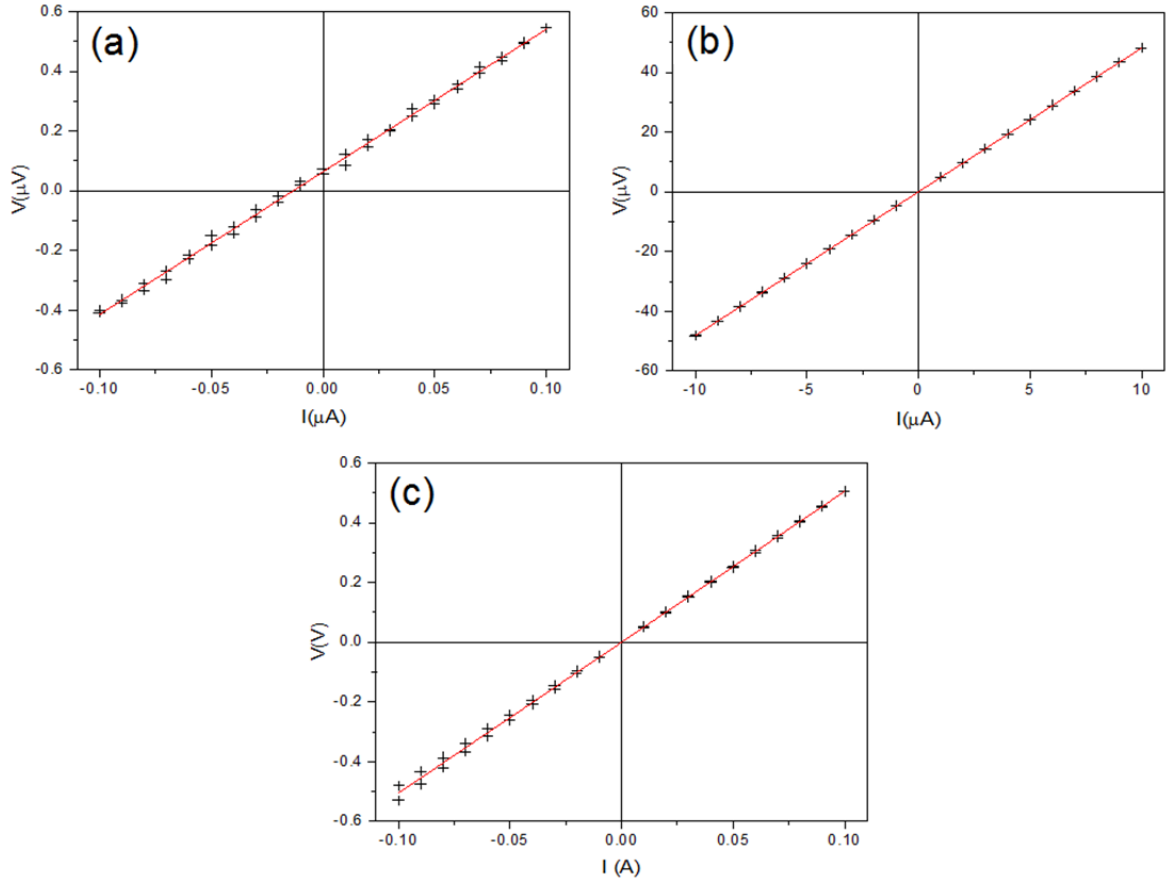

Figure 5.6 – I versus V (IV) measurement data for a 10 nm Pt film with a measured resistance of $(4.81438 \pm 0.00002)\ \Omega$ at room temperature at different source currents (a) $I_{max} = 0.1\ \mu$A, (b) $I_{max} = 10\mu$A, (c) $I_{max} = 0.1$ A.

After a considerable amount of testing, a swept measurement with 21 points evenly spaced between $-I_{max}$ and I_{max} was chosen. This was then repeated, sweeping back from I_{max} to $-I_{max}$ giving a total of 42 points per measurement. Each current value was applied for 0.5s giving a total time of 21 s for each IV sweep. Examples of these measurements are shown in Figure 5.6.

Figure 5.6 shows (a) Insufficient maximum current of 0.1 μA causing noise in the measurement. (b) Good measurement, 10 μA maximum source current. (c) 0.1 A maximum current, resulting in localised heating, evident from the splitting of the data in the 3rd quadrant of the graph. Conducting the experiment in this manner has a number of advantages, in that it allows easy determination of the quality of the resistance measurement. Additionally, this method can be used to disregard any erroneous data points that occur due to fluctuations in the mains ground due to other equipment in the laboratory.

To find the resistance from the IV data, a linear fit is plotted and the Pearson's correlation coefficient (r) calculated. By doing this, and comparing the r value, it is possible to determine automatically when spurious data have been collected and to disregard them. Any erroneous data points can then be can then be repeated before the temperature set point is changed. The measurement procedure is shown schematically in Figure 5.7.

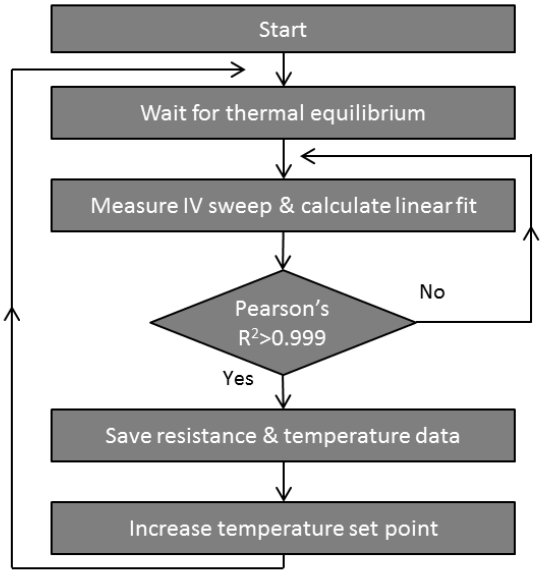

Figure 5.7 - Flow chart showing measurement procedure for the Néel Temperature measurement technique.

Depending on the step size between each temperature set point, the system takes from 3-15 minutes to equilibrate before a new data point can be measured. Using this method a typical Néel temperature measurement (100 K in 1 K steps) takes around 7 hours. It is possible to sweep the temperature rather than measure at equilibrium to reduce the measurement time, but this does not allow the repeat of any erroneous data points.

5.4 Calibration and Initial Measurements

After initial assembly of the apparatus, it was necessary to test and calibrate the system. The temperature sensors were calibrated at 77.35 K and 273.15 K before assembly of the cryostat. Thin film platinum and single crystal chromium samples were chosen to test the performance of the system as a whole. Thin film platinum was chosen as its resistance has a perfectly linear response to temperature and it could be prepared using a sputter target already available, without the need for any capping layers to prevent oxidation. Chromium

was chosen as it is a single element antiferromagnet with a well-defined Néel temperature ($T_N = 311$ K [42]) which is easily accessible using the Oxford Instruments cryostat. A single crystal sample was chosen so there would be no contribution to the resistance from grain boundary scattering or from surface scattering, meaning the cusp in the resistivity at T_N should be visible.

5.4.1 Thin Film Platinum Calibration

Figure 5.8 shows a perfectly linear relationship between temperature and resistance for the 25 nm thick Pt film indicating that both the temperature sensor and electrical measurement are working correctly. The data were collected using the method outlined in Figure 5.7 with a temperature step of 1 K. As the measurement was conducted using a Van der Pauw geometry, only a sheet resistance measurement is possible, meaning calculation of the temperature coefficient of resistance for comparison to the bulk value for Pt is not possible. The large value of resistance obtained can be explained by the thickness of the film becoming comparable to the mean free path of electrons resulting in a sharp increase in the amount of surface scattering present [179].

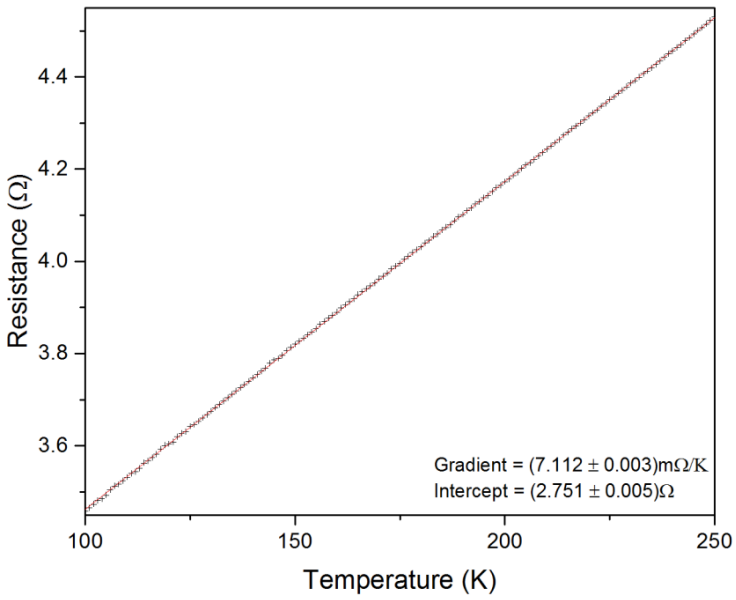

Figure 5.8 - Measurement of resistance as a function of temperature for a 25 nm thick Pt film.

5.4.2 Measurement of T_N in Single Crystal Chromium

An anomaly in the resistivity data for chromium near room temperature was first observed by Bridgman in 1933 [180]. It was not explained correctly until neutron diffraction measurements highlighted the antiferromagnetic to paramagnetic transition 30 years later [42, 181]. This prompted more work into the use of MR measurements for the determination of Néel transitions. Stebler was able to accurately measure T_N in a large single crystal Cr sample using a MR measurement over 17 days shown previously in Figure 5.1 [167].

To assess the applicability of the MR apparatus for measurement of T_N a 5 x 5 x 1 mm single crystal Cr sample was obtained from Goodfellow Cambridge Ltd.

It was possible to measure accurately the resistance using an IV sweep from -0.1 to 0.1 A at each point. Although this current is very high compared to typical thin film measurements, due to the extremely low resistance of the sample the amount of energy dissipated is small meaning there is no observable localised heating. From calculation, the peak heating rate of the sample due to the current is 1.36×10^{-5} Ks^{-1} ignoring any heat transfer to the copper sample stage. Figure 5.9 shows 150 of these measurements each separated by a temperature step of 0.5 K, from 250 K to 325 K obtained over 5 hours.

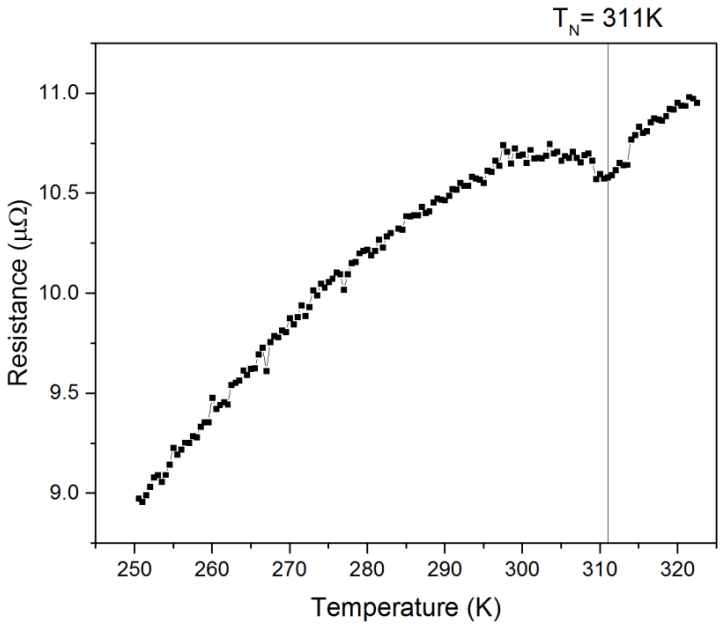

Figure 5.9 - Measurement of the Néel Temperature in single crystal Cr.

Between 305 K and 315 K a clear anomaly in the resistivity is observed with its minimum at (311 ± 3) K demonstrating the measurement developed is capable of resolving the change in resistance due to the reordering of the magnetic structure of the material. It is important to note that the magnitude of this anomaly is $\sim 2 \times 10^{-7}\ \Omega$..

Chapter 6: Sample Preparation and Characterisation

In this chapter, the main experimental techniques used for fabrication, as well as magnetic and structural characterisation of thin films, are described. The samples studied were produced by sputtering, using the High Target Utilisation Sputtering (HiTUS) system in York, or the DC/RF Magnetron system in Bielefeld. Structural characterisation was conducted using X-ray diffraction (XRD), X-ray reflectivity (XRR) and transmission electron microscopy (TEM). Finally, the magnetic characterisation of the samples using a vibrating sample magnetometer (VSM) and alternating gradient force magnetometer (AGFM) is discussed.

6.1 Thin Film Deposition

A thin film is a layer of material ranging from a single monolayer up to a few micrometres in thickness. There are a number of techniques used for production of this type of metallic sample, the most common being Molecular Beam Epitaxy (MBE) and direct current (DC) or radio frequency (RF) sputtering.

MBE is a method of thin film deposition relying on either high temperatures or electron beams to sublimate a target material before depositing it onto a crystalline substrate. MBE is widely used in the manufacture of semiconductor devices as it allows growth of high quality, single crystal materials. This is possible due firstly to the low growth rates, typically below 0.1 nm s^{-1}, allowing materials to be deposited epitaxially and secondly because of the absence of any carrier gas during deposition. This means ultra-high vacuum (UHV) operating pressures $< 1 \times 10^{-9}$ mbar have to be used. Although useful for the semiconductor industry, single crystal materials are not usually desired for industrial magnetic materials as their magnetic reversal mechanism is controlled by domain wall pinning at inclusions or crystal defects, which are by their nature unpredictable, additionally the cost of manufacture can be prohibitive.

Sputtering is a process that uses a DC bias voltage applied to a high energy plasma which is incident on the target material. Momentum is transferred from the ions in the plasma to atoms in the target material resulting in ejection of atoms from the target surface. When using a DC bias voltage, only metallic target materials can be sputtered. If an insulating target material is used this would lead to a negative charge accumulation at the target surface meaning a plasma cannot be maintained. This can be avoided by using an AC voltage supply, in practice, a RF frequency of 13.56 MHz is used [182]. Additionally, this RF electric field can increase the rate of ionisation of gas molecules, improving the deposition rate. This process is called RF sputtering.

Due to the requirement of a gas for generation of the ion beam, the operating pressure of sputter deposition systems is typically 1×10^{-2} to 1×10^{-5} mbar leading to a wide variety of sputter deposition rates ranging from 0.5 to 5 nm s^{-1}, controlled using a variety of techniques. Sputtering allows control over the deposition process resulting in high quality polycrystalline films. Due to these reasons, sputtering is the predominant method of production of magnetic thin films in industry.

6.1.1 Magnetron Sputtering

The desire for higher deposition rates at lower operating pressures led to the development of magnetron sputtering. By producing a strong transverse magnetic field of up to 1 T behind the target, the ionisation of the gas at the targets surface is increased by up to an order of magnitude [182]. Figure 6.1 shows an example of a magnetron sputtering system.

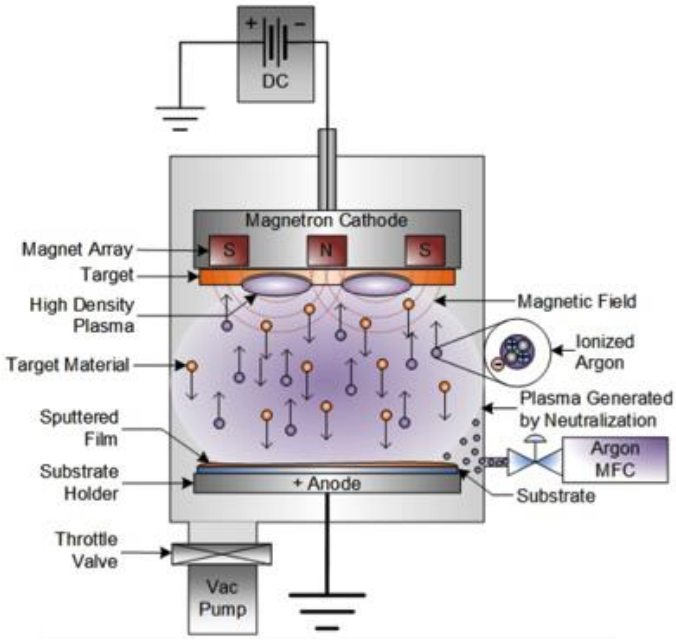

Figure 6.1 - Schematic diagram of the magnetron sputtering process [183].

The magnetic field at the surface of the target forces the electrons to follow helical paths causing an increase in plasma density at the target surface. This higher density plasma has a number of benefits. Primarily it will allow a glow discharge to be initiated at lower gas pressures, typically below 10^{-3} mbar. Furthermore it will greatly increase the deposition rate from the target, though only in the high density areas of the plasma. This leads to an erosion track, referred to as a 'racetrack', on the target surface that can severely limit the lifetime of the target. Additionally, as the field at the surface of the target is produced by a magnet array behind the target the thickness of the target is limited to ~5 mm. Industrial systems use complex magnet configurations as well as different shaped targets to combat these problems.

In magnetron systems, alloy materials can be deposited either from composite targets, or using a technique called co-sputtering. Co-sputtering is where two or more target materials are sputtered simultaneously from separate magnetron sources in the vacuum chamber. As the power of each magnetron source can be varied individually it is easy to control the stoichiometry of the resulting alloy produced. It is also possible to introduce a reactive gas into the chamber during growth, allowing compounds such as oxides and nitrides to be grown, this process is called reactive sputtering [182].

In this work, two sputter deposition systems are used: a customised 4 source magnetron system and the HiTUS 8 target system. The specification and advantages of these systems are detailed in sections 6.1.2 & 6.1.3.

6.1.2 BESTEC 2" DC/RF Magnetron Deposition System

The magnetron sputtering system used in this work was a 4 target confocal system produced by BESTEC in Germany. The system has 3 DC and 1 RF magnetron sources each designed for a 2" target. The sources are arranged confocally in the growth chamber as shown in Figure 6.2. To ensure a homogeneous deposition over the full area of the substrate, an angle of α = 21.1˚ was calculated for a target to sample distance of d_{TS} = 134.1 mm. This distance was used as it was equal to the distance to the crystal growth rate monitor when inserted. This allowed accurate in-situ measurement of growth rates. Additionally, to prevent textured or non-homogeneous growth, due to the angle of incidence of the source, the sample stage can be rotated at frequencies up to 10 Hz.

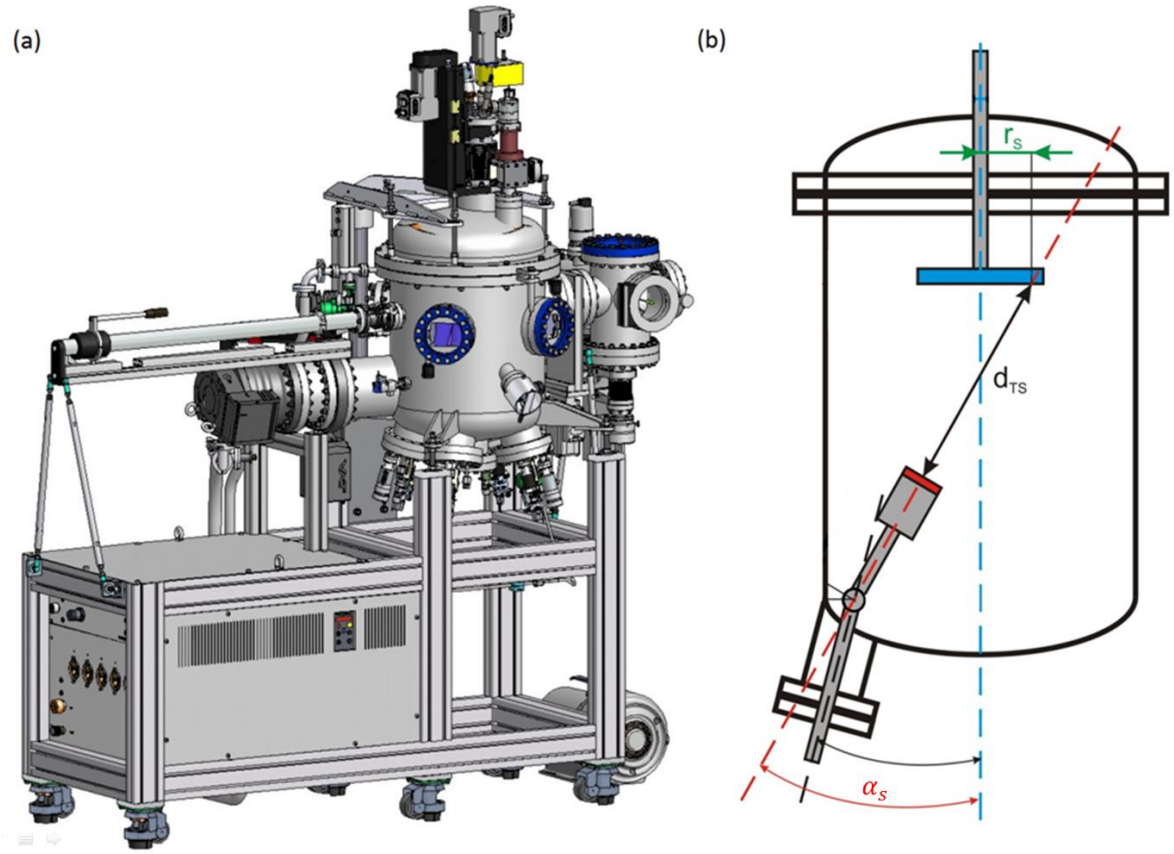

Figure 6.2 - (a) BESTEC 2" Quadruple source Magnetron Sputter Deposition System. (b) Schematic diagram showing confocal geometry for one of the four sources where r_s is the

radius of maximum substrate size, d_{TS} is the distance between source and substrate and α_s is the source tilt angle [184].

Figure 6.2(a) shows the BESTEC system. The 4 confocal magnetron sources are mounted on the bottom of the main chamber, turbo molecular pump and transfer arm on the left, sample rotation stage and heater on the top, and load-lock chamber on the right. The use of a separate load-lock chamber allows the system to maintain a base pressure below 10^{-8} mbar. When beginning deposition, a bias voltage of 800 V is applied to the target material to ignite the plasma. After ignition, the sources are operated in constant power mode. Typical operating pressure is 2×10^{-3} mbar of high purity (N6.0) Ar gas. Both the composition and pressure of the sputter gas can be varied to control the growth of the sample. Additionally, a radiative heater is mounted behind the sample stage allowing for the substrate to be heated to over 1000 K during deposition.

6.1.3 High Target Utilisation Sputtering (HiTUS)

The magnetron sputtering technique has certain limitations and most of these stem from the requirement that the plasma be generated at the sample surface. In the HiTUS system, developed by PlasmaQuest Ltd., the plasma is generated outside of the main chamber. Doing this allows the plasma density to be varied independently of the target bias voltage.

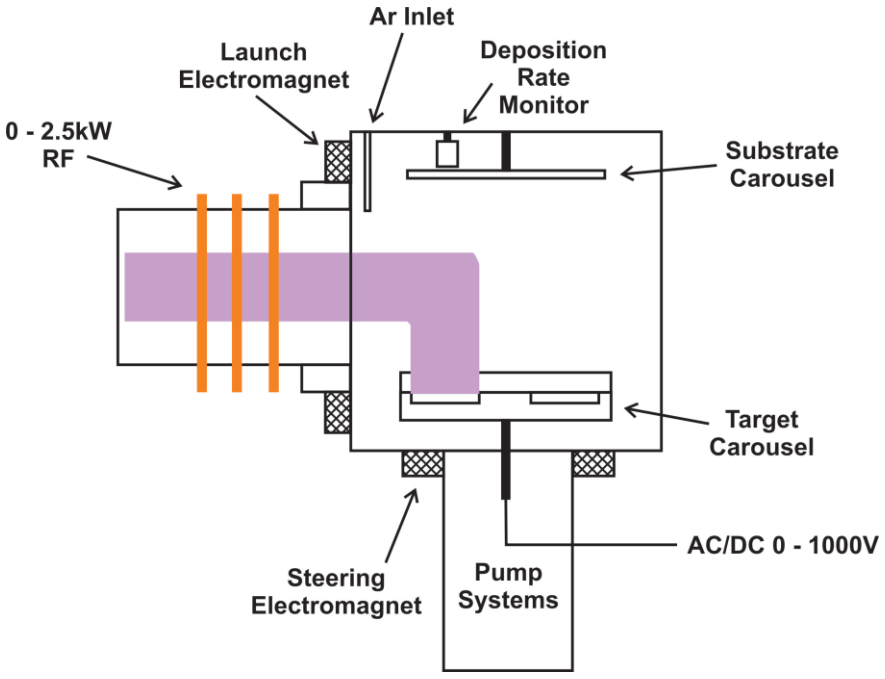

Figure 6.3 - Schematic Diagram of the HiTUS deposition system [185].

The plasma in the HiTUS system is generated in a side arm using a 13.56 MHz, 2.5 kW three turn RF antenna, shown in Figure 6.3. Through control of the RF power and operating pressure, the plasma density can be controlled between 10^{12} to 10^{14} cm^{-3} [185]. The plasma can then be guided to the target surface through the use of magnetic fields. Alternatively the plasma can be guided into the main chamber and used to clean substrate surfaces, allowing for removal of oxide layers before growth. During growth, a co-axial magnetic field with strength of 50 Oe is generated by the launch electromagnet, accelerating the plasma ions into the main chamber producing a continuous plasma beam. This beam is then steered onto the target surface using a second electromagnet with a magnetic field of ~500 Oe as shown in Figure 6.3.

At this point the plasma does not have sufficient energy to sputter atoms from the target surface. To accelerate the plasma, a DC bias voltage of 100 -1000 V is applied to the target allowing sputtering to occur. At voltages above 100 V the target current saturates and is independent of the voltage [186]. The deposition rate can be controlled using this voltage independently of the plasma generation. As the magnetic field at the surface of the target is near homogeneous, the target material is used much more evenly, giving over 90% target utilisation. This can be seen by comparison of Figures 6.4(a) and (b).

Due to the method of plasma generation, the HiTUS system cannot sputter from multiple targets simultaneously. In order to grow alloy materials, a composite target must be used. These targets can either be solid or powder pressed. As the sputter yield of an element is dependent on a number of factors, including melting temperature and atomic mass, it could be assumed that the stoichiometry of samples sputtered from a composite target would not have an equal stoichiometry to the target. However, as only surface atoms can be sputtered, if the sputtering rate is much higher for one element, its concentration at the surface will be reduced counteracting the difference in deposition rates. This does however highlight the need for target conditioning before growth. Additional control of the stoichiometry can be achieved using doping pegs. These pegs are mounted to the target surface using holes as seen in Figure 6.4(c).

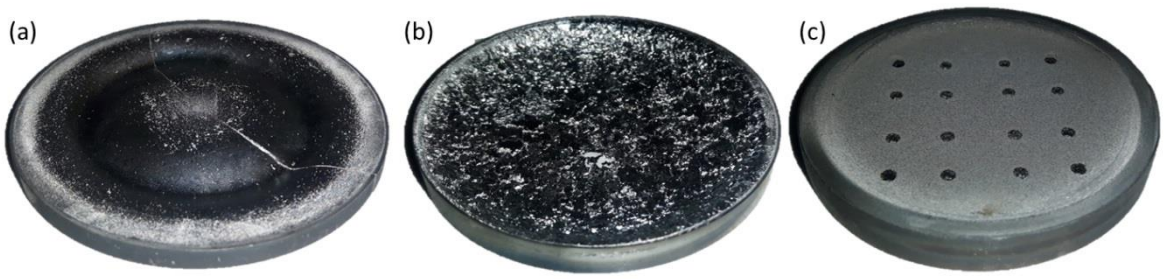

Figure 6.4 - (a) Used magnetron target with erosion 'racetrack'. (b) Alloy HiTUS target with high utilisation (0 mm thickness at centre 6 mm at edges) (c) Powder pressed HiTUS target with holes to allow doping pegs to be inserted.

The HiTUS system has a water-cooled target carousel that holds 8 targets and a substrate carousel with 6 positions. The target and substrate carousels are separated by ~300 mm, this large separation ensures there is no re-sputtering from deposited films and that there is adequate intermixing of sputtered materials to allow for uniform growth on multiple substrates simultaneously. Substrate temperatures are typically <350 K during deposition.

This system allows for up-to 6 samples, with unique structures, to be deposited each time the system is evacuated. The base pressure of the system is 2×10^{-7} mbar with pressures below 10^{-6} mbar achievable after 3 hours due to the 3 stage pumping system. After initial evacuation of the chamber, the plasma source is used to clean the inner walls of the system and can also serve to getter the system further improving the base pressure. The operating pressure of the system (1×10^{-3} to 4×10^{-2} mbar) is controlled using a 4 channel mass flow controller. Unless stated otherwise, the standard sputter gas used was Ar (N5.5) at a pressure of 2.50×10^{-3} mbar. Reactive sputtering is possible through utilisation of the remaining three gas channels, for MnN samples produced in this work a 1:1, N_2:Ar gas mix with N_2 (N5.5) was used.

6.1.4 Sputter Rate and Grain Size Control

As stated in section 6.1.3, the HiTUS system offers significant control of the plasma density through variation of the RF power, operating pressure and target bias voltage. Varying the plasma density allows control of the sputter rate and grain size of the deposited film. Higher plasma densities will cause an increase in the deposition rate, however the effect of this on grain size was unknown. An investigation into these effects was first conducted by Vopsaroiu

et al. in 2004, where the RF power, operating pressure and target bias voltage were each varied for 50 nm Cr thin films. The results of this study are summarised in Figure 6.5.

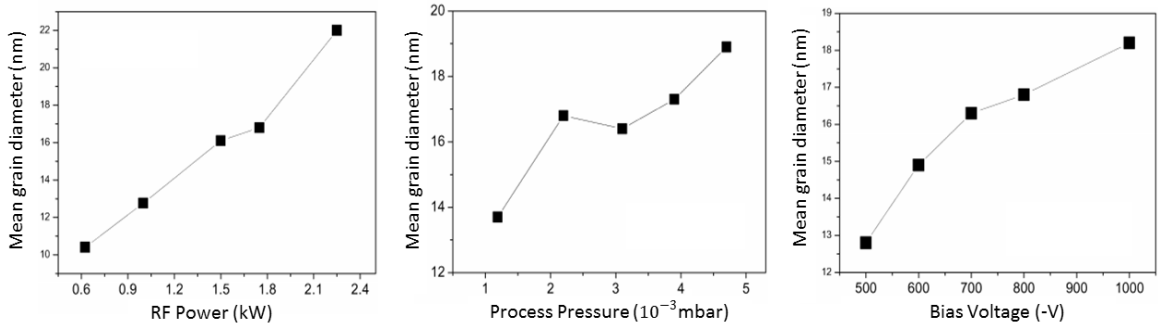

Figure 6.5 - Control of mean grain size in Cr thin films using (a) RF Power, (b) Operating pressure and (c) Target bias voltage [185].

A clear correlation is observed between the grain size and plasma density showing the mean grain size could be varied between 10 and 20 nm through variation of any of the sputtering parameters.

6.1.5 Growth Rate Calibration and Monitoring

Both sputter deposition systems used in this work are fitted with quartz crystal deposition rate monitors for in-situ monitoring. In the HiTUS system, the growth rate can be monitored during deposition. However in the BESTEC Magnetron system, there is no space to mount the deposition rate monitor next to the sample during growth, so it can only be used when the sample stage is retracted.

Quartz crystal deposition rate monitors use a quartz crystal microbalance as the sensor. As material is deposited onto the quartz crystal its resonant frequency will decrease as a function of the mass deposited. If the density of the deposited material is known, the growth rate can then be calculated.

Calibration of the crystal rate monitor is necessary each time the sensor is replaced. This can be done post deposition, using either a depth measurement between an area of a sample with deposited film and without deposited film using Atomic Force Microscopy (AFM), or through the use of XRR, described in detail in section 6.2.2. The difference between this

calibrated thickness and estimated thickness can then be used to calculate a tooling factor for the crystal rate monitor to improve thickness accuracy in subsequent growths.

6.2 Structural Characterisation

The magnetic and electrical properties of a system are defined by the physical properties of the film. These include the orientation, the crystallite and grain size, the density, the strain and the roughness of the sample. Through the use of advanced X-ray techniques and electron microscopy, all of these parameters can be measured. Properties such as orientation, strain and grain size can be measured using both techniques allowing measurement over macroscopic length scales, providing a mean value for a larger area of material using XRD, or for a single grain or crystal using TEM. Through measurement of large numbers of single grains, it is also possible to produce a distribution chart of the structural properties of the sample. In this section, the structural and compositional characterisation methods used in this work are described in detail.

6.2.1 X-ray Diffraction

In X-ray diffraction, an X-ray source is used to irradiate the sample. These X-rays are diffracted by the crystal planes of the sample, dependent on the incident angle of the radiation. When the incident angle of the radiation matches the Bragg condition, constructive interference occurs [187]. This condition is given by Bragg's Law:

$$n\lambda = 2d_{hkl}sin\theta, \qquad n = 1,2,3 \ldots \tag{6.1}$$

where n is the diffraction order, λ is the wavelength of the incident radiation, d_{hkl} is the crystal plane spacing and θ is the diffraction angle. Analysis of this diffraction pattern as a function of angle, allows the identification of the lattice parameter, crystalline phases, texture, crystallite size and lattice strain for a given sample. Details of these measurement types are given below.

Lattice Parameter Measurement

Depending on the geometry of the system, both the in-plane and out of plane lattice parameters can be measured. The most common geometry used for out of plane measurements is the Bragg-Brentano $\theta/2\theta$ geometry [188], shown in Figure 6.6.

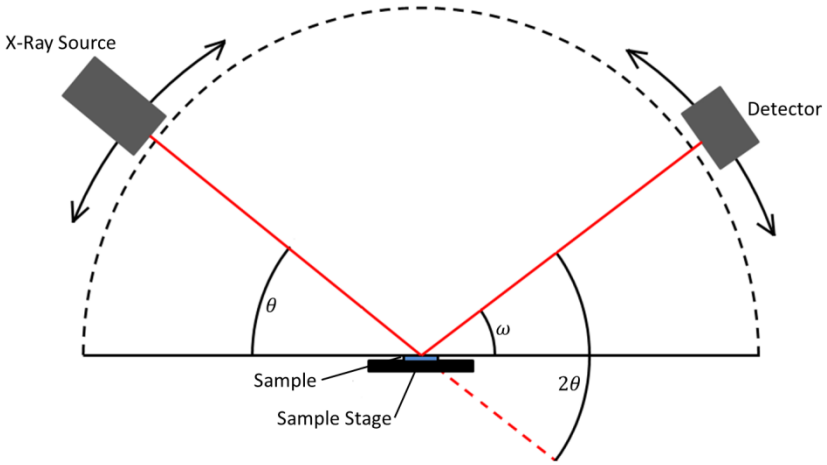

Figure 6.6 - Schematic diagram showing Bragg-Brentano geometry for a $\theta/2\theta$ measurement.

In this geometry, both the X-ray source and detector are scanned by an angle θ while the sample remains stationary, allowing determination of the crystal plane spacing given by equation 6.1. As the sample remains stationary during measurement, the angle ω (sample tilt) is equal to θ at all points. The lattice spacing (d_{hkl}) can be expressed in terms of the corresponding Miller indices $[hkl]$ for the observed peak, to then calculate the crystal lattice parameter α. For a cubic system d_{hkl} is given by:

$$d_{hkl} = \frac{\alpha}{\sqrt{h^2 + k^2 + l^2}} \tag{6.2}$$

To measure the in-plane lattice parameter, the same measurement type can be performed by fixing the source and detector in the plane of the sample and rotating the sample stage by angle χ and the detector by angle ϕ in the plane of the sample as shown in Figure 6.7. This measurement is referred to as a 2θ χ/ϕ plot.

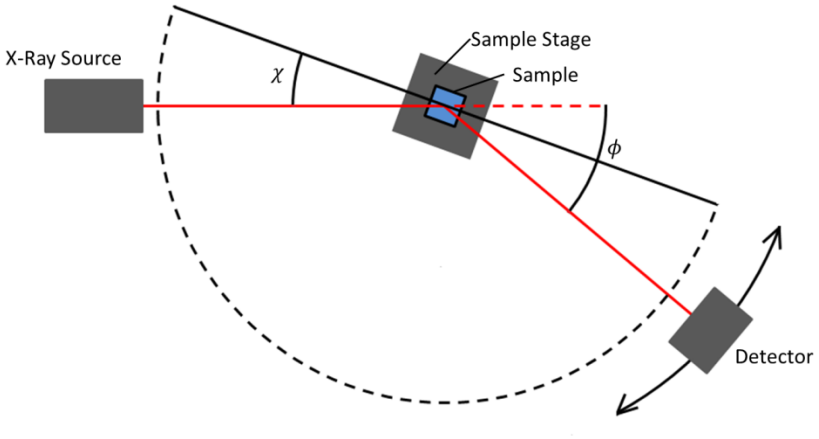

Figure 6.7 - Schematic diagram showing in-plane geometry for $2\theta\ \chi/\phi$ measurement.

When making in-plane measurements, the height and χ alignment of the sample is critical, especially when measuring textured samples. If alignment criteria are not met, no peak will be observed. Alignment of the XRD system is described later in this section.

Particle and Crystallite Size Analysis

In addition to calculation of lattice parameters, an estimate of the crystallite size within the film is possible by measuring the broadening of a diffraction peak for a $\theta/2\theta$ scan. The Scherrer equation is used to relate the peak broadening to crystallite size, given by [189]:

$$D_{cry} = \frac{f_s \lambda}{\beta cos\theta} \tag{6.3}$$

where D_{cry} is the crystallite size, f_s is a dimensionless shape factor and β is the line broadening of the peak after subtraction of instrument broadening. It is important to realise that the Scherrer equation only provides an estimate of the grain size, as it assumes crystallite size is the only contribution to peak broadening for a symmetric peak. In reality, factors such as strain, dislocations and grain boundaries can also lead to peak broadening and asymmetry. When both crystallite size and microstrain are present, the accuracy of this method can be improved by accounting for broadening due to lattice strain using the Williamson-Hall equation [190]:

$$\beta = 4\ \epsilon_{cry} \frac{sin\theta}{cos\theta} \tag{6.4}$$

where ϵ_{cry} is the crystal strain. Equations 6.3 and 6.4 can be combined to give:

$$\beta\ cos\theta = \frac{K\lambda}{D_{cry}} + 4\ \epsilon_{cry}\ sin\theta \tag{6.5}$$

This is known as a Williamson Hall plot. Multiple points can be measured and then fitted allowing for a more accurate determination of both the crystallite size and strain in the sample.

Texture and Quality Analysis

XRD can be used to measure crystalline orientation, strain and quality in thin film materials. This is due to a collection of diffraction data from a large area of the sample allowing quantitative analysis of the full film volume. In this section two measurement types will be described, rocking curves and pole figure scans. Rocking curves are predominantly used to study crystal quality and strain. They are performed by fixing the 2θ angle on the diffraction peak of interest then scanning the angle ω as shown in Figure 6.8.

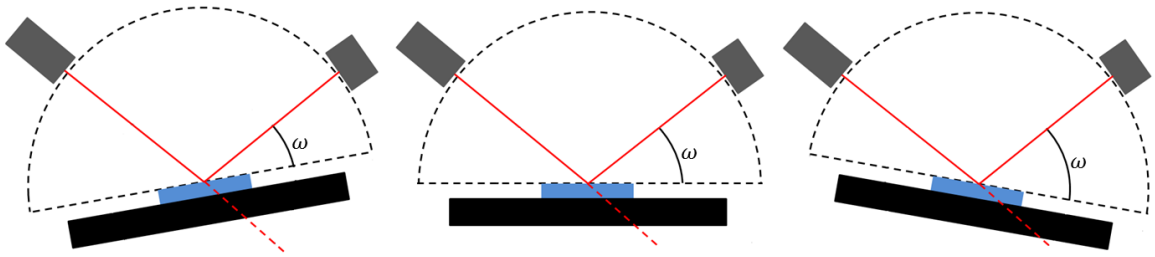

Figure 6.8 - Schematic diagram showing XRD geometry for ω scan (Rocking curve).

In a perfect crystal, a very sharp peak will be observed when the crystal is tilted so that its crystallographic orientation is parallel to the diffraction vector. The width of this peak is determined only by instrument broadening and the spectral width of the source. If the crystal has any imperfections, these will cause a broadening of the rocking curve due to a distribution of the crystallographic orientations within the sample. Through simulation and fitting of rocking curve data, quantitative values of lattice strain, thickness and composition can be obtained [191, 192]. If more information is required, multiple rocking curves can be

measured as a function of the 2θ angle. This measurement type is known as a reciprocal space map.

To obtain information about the preferred crystallographic orientation or texture, a pole figure scan can be used. A pole figure scan is a coupled ψ (sample rotation perpendicular to plane), χ (sample rotation in plane) scan as shown in Figure 6.9 (a). At each ψ step a full 360° χ scan is performed. These data can then be plotted as a 3D pole figure, an example of which is shown in Figure 6.9 (b).

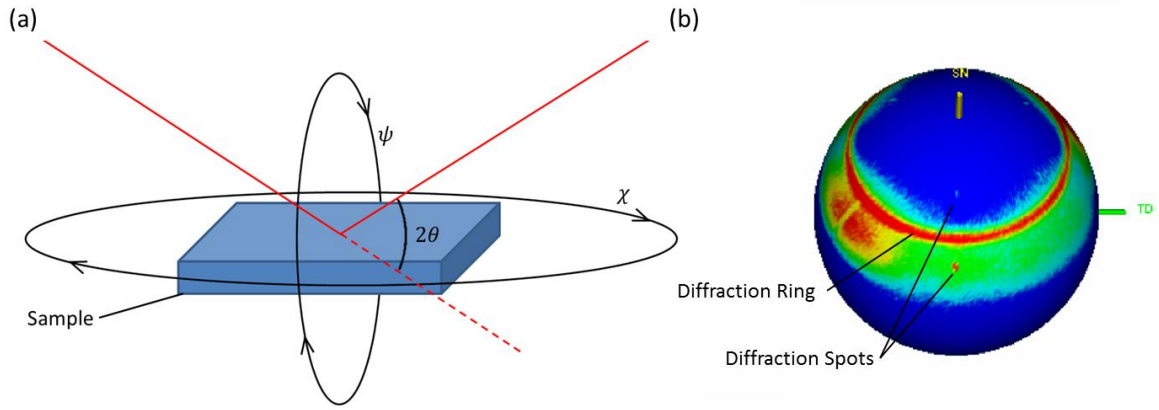

Figure 6.9 - (a) Coupled χ and ψ scan at fixed 2θ angle to produce pole figure scan (b) 3D pole figure for polycrystalline Ni_2MnAl thin film sample on MgO substrate fixed on the MgO (220) peak showing diffraction rings and spots.

From this 3D pole figure scan it is possible to collect information about the orientation of the crystal. Crystal planes with well-defined orientation will appear as sharp diffraction spots. Un-textured polycrystalline samples will show diffraction rings due to the absence of preferential crystal orientation. In Figure 6.9(b) the groups of three diffraction spots at 34° and 59° are due to the MgO (111) family of lattice planes. The ring at 45° is due to the Ni_2MnAl (220) lattice plane showing no preferential orientation of the Heusler alloy.

Rigaku 9kW Smart Lab Diffractometer

All XRD and XRR measurements performed in this work were made using a Rigaku SmartLab 9 kW diffractometer. The system has a 9 kW rotating copper anode generator with multilayer mirror optics producing a high brightness focal spot equal to a standard 18 kW generator. This allows the use of parallel beam optics and a germanium monochromator whilst keeping the typical measurement time below 1 hour. The diffractometer is equipped with a 6 axis

goniometer with an angle resolution of 0.0001°. Additionally, the sample stage can be equipped with either a translation stage for automated XY mapping of multiple samples or a tilt stage, allowing sample tilt alignment for reciprocal space map measurements [193]. The instrument is configured with cross beam optics that allow switching between direct beam (Bragg-Brentano) and parallel beam configurations.

X-ray Optics & Alignment

Precise alignment of the X-ray optics and sample are necessary when performing XRD or XRR measurements. Methods for alignment are well established and are mostly automated when using the Rigaku SmartLab software. Alignment can be split into two parts: X-ray optics alignment and sample alignment. In this section, a brief overview of these alignments is given. A full description of these alignments can be found in the Rigaku user manual [193].

Optical alignment is necessary each time any of the incident or detector optics are changed. The Rigaku system used in this work has separate alignment axes for incident arm height, monochromator alignment, incident and detector slit heights and $\theta/2\theta$ offset. Each of these axes is aligned by searching for the peak intensity position.

Sample alignment is carried out each time the sample is changed or moved on the stage. It consists of two main scans: stage height and ω offset calculation. These scans are repeated until no improvement in the peak signal can be made. Examples of these scans are shown in Figure 6.10.

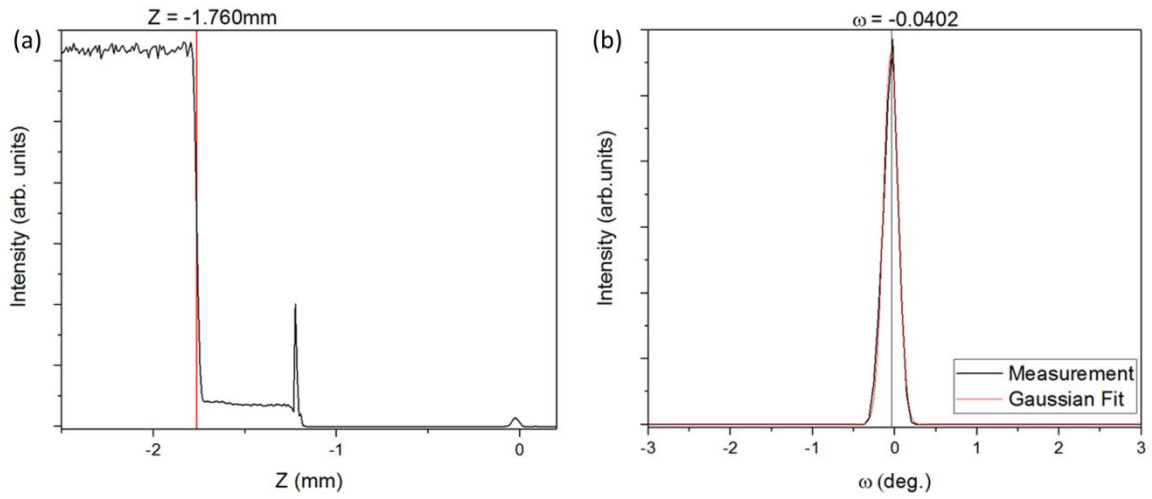

Figure 6.10 - Example sample alignment scans for (a) Direct beam half cut Z alignment showing -1.760 mm offset and (b) sample tilt ω alignment showing -0.0402° offset.

In Figure 6.10(a) the sample stage is driven up into the beam path and the point at which the beam is cut to half intensity calculated. In Figure 6.10(b) angle ω is scanned and peak intensity found. Additionally, when conducting in plane measurements with textured or single crystal samples the stage rotation angle χ must be aligned to ensure the in plane crystal direction is perpendicular to the direct beam.

6.2.2 X-ray Reflectivity

XRR is a surface-sensitive analytical technique used to measure the electron density perpendicular to the surface. This data can be used to obtain information about the film thicknesses, roughness and density. The technique is similar to the $\theta/2\theta$ measurement shown in Figure 6.6, but at angles of incidence close to the critical angle of total reflection. A typical reflectivity curve consists of two components: the Fresnel reflectivity and an interference pattern due to scattering at different layers of the sample. This set of interference peaks are known as Kiessig fringes [194].

XRR measurements are analysed by fitting simulated data to the measured data. Simulated data are calculated using the Rigaku Globalfit software package. Normal fitting parameters are: thickness, roughness and density, for the substrate and each film layer. Additional parameters for scale factor, background and beam divergence can be fitted to improve the correlation between simulated and calculated data. Figure 6.11 shows measured and calculated XRR data for three Tantalum films of nominal thickness 10, 15 and 20 nm.

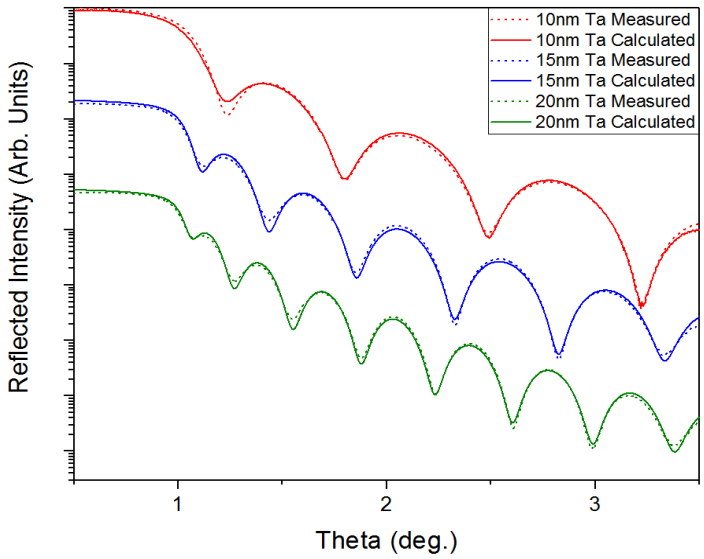

Figure 6.11 - XRR data for 10, 15 & 20 nm Ta thin film samples.

This type of measurement is used for calibration of the crystal growth rate monitor described in section 6.1.5. The table below shows the fitting parameters used in Figure 6.11.

Table 6.1 - XRR Fitting parameters for Ta thin film samples.

Sample	Thickness (nm)	Density (gcm^{-3})	Roughness (nm)
10 nm Ta	11.5	15.46	0.57
15 nm Ta	16.7	15.63	0.58
20 nm Ta	21.8	15.79	0.61

By comparing the thickness reported by the crystal rate monitor during growth and the XRR measured thickness, it is clear that the growth rate monitor is over estimating the thickness of material deposited by 9 to 15%. This variation is due to the increasing density of the Ta with increasing layer thickness towards the bulk value of 16.60 gcm^{-3} [195].

6.2.3 X-ray Fluorescence Spectroscopy

X-ray Fluorescence Spectroscopy (XRF) is a fast and non-destructive technique used for compositional analysis. The sample is irradiated with X-rays with sufficient energy to excite core level electrons in the material. When higher level electrons fill these vacancies, they will emit a photon with an element specific energy. The most important transitions to consider are K_α, K_β, L_α and L_β. These transitions have energy equal to the difference in energy between the initial and final orbitals. The wavelength of these transitions can be calculated

using Planck's Law. Due to lighter elements having a reduced absorption cross section, this technique is only generally applicable to elements with atomic mass greater than 12 [196].

The resulting emission spectrum is recorded using a multi-channel detector, and can then be evaluated after removal of background signal and smoothing of the data. Evaluation of element specific peaks allows the determination of the composition of the irradiated material. The system used in this work uses a 40 keV Ag anode X-ray tube and AMPTEK XR-100CR Si-PIN detector. Samples analysed using XRF, are deposited onto amorphous glass substrates to prevent diffraction peaks and analysed in a He atmosphere, as otherwise, characteristic emission of light elements would be absorbed by air. The typical integration time used was 2 hours.

6.2.4 Grain Size Analysis

Although an estimate of the mean crystallite size is obtainable through the use of Scherrer broadening (described in section 6.2.1), more detailed information about the grain size distribution was a requirement in this work. The only method which allows this type of measurement, is transmission electron microscopy (TEM). To produce in plane TEM images the sample must be electron transparent (typically below 100 nm [197]). This is normally achieved by simultaneously growing samples on both silicon substrates, for normal characterisation, and on copper fine mesh TEM grids, for grain size analysis. Unfortunately, when using lattice matched crystal substrates, or growth systems not designed for simultaneous sputtering of multiple substrates this is not possible. In these cases, sample thinning must occur post growth using a combination of mechanical polishing and focussed ion beam (FIB) milling to thin the sample to electron transparency.

In-Plane Sample Thinning

As mentioned above, it is not always possible to simultaneously sputter TEM grids to allow measurement of the grain size distribution using TEM. In these cases, a combination of mechanical polishing and FIB milling is used. Typically before thinning, samples are 500 µm thick. Using an optical polisher with 14, 6, and 1 µm diamond suspension polishes, it is possible to reduce this to < 50 µm. At this point, the sample is cut and glued into a TEM slot grid, allowing it to then be mounted into a microscope sample stage.

The FEI Inc. FIB system used in this work has both an electron column as typical in a scanning electron microscope (SEM) and an ion beam column mounted at 52˚ to the electron column. When the sample is inserted, the electron beam is used to scan the sample to find a clean area to work in. The sample is then manipulated inside the chamber to align the ion beam with the edge of the sample, and the electron beam on to the lower surface of the sample at an angle of 38˚ to the perpendicular. This orientation allows monitoring of the ion beam milling progress using the electron beam. To avoid contamination of the electron column, imaging is done intermittently.

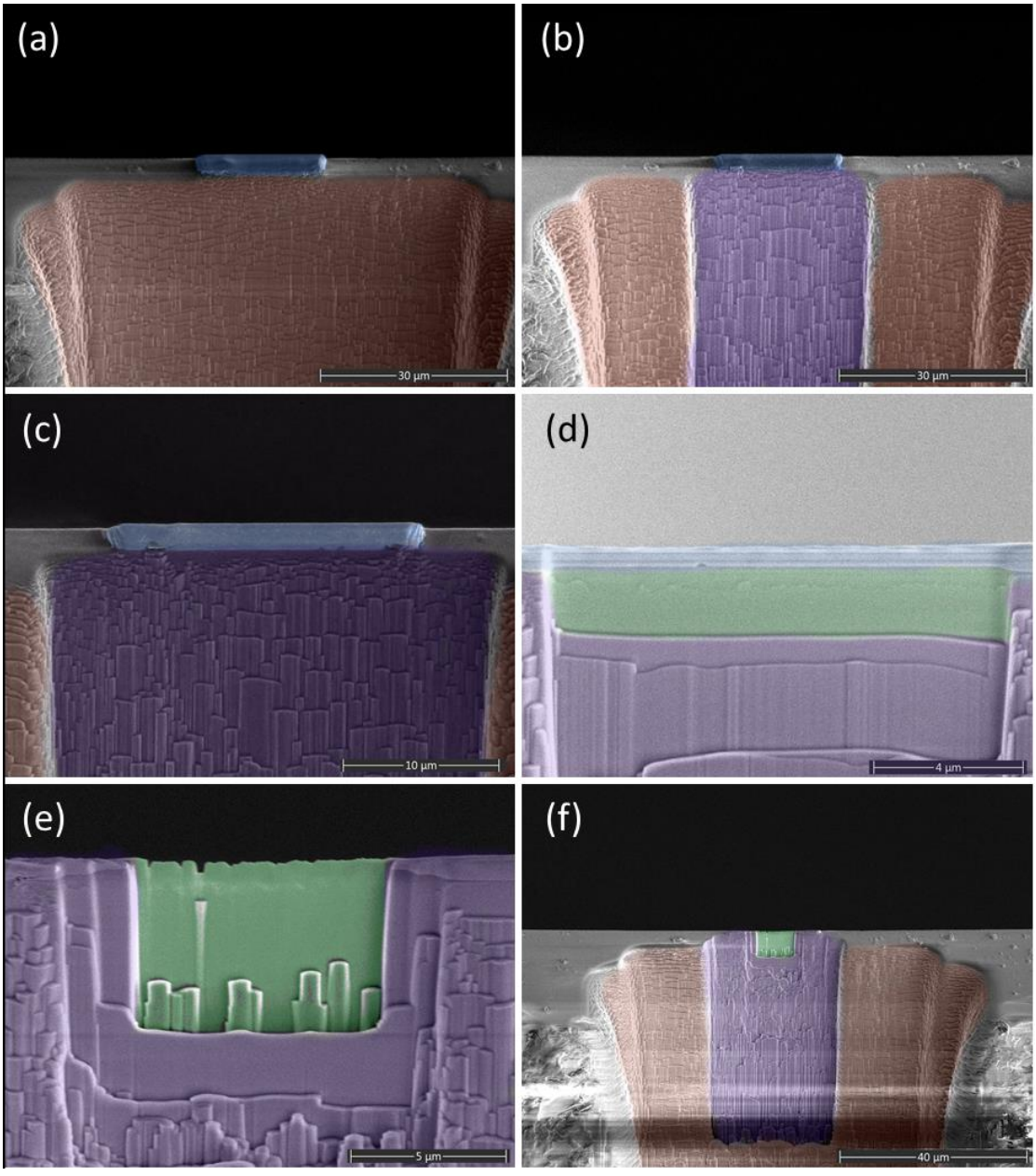

Figure 6.12 - Stages of FIB Sample thinning, red - Initial raster mill area, blue - deposited Pt, purple - cleaning cross section mill area, green - electron transparent area.

The FIB sample thinning process can be split into a number of stages shown in Figure 6.12. The first of these stages is a rough, high energy raster mill shown in red is Figure 6.12. Using the FEI Helios Xe Plasma FIB beam currents up-to 1.2 μA can be used, allowing removal of a 100 x 100 x 50 μm^3 volume of substrate in as little as 5 minutes. After this initial mill, a platinum bar is deposited to protect the top surface of the sample from delamination in subsequent milling operations. This Pt bar is shown in blue in figure 6.12 (a-d). From this point, cleaning cross section mills of decreasing power (50 nA to 1 nA) are used to thin the sample to electron transparency. During this process the deposited platinum is gradually removed as can be seen from comparison of Figures 6.12(c-e). Figure 6.12(f) shows the completed FIB thinning process with the $\sim$ 8 x 5 μm^2 electron transparent area shown in green.

Transmission Electron Microscopy (TEM)

Transmission electron microscopy (TEM) is a powerful research tool that can provide information about both the structural and chemical properties of a sample at an atomic scale. In this work, the microscopy has been carried out using a JEOL JEM-2011 TEM. This microscope uses a lanthanum hexaboride (LaB_6) thermionic filament and an acceleration potential of up to 200 keV. Once accelerated into the electron column, the beam is focussed to a $\sim$2 μm coherent beam and its intensity controlled by a number of lenses and apertures before interaction with the sample inside the objective lens. This lens focuses the transmitted, scattered electrons to form an intermediate image. This image is then further focussed and magnified by the intermediate lenses and apertures allowing for either a projection of an image or diffraction pattern. This is shown schematically in Figure 6.13.

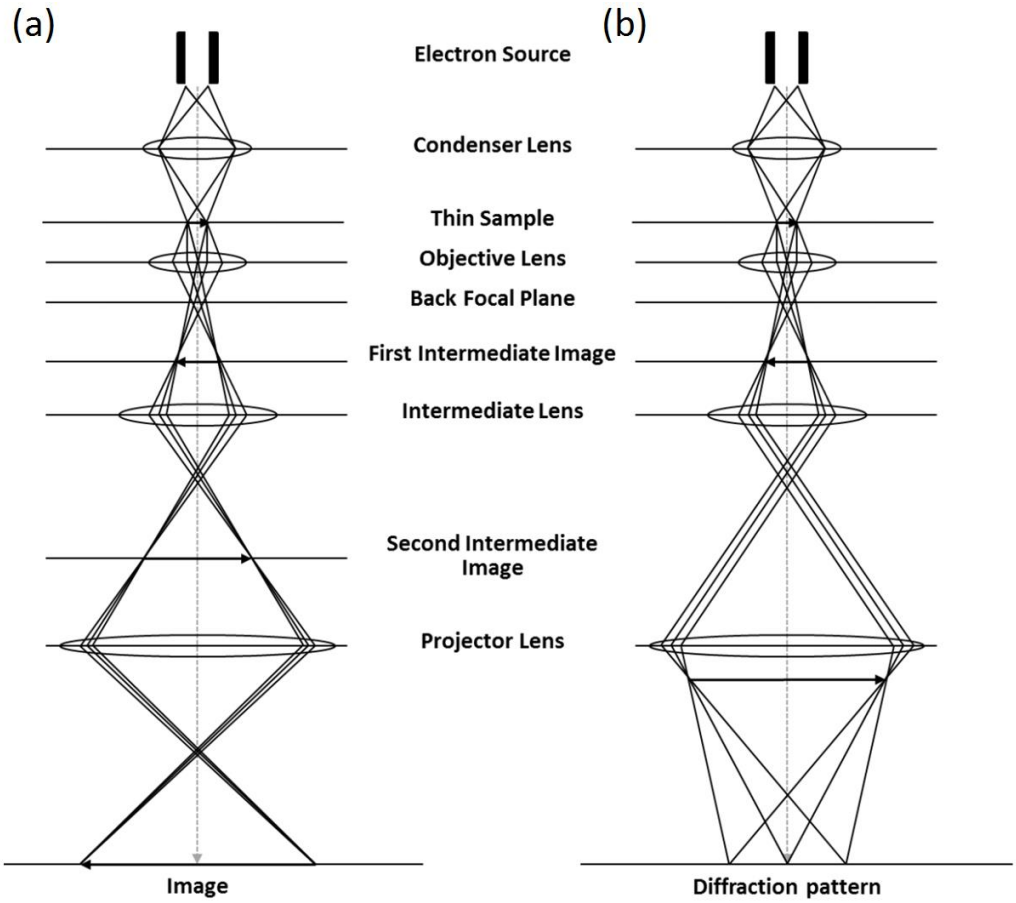

Figure 6.13 - Ray diagram for a typical TEM configuration for the formation of (a) bright field images and (b) diffraction patterns [197].

In TEM there are two major sources of contrast; mass-thickness and diffraction. The mass-thickness contrast is caused by low angle (< 0.5˚) scattering from interaction with the atomic nuclei dependent on Z-number and the thickness of the film. Diffraction contrast will only appear in crystalline materials where diffraction from lattice planes causes constructive and destructive interference. This allows for grain boundaries to be determined, as the diffraction contrast of each grain will depend upon its relative orientation.

Measurement of Size Distribution

After TEM images have been obtained, the grain diameters must be measured. For efficiency, grains are assumed to have a constant diameter and to be epitaxial (i.e. cylindrical grains). The grain diameters are measured manually using a Zeiss particle size analyser, with measurements recorded using a NI DAQ interface and LabView. To minimise the effect of any errors in the measurement, a minimum of 500 grains were measured for each sample.

6.3 Magnetic Characterisation

Thin film magnetic materials are typically characterised in terms of their saturation magnetisation (M_S), coercivity (H_C) and remanent magnetisation (M_R) all of which can be calculated from the measurement of a hysteresis loop. These parameters can be explored as a function of time, temperature or field angle relative to the easy axis of the sample.

When considering antiferromagnetic materials, there is no net moment from the sample making them difficult to characterise. Instead, it is common to grow a ferromagnetic material in contact with an antiferromagnetic material, in order to investigate its properties. Exchange coupling between the two layers allows information about the antiferromagnetic layer to be inferred from the behaviour of the neighbouring ferromagnetic layer. Using this technique, it is possible to measure the exchange bias (H_{EX}), thermal stability, coercivity enhancement and in conjunction with grain size analysis, the magnetocrystalline anisotropy (K) of the antiferromagnetic layer [73].

In this work, two types of magnetometer are used. Firstly the vibrating sample magnetometer (VSM), an instrument based on the measurement of induced voltage in pairs of coils due to the magnetic flux from a vibrating sample. Secondly, the alternating gradient force magnetometer (AGFM), which uses an alternating gradient field to produce a moment dependent displacement of the sample, measured using a piezo electric bimorph. These two systems are discussed in more detail in the following sections.

6.3.1 Vibrating Sample Magnetometer

The Vibrating Sample Magnetometer was first described by Foner in 1959 [198] and is now the one of the most common and versatile types of magnetometer available. The VSM uses Faraday's law of induction to detect a voltage related to the rate of change of magnetic flux from the sample as shown in equation 6.6.

$$V_i = -N_c \frac{d\phi_f}{dt} \tag{6.6}$$

where V_i is the induced voltage, ϕ_f is the magnetic flux from the sample and N_c is the number of turns in the coils. To produce a time-varying flux, the sample is vibrated between the pickup coils using a piezoelectric element or linear actuator. The total magnetic flux from

the sample is given by the sum of the applied magnetic field, H and the magnetisation, M of the sample as shown in equation 6.7.

$$\phi_f = (H + M) \cdot A_c \tag{6.7}$$

where A_c is the area of the detection coils. By combining equations 6.6 and 6.7 the voltage induced in the coils can be expressed as:

$$\int V_i \cdot dt = -N_c A_c \cdot M \tag{6.8}$$

where only the magnetisation contributes to the induced voltage as the external field is invariant with time. Figure 6.12 shows a schematic diagram of a VSM.

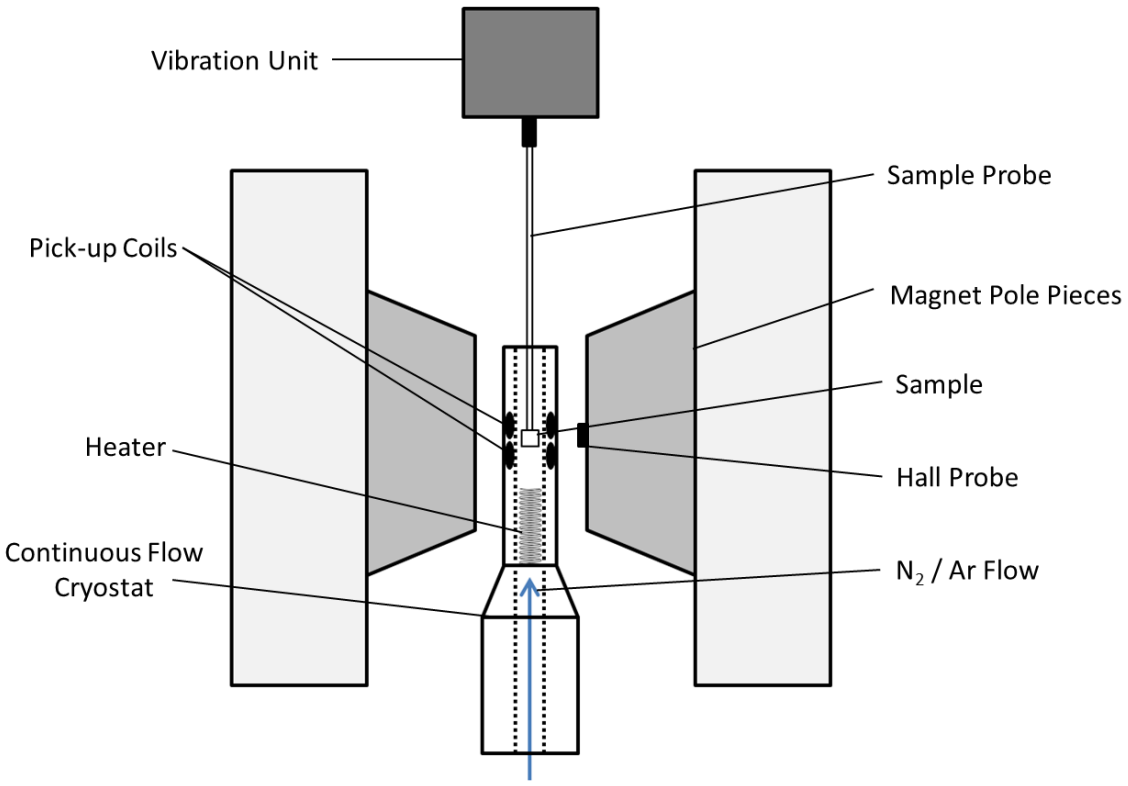

Figure 6.14 - Schematic Diagram of a VSM.

As shown in Figure 6.14 a continuous flow cryostat can be used in conjunction with the VSM allowing for temperature-dependent measurements to be conducted. Additionally, VSMs can be configured with vector coils and rotating stages as well as additional hardware for

measurement of magnetic torque and magnetoresistance effects. For these reasons, the VSM is considered the most versatile magnetometer available.

Microsense Model 10 VSM

The majority of magnetic measurements in this work were made using a Microsense Model 10 VSM. This VSM is equipped with Mallinson vector pick-up coils, 360˚ field control, an open, continuous-flow cryostat and resistive electromagnet with maximum field > 2 T.

The VSM uses a Stamford Research SR830 lock-in amplifier with a reference frequency of 75Hz, for each of the vector coil pairs. This allows a noise base of 5 μemu without any averaging and 0.5 μemu with 100 averages to be achieved at a measurement time from 30 minutes to 1 hour, depending on hysteresis loop parameters [199]. The Microsense system is unique when compared to other commercial systems, as when changing the field angle, it rotates the magnet assembly rather than the sample. This means the sample position remains fixed relative to the sense coils while rotating. The advantage of this geometry, is that the search coil sensitivity remains uniform over the full rotation range. Additionally, this is useful during calibration, as both the X and Y coils can be calibrated independently by setting the field angle to 45˚/-45˚.

The magnet is water-cooled and mounted on a rotational stage with 360˚ of travel and accuracy of 0.1˚. Using the standard pole pieces and a gap of 60 mm, a maximum field of 2.2 T is achievable using the 15 kW power supply. The pole pieces can be changed to give maximum field in excess of 3 T but with insufficient space to use the cryostat.

As the sample must be vibrated, use of a closed cryostat can reduce the sensitivity of the system due to transmission of vibration from the sample to cryostat material through vacuum seals. To prevent this, an open bath continuous flow cryostat is used. Gaseous N_2/Ar is pumped through a Dewar of liquid nitrogen before being fed into the bottom of the cryostat and heater as shown in Figure 6.14. The temperature of this gas flow is controlled using a PID feedback system. Using this approach, a temperature range of 100 K to 800 K is achievable. Under normal operation, N_2 is used as the cryogen; at temperatures above 575 K, Ar is used to prevent damage to the sample due to its higher stability.

Calibration

As the VSM is a comparative rather than a direct measurement technique, to ensure accurate measurements regular calibration of both H and M must be carried out. Calibration of the applied field is conducted using two reference points. First a zero Gauss chamber to establish a zero point and then secondly a reference permanent magnet, measured using a secondary standard Lakeshore model 425 Gaussmeter with certified trace-back to NIST. The VSM's Gauss probe is removed from the electromagnet and then adjusted accordingly to give correct readings at both calibration points.

To calibrate the moment, a nickel sphere is commonly used. However when measuring thin film materials this is not desirable for a number of reasons. Primarily the saturation moment measured from a nickel sphere will typically be 3-4 orders of magnitude larger than that of a thin film sample, additionally, it only provides a single point of calibration.

For thin film measurements, a more suitable calibration material is palladium (Pd) foil. It is a Pauli paramagnet, so has a well-defined linear magnetic susceptibility of $5.26 \times 10^{-6}\ \mathrm{cm^3 g^{-1}}$ [200, 201] and can be cut to the same size and shape as the measured sample allowing shape effects to be considered. Additionally, it has a good chemical stability, better than that of Nickel, thus allowing repeated use and cleaning of the calibration sample without any change in the moment. The mass of the Pd calibration sample is measured using a Mettler UMT2 microbalance to a precision of 1 μg allowing calculation of the moment of the sample.

The Pd calibration sample is inserted into the VSM and the calibration field is swept over a range similar to the measurement. The gradient of the resulting M/H line is then adjusted to match the value calculated using the sample's mass and susceptibility.

6.3.2 Alternating Gradient Force Magnetometer

The AGFM was first described by Zijlstra in 1970 [202] and developed further by Flanders in 1988 through the use of piezo-electric sensor materials [203]. It has two main advantages over the VSM: sensitivity over 2 orders of magnitude higher and up to 50 times shorter measurement acquisition times. The AGFM works by suspending the sample in both a continuous and AC magnetic field and measuring the force of the sample due to the gradient field. This displacement is measured by mounting the sample to a piezo-electric bimorph, which converts the stress exerted on it by the nanometre scale deflection of the sample to an

electric signal. Figure 6.15 shows a diagram of the AGFM probe head assembly used for detection of these deflections. The force is transmitted from the sample to the bimorph using thin quartz rods. The force F_M exerted on the sample by the gradient field is given by:

$$F_M = m_s \times \left(\frac{dH}{dx}\right) \tag{6.9}$$

where m_s is the moment of the sample and dH/dx is the magnetic field gradient measured in the x direction.

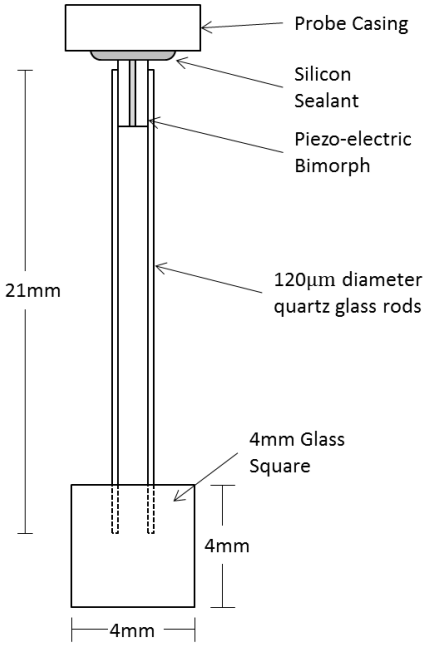

Figure 6.15 - Schematic diagram of AGFM Probe for in-plane measurement.

The use of an alternating gradient field allows the use of a lock-in amplifier and subsequently allows the system to be tuned to the resonant frequency of the probe and sample. This is necessary every time the sample is changed or remounted, as any mass change of the sample and mounting grease will result in a change in the resonant frequency. This approach allows a noise base of 10 nemu to be achieved, even at averaging times below 100 ms [204, 205]. Figure 6.16 shows a schematic diagram of the Princeton Measurements Corporation AGFM used in this work.

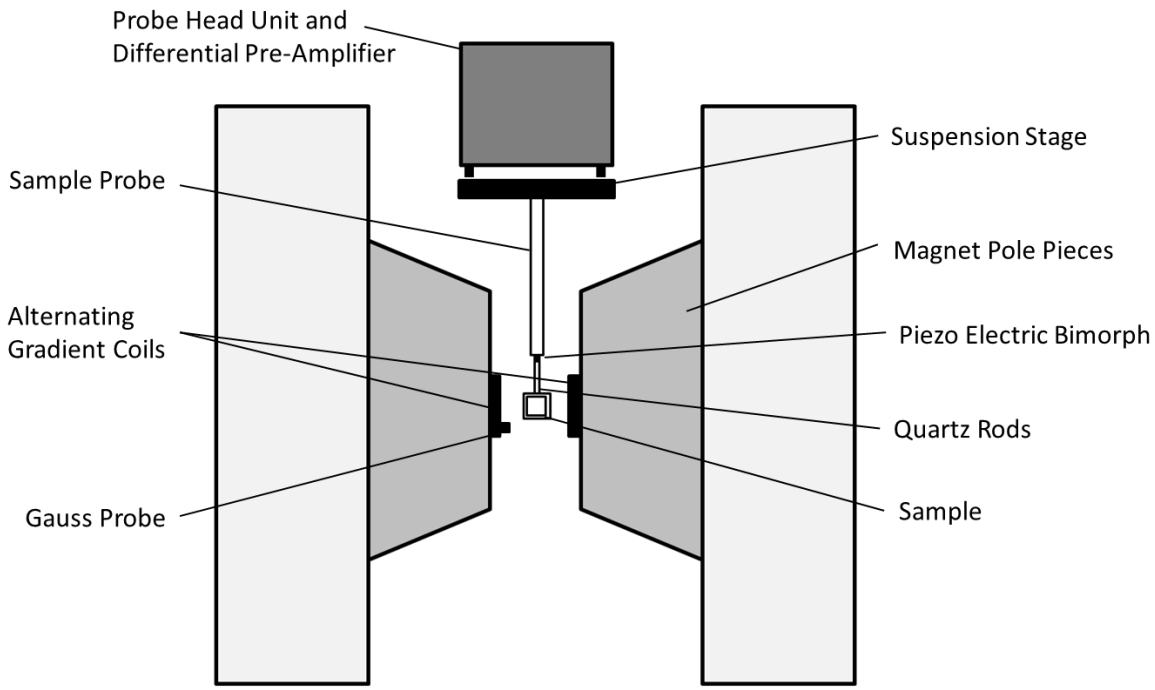

Figure 6.16 - Schematic diagram of AGFM system with in-plane sample probe.

This system uses resistive water-cooled electromagnets with a peak field of 2.2 T and is calibrated using the same method as described in section 6.3.1. Despite clear advantages in the sensitivity and shorter acquisition time achievable, the AGFM it is not as versatile as the VSM. This is due to two main factors. Firstly, the system is extremely sensitive to variation in resonant frequency; meaning factors such as temperature change can cause a large drift and difference in sensitivity. Secondly, due the mechanical nature of the system, the use of any gas flow or pumping equipment near the sample will result in additional noise in the measurement. For these reasons, when doing any measurement with temperature control, the VSM was the preferred method of characterisation.

Chapter 7: Experimental Results

The following work presents the growth and characterisation of materials with the potential to provide a viable alternative to IrMn as a thin film antiferromagnetic material for use in spintronic device applications.

7.1 Heusler alloys

Heusler alloys were chosen as a candidate group of materials for the HARFIR project because of both theoretical predictions and preliminary experimental work suggesting that they might provide a suitable alternative to IrMn. The reasons for the choice of Heusler alloys as a candidate material group are explained in detail in chapter 4. Almost all Heusler alloys crystallise in a cubic structure and hence the magnetocrystalline anisotropy is expected to be low. This is likely to cause a decrease in both the observed thermal stability and exchange bias obtained using these materials. Hence, techniques such as variation of stoichiometry and introduction of lattice strain, using seed layers or lattice matched substrates, are considered.

In this work, the two Heusler Alloys investigated were Ni_2MnAl and Ru_2MnGe with other alloys researched by partner institutions in the HARFIR project. Ideally, the growth of any new antiferromagnetic materials should comply with existing industrial standards for device fabrication. These standards include limits on both annealing times and temperatures, to maintain production line efficiency and to prevent damage to neighbouring device layers due to chemical decomposition or intermixing. The crystallisation and growth of these materials are characterised by XRD crystallography. Electrical and magnetic measurements are subsequently used to assess the suitability of the materials for commercial applications.

7.1.1 Ni_2MnAl

Ni_2MnAl is unusual in that it is predicted to exist in paramagnetic, antiferromagnetic and ferromagnetic phases dependent on the extent of its crystallisation [148]. The desired antiferromagnetic phase is the partially ordered B2 crystal phase. This phase has been shown to be stable in a single crystal thin film, deposited using molecular beam epitaxially and has a Néel temperature of 300 K [147]. Work prior to this project (unpublished HARFIR report) from

within the research group at York showed that growth of polycrystalline Ni_2MnAl on an amorphous Ta seed layer using the HiTUS system promoted crystallisation of the Heusler alloy compared to growth on Si (100) substrates directly. Growth on the 10 nm Ta seed layer should therefore allow crystallisation of Ni_2MnAl, using post growth annealing at temperatures which do not damage the thin film structure.

In addition to polycrystalline samples prepared using HiTUS, epitaxial Ni_2MnAl films were prepared using magnetron sputtering at Tohoku University on MgO substrates with growth temperatures between 573 and 873 K. Although this method of growth is unlikely be adopted commercially, the higher crystallinity of the deposited films allowed for determination of the Néel temperature of the material.

Polycrystalline Ni_2MnAl

Polycrystalline Ni_2MnAl films were prepared using the HiTUS deposition system. Initially Si (100) substrates with dimensions of 16×16 mm^2 and 5×5 mm^2 were used for X-ray and magnetic measurements respectively. Samples were deposited using a powder pressed Ni_2MnAl target at an Ar process pressure of 2.50×10^{-3} mbar and a bias voltage of 900 V. The thickness of the Ni_2MnAl layer was fixed at 50 nm to provide adequate signal for XRD measurements. In addition to an amorphous Ta seed layer, a 2.5 nm Ta cap was used to prevent oxidation of the material surface.

The films were post annealed using a vacuum furnace capable of temperatures up to 1000 K with a base pressure below 1×10^{-6} mbar achieved using a diaphragm roughing pump and turbo-molecular main pump.

As shown in Figure 7.1 no clear peak is visible in XRD spectra for the Ni_2MnAl until after annealing. In subsequent measurements, after annealing for 1 hr at 673 and 773 K clear (220) peaks are visible for Ni_2MnAl corresponding to out of plane lattice constants of 5.88 Å and 5.85 Å respectively. From Figure 7.1 alone it is not possible to determine the phase in which the Ni_2MnAl has crystallised, as the A2, B2 and $L2_1$ structures have almost identical lattice parameters. To confirm the presence of the antiferromagnetic B2 phase either electrical measurements on the existing films or magnetic measurements of similar films grown with a neighbouring ferromagnetic layer can be used.

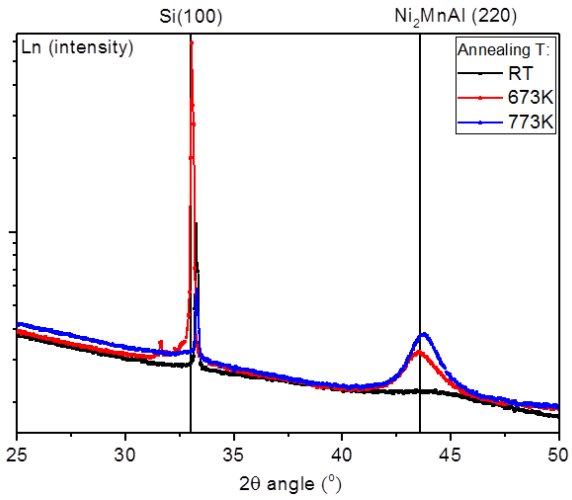

Figure 7.1 - XRD θ/2θ scan showing the effect of 1 hr post annealing on crystallisation of 50 nm thick Ni_2MnAl films on a Ta seed layer.

Early measurements of the electrical resistivity for Ni_2MnAl films showed a large change in the resistivity, however this was shown to be a consequence of growth on a semiconducting substrate. To avoid this, electrical measurements were instead performed on samples grown on electrically-insulating quartz substrates. Figure 7.2 (a) shows an example of the temperature variation of the resistivity for polycrystalline Ni_2MnAl obtained using the magnetoresistance apparatus described in Chapter 5.

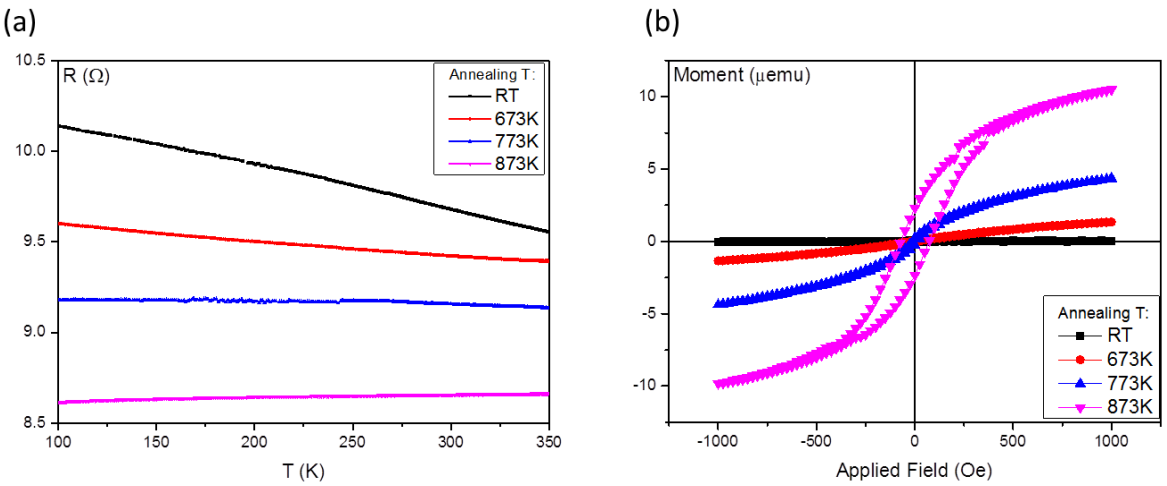

Figure 7.2 - (a) Temperature dependent electrical resistivity (b) Room temperature magnetisation curves, of 50 nm Ni_2MnAl films as grown and then post annealed at temperatures up to 873 K for 1 hr on quartz substrates.

It is immediately obvious that despite their 50 nm thickness, the Ni_2MnAl films have a high intrinsic resistance. Although this decreases with annealing temperature, all films have a resistance between 8.65 Ω and 9.67 Ω at room temperature. This value of resistance is probably due to a large amount of scattering at grain boundaries. This is confirmed by Scherrer broadening, which gives an estimate of the mean crystallite size in the films as 4.9 nm.

Due to the high resistance of the films, it is impossible to measure any change in the resistance due to the variation of magnetic scattering at the Néel temperature as the resistance is dominated by grain boundary scattering. Figure 7.2(b) shows the room temperature magnetisation curves for the samples. As expected, the un-annealed sample shows no magnetic hysteresis, however all annealed samples show a degree of ferromagnetic order which increases with annealing temperature. This is direct evidence of formation of the fully ordered, ferromagnetic $L2_1$ phase of Ni_2MnAl. The increase of saturation magnetisation observed at higher annealing temperatures will be due to a large proportion of the film becoming fully ordered.

As electrical measurements were unable to provide any confirmation of the antiferromagnetic B2 phase, a number of exchange bias devices were grown with a 3 nm CoFe ferromagnetic layer. Figure 7.3 shows the resulting hysteresis loops after field cooling to 100 K.

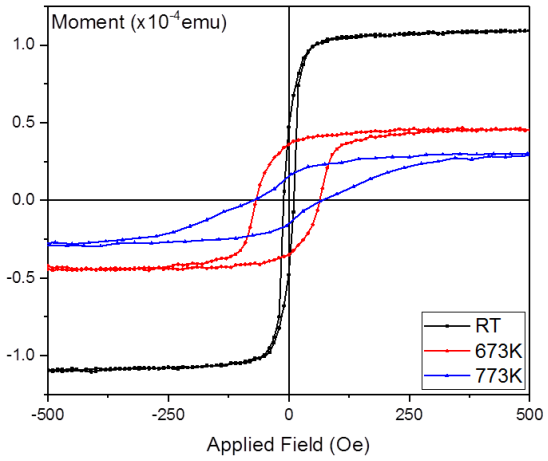

Figure 7.3 - Magnetic hysteresis loops at 100 K for Ni_2MnAl (30 nm) / CoFe (3 nm) / Ta (2.5 nm) films as grown and then after field annealing/cooling for 1.5 hrs at 673 & 773 K in an applied field of 20 kOe.

Although no exchange bias is observed, both annealed samples show a considerable increase in coercivity compared to the un-annealed sample. This may be due to exchange coupling of the CoFe layer to the Ni_2MnAl layer. However, as a large decrease (72%) in saturation magnetisation is observed, this could also be due to pinning caused by increased roughness and intermixing at the CoFe interface.

Epitaxial Ni_2MnAl

During the course of the HARFIR project epitaxial Ni_2MnAl films were prepared at Tohoku University using UHV magnetron sputtering in a system with a base pressure below 5×10^{-9} mbar. Ni_2MnAl films were co-sputtered from three separate targets onto heated MgO (100) substrates cleaned using argon ion milling. The deposition temperature was varied from 573 to 873 K. The film composition was found to be $Ni_{52}Mn_{25}Al_{23}$ (at. %) using inductively-coupled plasma optical emission spectroscopy [206]. As part of the collaboration, a set of 100 nm thick Ni_2MnAl films, capped with 3 nm Al, were sent to York for further analysis. Figure 7.4 shows the XRD data obtained for these samples.

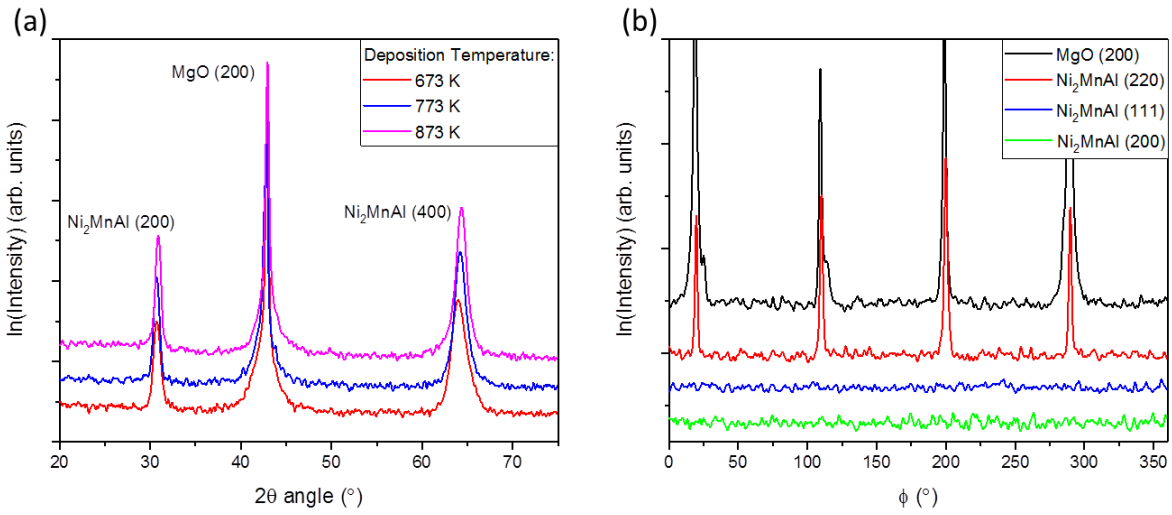

Figure 7.4 - (a) XRD $\theta/2\theta$ spectra for 100 nm Ni_2MnAl films on MgO single crystal substrates at deposition temperatures 673, 773 and 873 K. (b) XRD ϕ scan fixed on MgO (200) and Ni_2MnAl (200), (220), (111) in-plane diffraction peaks for the sample grown at 773 K.

Figure 7.4 (a) shows the presence of sharp (200) superlattice and (400) diffraction peaks for the epitaxially co-sputtered Ni_2MnAl suggesting the films are well crystallised. Similar to the polycrystalline samples, a contraction of the lattice constant is observed for the films deposited or annealed at higher temperatures. For these samples the out of plane lattice

constant decreased from (5.82 ± 0.01) Å to (5.78 ± 0.01) Å. The 4 clear peaks in the Ni_2MnAl (220) ϕ scan shown in Figure 7.4 (b) indicate that the epitaxially grown Ni_2MnAl films have extremely strong in plane texture and have crystallised in a B2 or $L2_1$ structure, with the Ni_2MnAl lattice lying on the MgO (100) substrate at an angle of 45°. The absence of the Ni_2MnAl (200) and (111) $L2_1$ diffraction peaks in the ϕ scan, confirm that no $L2_1$ structure is present.

Electrical measurement of the samples revealed that the epitaxial films had a resistance of the order 1 mΩ at room temperature; approximately 10^4 times lower than the polycrystalline samples. Figure 7.5(a) shows the temperature-dependent resistivity for the epitaxial samples.

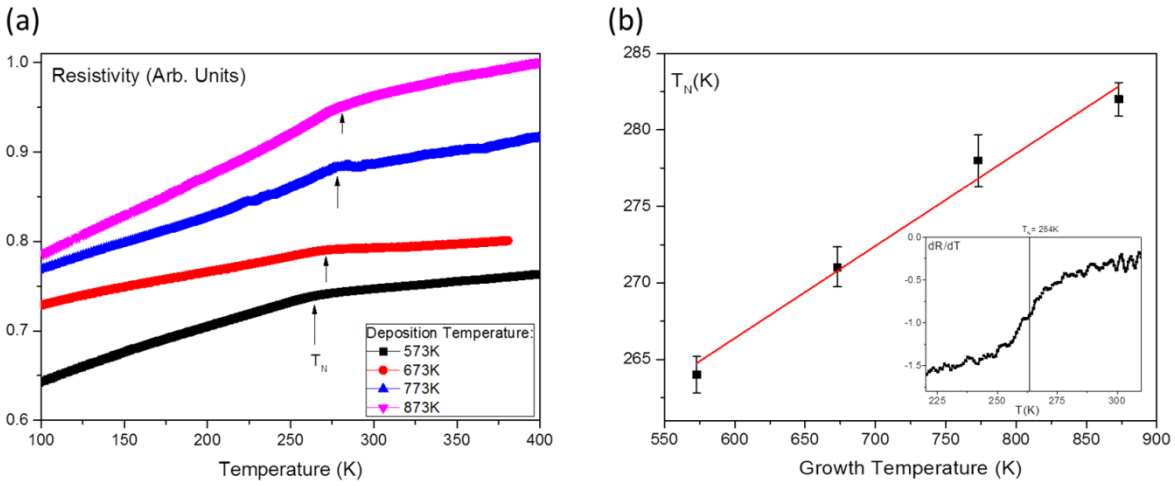

Figure 7.5 - (a) Temperature-dependent electrical resistivity of epitaxial Ni_2MnAl films. (b) Néel temperature dependence on the deposition temperature of Epitaxial Ni_2MnAl films. Inset figure shows an example of the dR/dT plot used for determination of T_N.

All samples display a change in gradient associated with a phase change from an antiferromagnetic to paramagnetic state. To determine the accurate location of the gradient change, derivative plots were used as shown in the inset graph in Figure 7.5(b). A clear linear relationship is observed in Figure 7.5(b) between the deposition temperature and the Néel temperature. This is probably due to higher deposition temperature allowing the formation of larger grains, leading to greater stability of the antiferromagnetic phase. As expected, the Néel temperatures obtained are lower than those found in the literature for bulk single crystal Ni_2MnAl ($T_N = 313$ K) [147, 148].

Researchers at Tohoku University also performed low temperature magnetic measurements on similar Ni_2MnAl films with a 3 nm Fe ferromagnetic layer using superconducting quantum

interference device (SQUID) magnetometry. The results of these measurements are shown below in Figures 7.6(a) & (b).

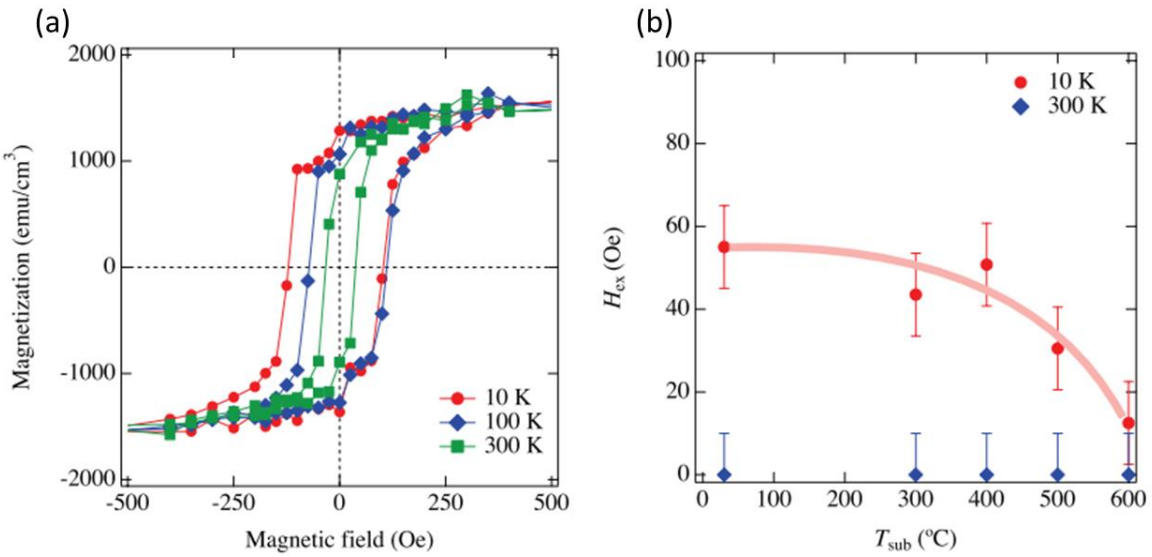

Figure 7.6 - (a) Hysteresis loops for the Ni_2MnAl (100 nm) / Fe (3 nm) bilayers deposited at 773 K, measured at 10, 100 & 300 K [206]. (b) Deposition temperature-dependence of the exchange bias in Ni_2MnAl (100 nm) / Fe (3 nm) bilayers [206].

Despite clear evidence of the antiferromagnetic B2 phase and Néel temperatures between 264 & 282 K, no exchange bias was observed for any samples at temperatures above 80 K using the Microsense model 10 VSM. This suggests that the maximum blocking temperature of the material is much lower than 100 K. Interestingly, Figure 7.6(b) shows that the highest exchange bias (55 Oe) was reported for the Ni_2MnAl film deposited at room temperature, rather than samples deposited at high temperature. This result can be possibly explained by a number of mechanisms caused by the variation of deposition temperature. As the film was grown on a MgO (100) substrate with a plane diagonal lattice spacing of 5.96 Å, increased deposition temperatures will reduce the internal strain present and therefore decrease the magnetocrystalline anisotropy, however this is unlikely to be the case in 100nm thick films. Instead it is more likely that a variation in the grain size or crystallinity resulted in the low thermal stability of the exchange bias observed. This anisotropy of Heusler alloys is discussed in greater detail in section 7.1.3.

7.1.2 Ru_2MnGe

Ru_2MnGe is the second candidate Heusler alloy investigated in this project. Similar to Ni_2MnAl, it is a Mn-based alloy, however it is predicted to be antiferromagnetic in its fully-ordered $L2_1$ phase. Additionally, calculations of the ground state energies for Ru_2MnGe indicate that it should be most stable in a (111) sheet antiferromagnetic structure [144].

Growth Optimisation

All growth of Ru_2MnGe was done using the BESTEC 2", 4 source magnetron sputtering system in Bielefeld University. Samples were co-sputtered from 3 separate targets onto heated single crystal MgO substrates similar to the epitaxial Ni_2MnAl described previously. All samples were deposited at a process pressure of 2.0×10^{-3} mbar with a Ru_2MnGe deposition rate of 1.32 Å/s calibrated using XRR. Due to the system having a maximum of 4 magnetron sources, all samples were capped with 2 nm Ru allowing bilayer samples with a ferromagnetic CoFe layer to be prepared. Initial stoichiometry was controlled by calculation of sputter power, then refined incrementally using XRF. Figure 7.7 shows the XRF spectrum for the final composition achieved.

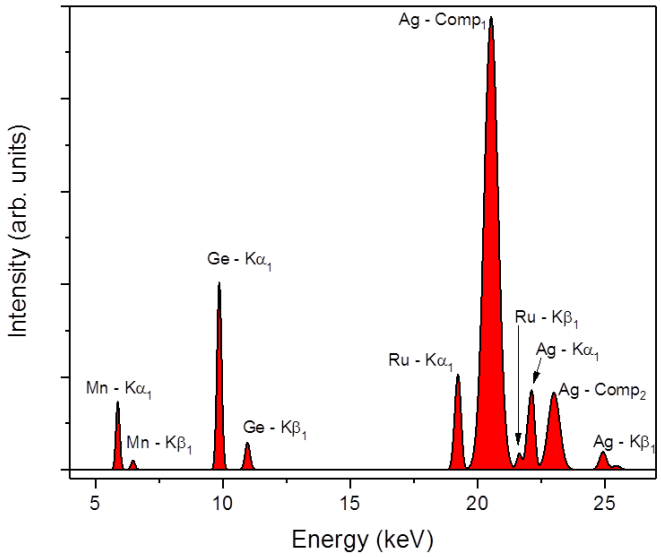

Figure 7.7 - XRF spectrum for Ru_2MnGe film on glass substrate after background subtraction. Kα, Kβ and Compton (inelastic) peaks labelled for all elements.

Using the spectrum shown in Figure 7.7, the final stoichiometry was calculated to be Ru = (50.0 ± 0.5), Mn = (25.1 ± 0.4) and Ge = (24.9 ± 0.2) by atomic percentage. Ag peaks in the

spectrum are due to the use of an Ag anode X-ray source. After refinement of the stoichiometry, samples were grown on MgO substrates at deposition temperatures between 723 & 823 K.

Structural Characterisation

After growth, 100 nm thick Ru_2MnGe films were measured using XRD to characterise the film quality. Figure 7.8 shows a selection of the XRD data obtained.

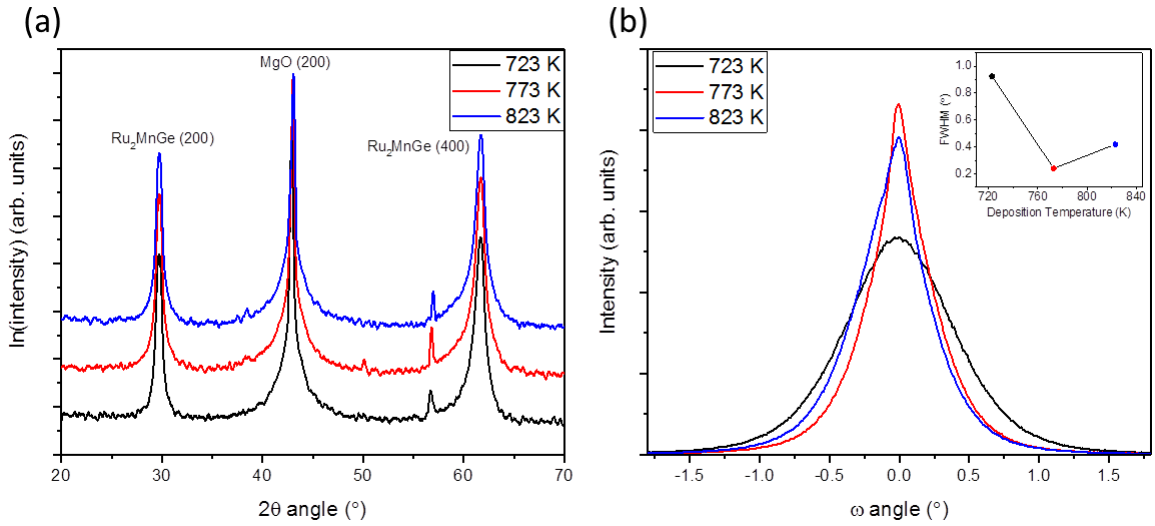

Figure 7.8 – (a) $\theta/2\theta$ spectra for 100 nm Ru_2MnGe films on MgO (100) substrates grown at deposition temperature between 723 & 823 K. (b) Ru_2MnGe (200) rocking curves showing the FWHM of peaks obtained using split pseudo-Voigt fitting (inset).

From inspection of Figure 7.8 (a) it is clear that all samples are well crystallised and show no change in lattice constant for the different deposition temperatures. The mean lattice constant was calculated to be (6.004 ± 0.004) Å. When compared to the (110) direction lattice constant in MgO, this gives a lattice mismatch between film and substrate of only 0.79% (0.04 Å) meaning it is not possible to distinguish between MgO (200) and Ru_2MnGe (220) peaks in in-plane XRD scans using the best X-ray optics available.

Figure 7.8 (b) shows measurement of the rocking curves for the Ru_2MnGe (200) diffraction peaks. The widths of all peaks confirm the polycrystalline nature of the samples, with the sample deposited at 773 K showing the greatest degree of texture with a rocking curve full width half maximum (FWHM) of 0.27°.

Measurement of the Blocking Temperature

Ru_2MnGe samples with the structure MgO (Sub) / Ru_2MnGe (20 nm) / CoFe (2.3 nm) / Ru (2 nm) grown at a deposition temperature of 773 K were used for magnetic measurements. Samples were set in an applied field of 20 kOe at T_{set} = 500 K for 90 minutes, after which they were field cooled to T_{NA} = 100 K. During the measurement the samples were incrementally activated in steps of 10 K at temperatures 100 K < T_{act} < 140 K with all measurements carried out at 100 K.

Figure 7.9(a) shows examples of the hysteresis loops obtained during the measurement. On inspection of the hysteresis loop taken at 100 K (black) it is clear from the high squareness that the reversal is dominated by a nucleation and rapid domain motion driven process. There is some evidence of pinning or domain rotation during the last 20% of the reversal, which becomes more evident in measurements after activation at higher temperatures. The hysteresis loop measured at 100 K also shows the maximum exchange bias obtained (81 Oe) for the Ru_2MnGe samples.

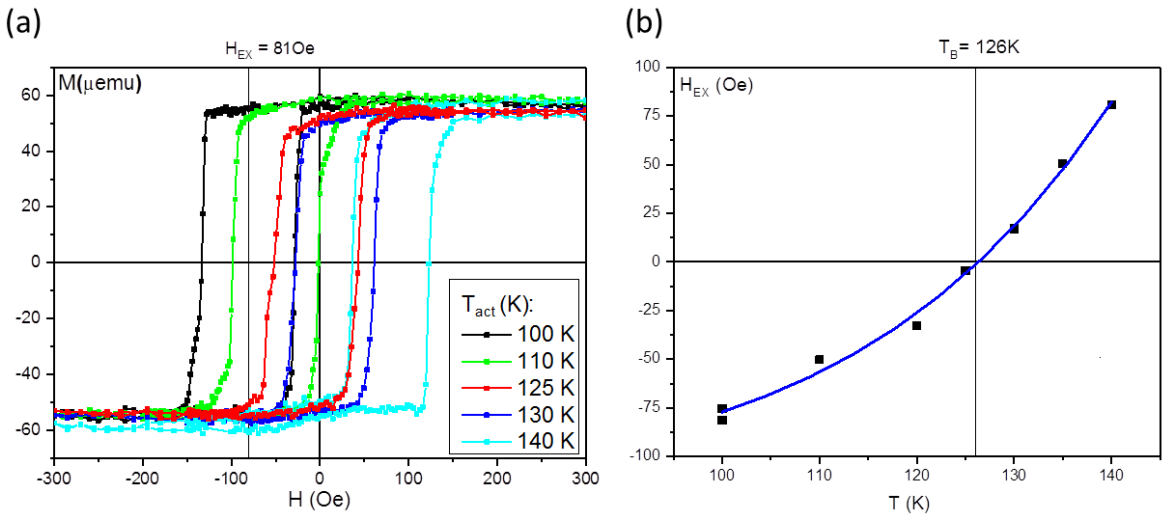

Figure 7.9 - Magnetic measurements for Ru_2MnGe (30 nm) / CoFe (2.5 nm) samples showing (a) Hysteresis loops at 100 K after thermal activation for 30 minutes at temperatures T_{act} = 110 K to 140 K. (b) Exchange bias as a function of activation temperature.

Figure 7.9(b) shows the exchange bias as a function of activation temperature. The point where half the grain volume distribution has been reversed meaning no exchange bias is observed is the median blocking temperature T_B = (126 ± 3) K. It is clear that the lowest temperatures available (100 K) are not sufficient to saturate the exchange bias due to thermal

instability. If the derivative of the blocking curve were to be fitted this would result in a very broad distribution of blocking temperature. For this reason it is not possible to calculate an accurate estimate of the magnetocrystalline anisotropy in the Ru_2MnGe film.

7.1.3 Magnetocrystalline Anisotropy of Antiferromagnets

There is little existing literature regarding the anisotropy of antiferromagnetic materials. Most studies focus on neutron scattering though due to the inherent difficulty of measurement due to no net moment being produced from the structure. Therefore, the majority of work is based on theoretical predictions, as discussed in section 2.4.

The York model allows direct measurement of the effective antiferromagnetic anisotropy as long as the antiferromagnetic film is exchange coupled to a neighbouring ferromagnetic layer. Despite this the principles by which antiferromagnetic materials give rise to their anisotropy are not well understood. By considering the behaviour of anisotropy in ferromagnetic materials, it is possible to suggest that similar effects can give rise to the anisotropic behaviour of antiferromagnets.

It is well known that systems with cubic structure inherently have low anisotropy, however this anisotropy is strongly dependent on the crystallographic direction of the magnetisation as shown below in Figure 7.10.

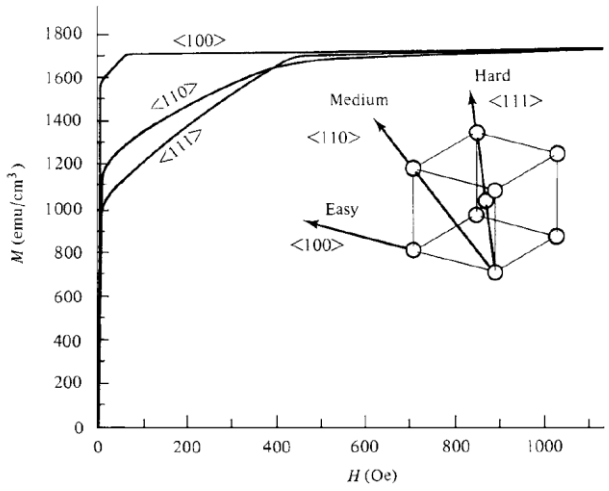

Figure 7.10 – Magnetisation curves for Fe along its three principal crystallographic directions [4].

Figure 7.10 shows that the (110) and (111) crystal directions in BCC iron have significantly higher saturation fields and therefore effective anisotropy than those oriented in the (100)

direction. This can be understood by consideration of the crystal anisotropy energy E_K; the energy equal to the work done to turn the magnetisation direction away from the easy axis. Akulov showed in 1929, that E_K can be expressed in terms of a series expansion of the direction cosines of the magnetisation relative to the crystal axes [207].

$$E = K_0 + K_1(\alpha_1^2\alpha_2^2 + \alpha_2^2\alpha_3^2 + \alpha_3^2\alpha_1^2) + K_2(\alpha_1^2\alpha_2^2\alpha_3^2) \ldots \quad (7.1)$$

where K_0, K_1, K_2 are anisotropy constants for the material at a particular temperature and $\alpha_1, \alpha_2, \alpha_3$ are the cosines of the angles the magnetisation makes with the crystal axes. These anisotropy constants can be determined experimentally, for example for Iron, $K_1 = 4.8 \times 10^5$ ergs/cm^3. Similarly, for nickel, which due to its FCC structure has an easy axis in the (111) direction, the anisotropy can be calculated as $K_1 = -0.5 \times 10^5$ ergs/cm^3. Although generally cubic materials have low anisotropy, there are a limited number of exceptions to this rule, the principal being cobalt ferrite ($CoO{\cdot}Fe_2O_3$) which has an exceptional anisotropy for a cubic structure of $K_1 = 2.0 \times 10^6$ ergs/cm^3. This is due to its complex inverse spinel structure where the Co^{2+}, Fe^{2+} and Fe^{3+} occupy octahedral and tetrahedral lattice sites, therefore increasing the anisotropy.

Generally, most high anisotropy ferromagnets have inherently anisotropic structures such as hexagonal close packed (HCP) or tetragonal. Well known examples of HCP ferromagnets are Co ($K_1 = 4.5 \times 10^6$ ergs/cm^3), and $BaO{\cdot}6(Fe_2O_3)$ ($K_1 = 3.3 \times 10^6$ ergs/cm^3). In the case of barium ferrite, this has led to its applications in magnetic stripe cards, as coercivities in excess of 5 kOe are achievable. The inclusion of Pt into HCP Co can further increase the anisotropy as high as $K_1 = 4.1 \times 10^7$ ergs/cm^3 [208].

Modern hard drive recording media uses $Co_{75}Cr_{15}Pt_{10}$. The further inclusion of Cr, improves the corrosion resistance and lowers the saturation magnetisation considerably. This allows the recorded information density to be increased substantially, due the reduction in the demagnetisation field. In granular thin films, coercivities in excess of 5 kOe are obtainable [209, 210]. Superlattice structures such as Co/Pt multilayers can generate even higher coercivities than those in alloys, due to interfacial two-ion effects, but are hence not relevant to this work. The best known example of a ferromagnet with tetragonal structure is $Nd_{31}Fe_{67}B_{1.2}Dy_{0.8}$, this material is widely used in applications which require bulk permanent magnetism and has replaced AlNiCo and ferrite magnets in many applications such as in electrical generators.

As discussed in section 3.4 spin valve sensors have led to increased interest in antiferromagnetic materials. In particular, the thermal stability of materials used in exchange bias devices. The York Model has shown that the loop shift is controlled by the thermal stability which is in turn controlled by a quasi-Stoner-Wohlfarth type reversal dependent on the product of the magnetocrystalline anisotropy and the grain volume as shown in equation 2.6 reproduced below.

$$\Delta E = K_{AF} V \left(1 - \frac{H^*}{H_K^*}\right)^2 \tag{2.6}$$

The first material used in hard drive read heads was NiO as discussed in chapter 2. However, due to its low anisotropy, the read head had to frequently be re-set during use, due to thermal relaxation. Subsequently FeMn ($K_{AF} = 1.35 \times 10^5$ ergs/cm^3 [211]) came into common usage, although due to its low corrosion resistance and limited anisotropy, due to its cubic structure, despite planar (111) antiferromagnetic alignment, was later replaced by alloys such as PtMn and IrMn.

Both of these alloys have unique features that enhance the magnetocrystalline anisotropy. PtMn is deposited in a cubic FCC phase, however, with the use of high temperature annealing it is possible to crystallise the fully ordered $L1_0$ face centred tetragonal (FCT) phase, increasing the anisotropy to ($K_{AF} = 1.9 \times 10^6$ ergs/cm^3 [212]). IrMn is cubic and has been shown to exhibit a (111) sheet antiferromagnetic structure in thin films, as shown in Figure 2.10(b) reproduced below, but it is believed that the high value of effective anisotropy ($K_{AF} = 2.7 \times 10^7$ egrs/cm^3 [108]) is due to the disparity between the sizes of the Ir and Mn atoms.

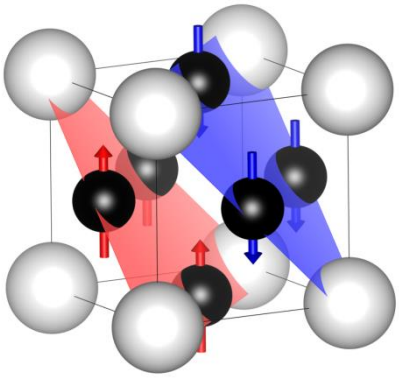

Figure 2.10 (b) - Schematic drawing of magnetic unit cell of ordered FCC alloy (111) sheet antiferromagnet with collinear spin structure.

Additionally, it is worth noting that although nominally the composition is $IrMn_3$, sputtered films usually have a composition closer to $IrMn_4$ as discussed previously in chapter 2.

All Heusler alloys grown in this work and in the collaborative HARFIR project had cubic structures and as a consequence, have had low thermal stabilities due to their limited anisotropy. In Ni_2MnAl the spin ordering is predicted to be along the (100) direction coupled inter-atomically as shown in Figure 7.12(a) [213]. From the previous discussion it is clear that the anisotropy will be analogous to that of Fe or Ni.

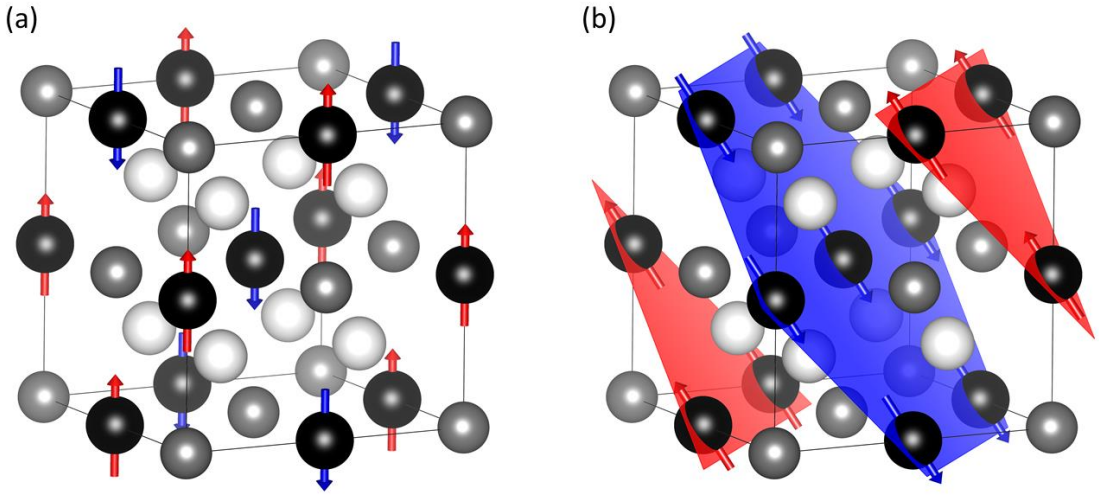

Figure 7.11 - Predicted antiferromagnetic spin structures for the full Heusler alloys with the composition X_2YZ, where atoms: X- white, Y-black, Z- grey (a) B2 Ni_2MnAl (black and grey sites interchangeable) (b) $L2_1$ Ru_2MnGe.

The spin ordering in Ru_2MnGe is predicted to be along the (111) planes with the moments oriented parallel to the plane and is therefore a sheet antiferromagnetic material [144]. This structure is similar to that of IrMn and as a result has a higher anisotropy manifested by a higher measured blocking temperature. However as the Néel temperature is only just above room temperature, Ru_2MnGe is not suitable for integration into device applications.

7.2 Manganese Nitride

For the reasons discussed in section 7.1.3, the focus of the project was moved away from cubic Heusler alloys due to their inherently low anisotropy. Based on a series of works produced by Meinert et al. [151] at Bielefeld university in 2015, MnN was chosen as an alternative prototype material due to its tetragonal structure and promising initial measurements. As collaborators in the HARFIR project, researchers at Bielefeld University sent a MnN film to York for evaluation of its thermal stability. Subsequently more MnN films were prepared, using both the HiTUS system in York and the BESTEC 2" magnetron system in Bielefeld during a laboratory exchange, to investigate effects of layer thickness, seed layers, doping and growth rate.

MnN films are prepared using reactive sputtering, there are many possible phases of the manganese nitride and growth of these phases is primarily controlled by nitrogen content. The desired antiferromagnetic equi-atomic θ–phase MnN crystallises in a FCT tetragonal variant of the NaCl structure with a bulk c/a ratio of 0.984 at room temperature [152]. This phase is the most nitrogen rich phase, meaning it can be obtained relatively easily by sputtering with a gas composition of 50:50 N_2:Ar by atomic percentage. As can be seen from Figure 4.4(b), θ–phase MnN is a sheet antiferromagnetic material with planes lying along the (100) direction [17] further details of the structure are discussed in chapter 4.

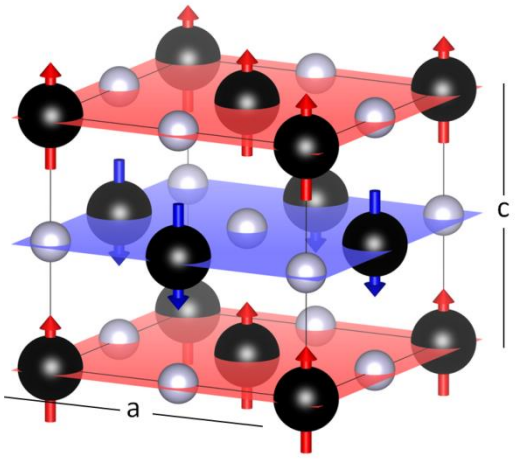

Figure 4.4 (b) - Spin structure of the unit cell of θ-phase MnN with dimensions a = 4.256 Å, and c = 4.189 Å [152].

7.2.1 Blocking Temperature of Prototype Samples

Initially, one MnN exchange bias sample was provided by Bielefeld University in order to assess the thermal stability of the compound. The layer structure of the sample is shown below in Figure 7.12. The sample was prepared using a 4" BESTEC UHV Magnetron deposition system similar to the 2" BESTEC system described in section 6.1.2. The main differences lie in the working distance between source and substrate, source size and number of magnetron sources present. The system base pressure was 5×10^{-9} mbar and process pressure was 2.3×10^{-3} mbar giving a typical deposition rate for MnN of 1 Å/s at a source power of 50 W.

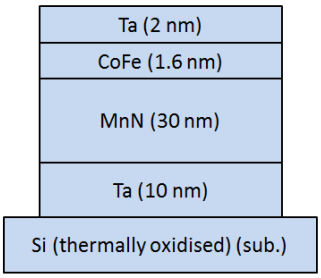

Figure 7.12 – MnN exchange bias sample structure.

After growth, the sample was field annealed in a vacuum furnace at 600 K for 15 minutes in a magnetic field of 6.5 kOe. XRD data from Bielefeld indicated that the out of plane lattice constant was larger than the in-plane constant giving a c/a tetragonal distortion of 1.04. The mean perpendicular crystallite size was calculated from Scherrer broadening of the MnN (200) and (400) peaks using the Williamson-Hall equation to be (14 ± 3) nm.

Figure 7.13(a) shows examples of the hysteresis loops taken during measurement of the blocking temperature. Prior to measurement, the sample was reset at 500 K for 90 minutes in line with the York Protocols. The maximum exchange bias observed at room temperature was 1208 Oe. This high value will be due in part to the low thickness of the CoFe ferromagnetic layer. From the shape of the hysteresis loop, it is clear that the reversal does not occur through a nucleation and rapid reversal process similar to the Heusler alloys previously investigated, but instead by a more gradual domain nucleation, rotation and propagation process. On careful inspection of the hysteresis loops with higher exchange bias, where the ferromagnetic CoFe layer is still near saturation at zero field, there is a step in the magnetisation at H = 0 Oe. The cause of this step is not known but is probably due to some

form of inhomogeneity at the interface between the CoFe and MnN layers causing a decrease in the strength of the exchange coupling between the layers.

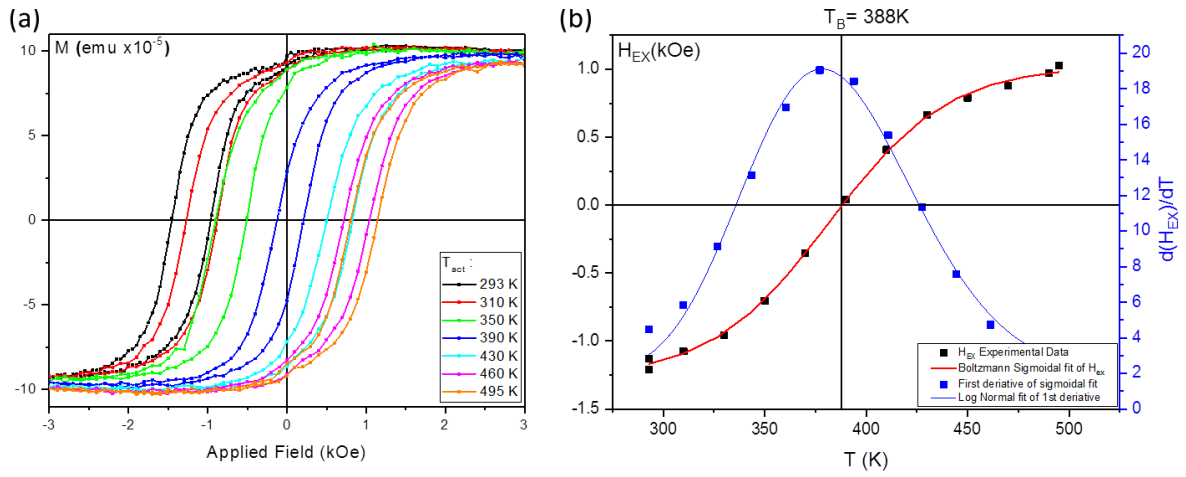

Figure 7.13 - Magnetic thermal stability data for MnN (30 nm) / CoFe (1.6 nm) sample: (a) hysteresis loops taken after setting in reverse field at temperatures T_{act} for 30 mins (b) Blocking temperature variation.

Again, using the York Model measurement protocols, it is possible to determine the blocking temperature as shown in Figure 7.13(b). Immediately it is clear that the MnN is almost fully thermally stable at room temperature. Conversely to the hysteresis loops, the blocking temperature measurement shows no evidence of reduced coupling or anisotropy between the layers. To investigate this further it would be necessary to make measurements at lower temperatures to find any non-uniformity in the blocking process.

The data obtained fit well to a classical Boltzmann sigmoid function, as found for other exchange bias systems. The mean value of the blocking temperature ($< T_B >$) was found to be (388 ± 3) K with a maximum of $T_B \cong 480$ K. The distribution of blocking temperatures can be found by taking the first derivative of the data and is shown in Figure 7.13(b). A log normal distribution was used to fit the resulting data. As the blocking temperature relates to the product $K_{AF}V$, the quality of the fit suggests the anisotropy constant must remain constant over the measurement, as the grain volume distribution will invariably fit the log normal distribution. Using the estimate of lateral grain size obtained from Scherrer broadening and the film thickness to calculate the mean grain volume, it is possible to calculate an estimate of the effective anisotropy constant of $K_{AF} = 7 \times 10^4$ ergs/cm^3. This lower value of anisotropy confirms why thick layers are necessary to achieve thermal stability at room temperature when compared to the anisotropy constant of IrMn ($K_{AF} = 2.7 \times 10^7$ ergs/cm^3 [108]).

7.2.2 Small Grain Films

After promising initial thermal stability measurements of the prototype MnN film prepared by researchers at Bielefeld University, a full study was undertaken. This study included the effects of variation of layer thickness, seed layers, lattice matched substrates and oblique angle sputtering. Sample growth was carried out using both the 2" BESTEC magnetron system and the novel HiTUS system. Structural characterisation was performed using X-ray diffraction and electron microscopy, magnetic characterisation was done using the Microsense model 10 VSM. Additional work was carried out by BSc project students under direct guidance of the author. The results of these studies are presented in the following sections. All data presented are for samples where t_{MnN} = 30 nm unless otherwise stated.

Sample Growth and Structural Characterisation

Samples were prepared using the BESTEC 2" magnetron sputter deposition system described in section 6.1.2. The typical deposition rate for MnN was 0.47 nm/s at a source power of 50 W and process pressure of 2.3 x 10^{-3} mbar. Sample structure was identical to that shown in Figure 7.12, except the MnN layer thickness was varied between 10 nm and 50 nm. Figure 7.14 shows the XRR spectrum obtained for the sample with t_{MnN} = 30 nm. Simulation and fitting of the reflectivity data yielded a MnN layer thickness of (29.4 ± 0.1) nm and a density of (6.17 ± 0.08) gcm^{-3}. When fitting, layer thicknesses are obtained from the Fourier transform of the XRR data before refining along with density and surface roughness values. The roughness values obtained were between 0.1 and 0.4 nm.

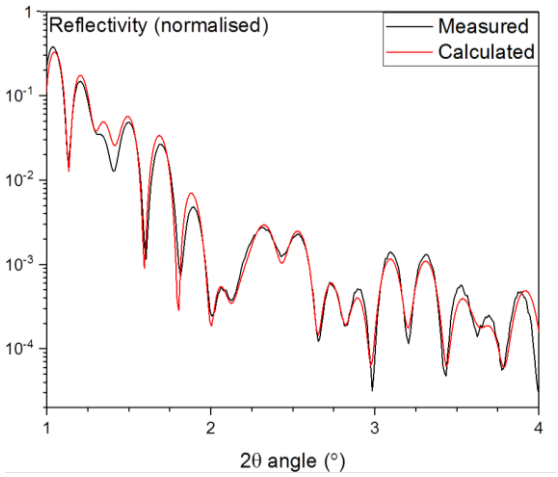

Figure 7.14 – Measured XRR data and calculated fit for 30 nm MnN prepared using magnetron sputtering.

The thickness obtained from XRR is consistent with the nominal thickness obtained from calibration of the crystal growth rate monitor. The density is higher than the value of 6.03 gcm^{-3} previously obtained using a stoichiometric composition and the lattice constants calculated by Suzuki et al. [152]. This higher value is however consistent with the work by Meinert et al. [151]. The XRD data obtained for the MnN prepared using magnetron sputtering is shown in Figure 7.15.

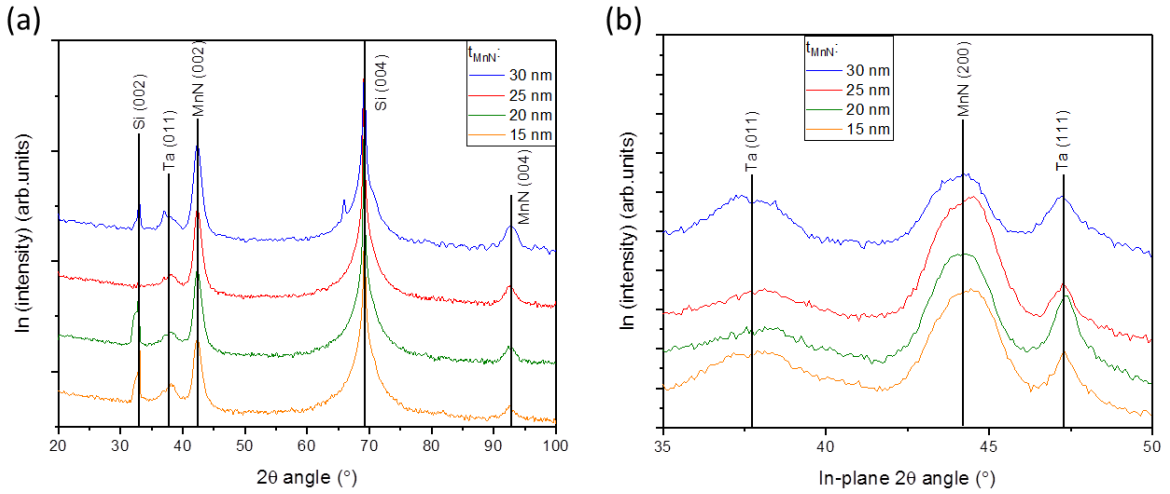

Figure 7.15 – (a) Out of plane and (b) In-plane, $\theta/2\theta$ XRD measurements of 15 – 30 nm MnN film stacks produced using magnetron sputtering.

From the data presented in Figures 7.15(a) & (b) the lattice parameters corresponding to the out of plane (002) and (004) and in-plane MnN (200) peaks were calculated. These data show that the MnN is oriented with its c axis out of plane with 2D random texture in plane. A summary of these data, together with the calculation of the tetragonal distortion is given is table 7.1. Additionally the Scherrer crystallite size was calculated from the MnN (002) peak for all samples. No significant variation in crystallite size was observed as a function of film thickness, with all samples having a crystallite size between 8.7 and 9.1 nm.

Table 7.1 – Summary of calculated lattice parameters and tetragonal distortion ratios for MnN prepared using magnetron sputtering:

Thickness (nm)	Out of plane (002) (Å)	Out of plane (004) (Å)	In-Plane (200) (Å)	Tetragonal Distortion
15	4.267	4.263	4.077	1.047
20	4.265	4.264	4.107	1.038
25	4.266	4.267	4.078	1.046
30	4.265	4.264	4.114	1.037
Mean	4.266 ± 0.001	4.265 ± 0.002	4.09 ± 0.02	1.042 ± 0.005

To investigate the effects of seed layers, doping and oblique angle sputtering, additional samples were prepared using the HiTUS system. Initially, samples were reactively sputtered from a powder pressed Mn target however, due to the high plasma power of the HiTUS system and the brittle nature of Mn, this resulted in cracking of the Mn target. To resolve this, a cast Mn target bonded to a copper backing plate was used for further growth. Using a 50:50 N_2:Ar (at. %) gas mixture and 900 V bias voltage resulted in a typical growth rate of 0.46 Å/s, almost identical to MnN prepared using the BESTEC 2" magnetron system. Figure 7.16 shows the X-ray structural characterisation for a 30 nm MnN prepared using the HiTUS system.

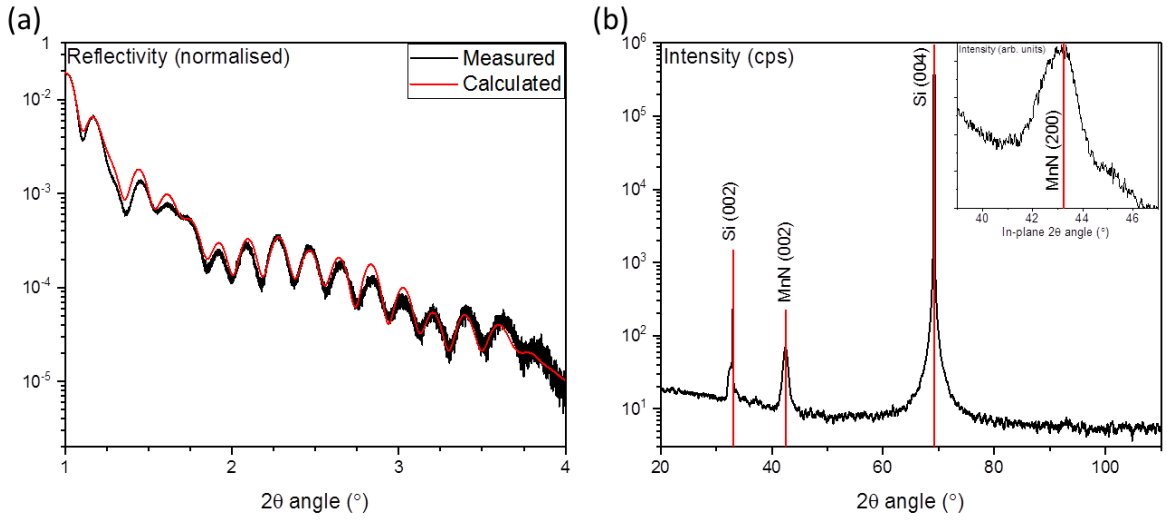

Figure 7.16 - (a) Measurement of film thickness and density using XRR. (b) XRD $\theta/2\theta$ scan for MnN (30 nm) / CoFe (3 nm) sample prepared using the HiTUS system. In-plane 2θ χ/ϕ scan of MnN (200) peak inset.

From the calculated data shown in Figure 7.16(a) a layer thickness of (30.5 ± 0.2) nm and a density of (6.2 ± 0.1) gcm^{-3} were obtained for the MnN layer. To reduce the magnitude of the oscillations in the calculated data to match the experimental data, layer roughness was set to between 1 and 3nm. Only the MnN (002) peak is visible in the θ/2θ measurement shown in Figure 7.16(b) indicating a lower level of crystallinity than that for samples prepared using magnetron sputtering. The inset figure in Figure 7.16(b) shows the in plane XRD spectrum. Due to the lower crystallinity of the samples prepared using HiTUS a 14 hour scan was used to obtain the in-plane diffraction data presented. Additionally the in-plane ϕ angle was set to avoid the Si (220) substrate diffraction peak. Using Bragg's law, the in and out of plane lattice constants were calculated to be (4.168 ± 0.004) Å and (4.247 ± 0.001) Å respectively, resulting in a tetragonal distortion ratio of (1.019 ± 0.001).

Grain Size Analysis

The distributions of lateral grain diameters were determined using TEM as described in section 6.2.4. Films grown using magnetron sputtering and the HiTUS system were measured. Figures 7.17 & 7.18(a) show examples of bright field TEM images of the film surface. As the samples have a constant thickness and homogeneous composition over the observed area, contrast in the bright field TEM images will be primarily due to diffraction. For this reason, grains orientated to meet the Bragg condition show sharp contrast (black in bright field image) meaning their boundaries can be easily determined. Figures 7.17(b) & 7.18 (b) show the grain diameter distribution obtained after measurement of at least 500 grains.

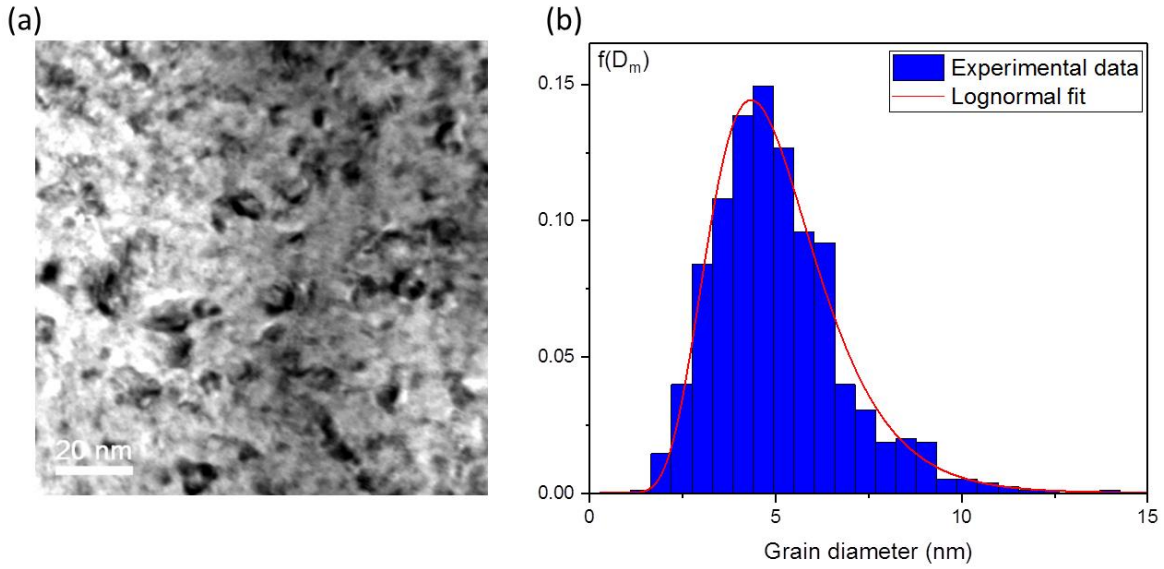

Figure 7.17 - Measurement of the grain size distribution for 30 nm MnN films prepared using magnetron sputtering (a) Typical TEM image used for size analysis, (b) Summary of grain diameter data obtained from measurement of 750 grains.

A log normal distribution function was fitted to the grain size distribution shown in Figure 7.17 (b), this fit yields a mean grain size of $D_m = (4.83 \pm 0.04)$ nm with a standard deviation of $\ln(D_m)$ of $\sigma_D = (0.328 \pm 0.007)$. Given no change in lattice constant, crystallinity or Scherrer crystallite size is seen in the XRD measurements as a function of layer thickness for films prepared using magnetron sputtering, the grain size is assumed to be constant between samples.

Figure 7.18 shows the determination of the lateral grain size distribution for a 30 nm MnN film grown using the HiTUS deposition system. Immediately it is obvious that the lateral grain

size is substantially larger. Interestingly, on careful inspection of Figure 7.19(a) the majority of grains appear to be segregated by a thin boundary area with bright contrast, this may be due to contamination from the HiTUS system. As the AF grains are not significantly exchange coupled together due to their absence of a net moment, this is not expected to affect magnetic measurements.

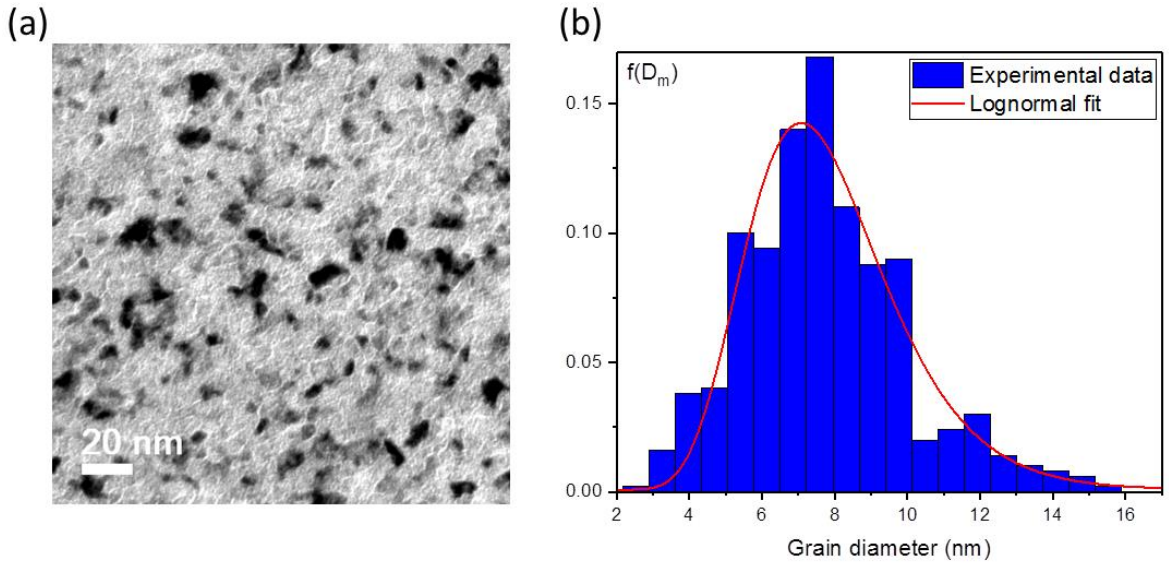

Figure 7.18 - Measurement of the grain size distribution for 30 nm MnN films prepared using the HiTUS equipment (a) Typical TEM image used for size analysis, (b) Summary of grain diameter data obtained from measurement of 500 grains.

Fitting a lognormal distribution to the data shown in Figure 7.18(b) gives a mean grain size of $D_m = (7.59 \pm 0.09)$ nm with a standard deviation in $\ln(D_m)$ of $\sigma_D = (0.26 \pm 0.01)$ nm. When comparing the results obtained for the grain size in MnN films prepared using different techniques, it is important to compare grain volume rather than diameter, as it is the volume that will control the thermal stability. Assuming columnar growth and using the layer thicknesses derived from XRR data, the mean grain volumes were calculated to be (549 ± 6) nm^3 in the films prepared using magnetron sputtering and (1380 ± 10) nm^3 in the films prepared using the HiTUS system.

Setting Process

As the initial state of the antiferromagnet is unknown, the first requirement is to set the antiferromagnet in a reproducible manner. Ideally, the antiferromagnetic layer is set by field cooling from above its Néel temperature, however due to the high Néel temperature of MnN

($T_N = 655$ K [214]) this is not possible as these temperatures would result in interfacial mixing and nitrogen desorption. Instead, the antiferromagnet is set by a thermal activation process at $T_{set} < T_N$ for a setting time of t_{set}. To determine the best value for T_{set}, it is possible to measure the dependence of the exchange bias on the setting temperature. Initially a setting time of $t_{set} = 90$ mins was used, as suggested by the York Protocols [58]. To eliminate effects of unwanted thermal activation from the measurement, the sample is first cooled to a temperature where no thermal activation occurs (T_{NA}); this temperature is determined by trial and error for each sample as described in chapter 3.

Figure 7.19 shows the measurements used to determine T_{set} for a sample prepared using magnetron sputtering. From inspection of the example hysteresis loops shown in Figure 7.19(a), it is clear that as the setting temperature increases, there is a change in the reversal of the ferromagnetic layer. Before the antiferromagnetic layer is set, the reversal is gradual, indicative of reversal via a domain rotation or domain wall movement process. This is due to strong exchange coupling between the ferromagnetic and randomly orientated antiferromagnetic grains.

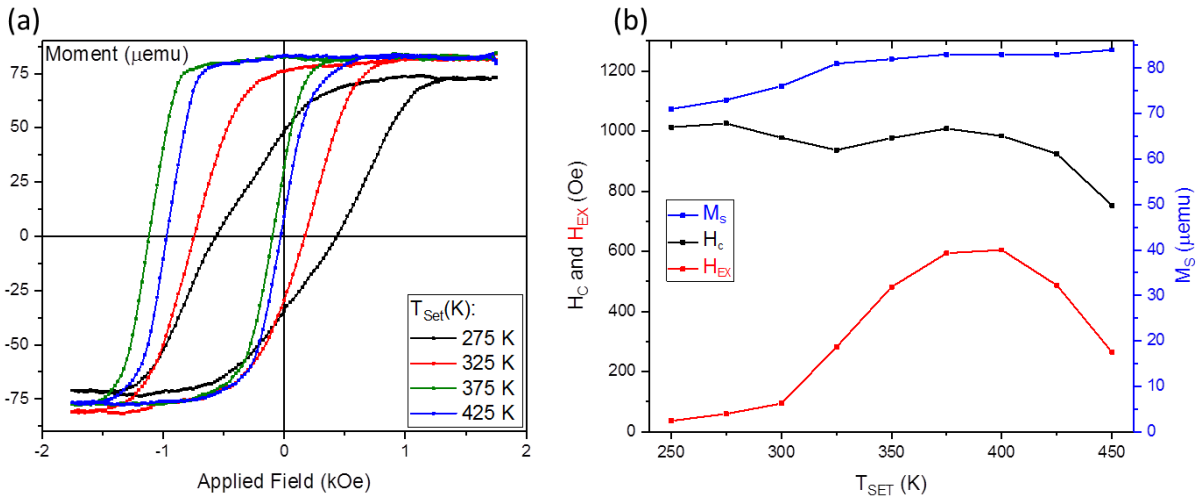

Figure 7.19 - Setting temperature dependence MnN film prepared using Magnetron sputtering, all measurements at 250 K (a) Examples of hysteresis loops obtained (b) summary of hysteresis loop parameters as a function of setting temperature.

As the MnN becomes set in-plane, the magnitude of this effect is decreased, subsequent hysteresis loops still display a gradual reversal which is indicative of a wide distribution of domain wall pinning strengths in the MnN. This re-orientation of the strongly exchange-

coupled grains also explains the increase in saturation magnetisation observed between the hysteresis loops for the unset, and set samples.

Figure 7.19 (b) shows an initial increase in exchange bias with increasing setting temperatures. This is due to a larger proportion of the grain size distribution becoming thermally activated, allowing a larger proportion of the antiferromagnetic grains to be set. At setting temperatures above 400 K, a sharp decrease in exchange bias is observed and no change in saturation magnetisation is observed. This suggests that there is no damage to the ferromagnetic CoFe layer, this is probably due to desorption of nitrogen from the MnN layer [215]. For this reason, a setting temperature of $T_{set} = 380$ K was used for all further measurements of films prepared using magnetron sputtering.

Figure 7.20 shows a similar measurement for a MnN exchange bias sample prepared using HiTUS. At setting temperatures from 300 K to 500 K an increase in coercivity is observed along with an increase in exchange bias (147 Oe at T_{set} = 300 K to 197 Oe at T_{set} = 500 K).

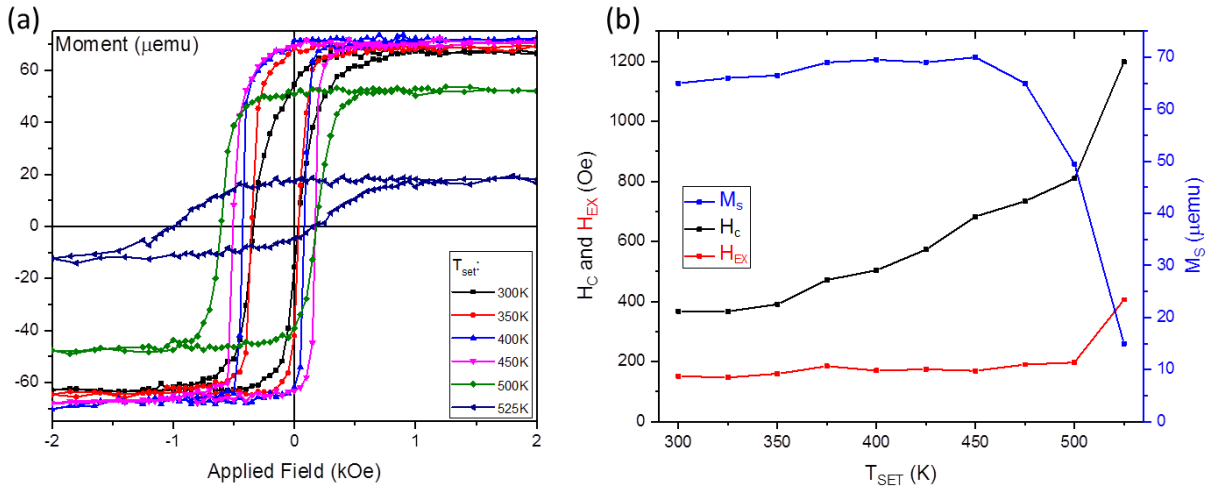

Figure 7.20 - Setting temperature-dependence of 30 nm MnN / 3 nm CoFe film prepared using the HiTUS deposition system, all measurements at 300 K (a) Examples of hysteresis loops obtained, (b) Summary of hysteresis loop parameters as a function of setting temperature.

As no peak in exchange bias was observed, measurements were taken at incrementally higher temperatures until a sharp decrease in saturation magnetisation was observed. This decrease in M_s implies damage to the ferromagnetic CoFe has occurred, probably through intermixing

at the interface. The increase in coercivity is further evidence of damage as more pinning sites will be available.

Considering that damage has occurred to the ferromagnetic layer, the sharp increase in exchange bias observed for T_{set} = 550 K may be entirely due to a reduction in thickness of the ferromagnet rather than any change in the MnN. As 450 K is the highest setting temperature where no decrease in saturation magnetisation is observed, $T_{set} = 450$ K was used for all further measurements of HiTUS prepared MnN films.

To determine the necessary setting time, an un-set MnN sample was set incrementally measuring the exchange bias multiple times during the setting process. Figure 7.21(a) shows the value of exchange bias as a function of setting time for films deposited using magnetron sputtering. Each measurement was performed at 250 K after removal of any training effect. Over 99% of the maximum exchange bias is observed after $t_{set} = 110$ mins, hence this value of t_{set} was used when measuring the blocking temperatures of MnN samples.

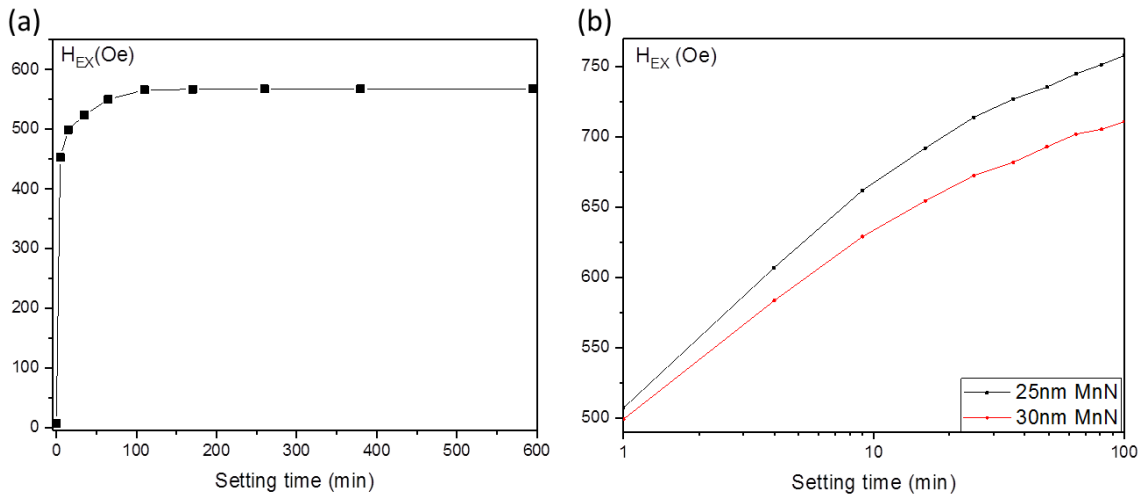

Figure 7.21 - (a) Setting time dependence of the exchange bias up to 10 hours with $T_{set} = 380$ K. (b) $\ln(t)$ dependence of the exchange bias in 25 and 30nm thick MnN films prepared using magnetron sputtering.

From further inspection of Figure 7.21 it is evident that no decrease in exchange bias is observed even after setting in an open cryostat/oven at 380 K for 10 hours. This confirms that setting at 380 K does not thermally damage the film as shown for higher temperatures in Figure 7.19.

Figure 7.21 (b) shows exchange bias as a function of $\ln(t)$, for both $t_{MnN} = 25$ and 30 nm. As previously discussed in section 3.3.2 non-linearity in these data suggest a narrow distribution of energy barriers, this corresponds well with the grain size distribution determined from TEM data shown in Figure 7.18(b).

Similar setting time dependence experiments were carried out for the samples prepared using the HiTUS system. However 100% of the maximum exchange bias was observed for setting times under 1 minute, suggesting the effective anisotropy of the material must be much lower.

Measurement of the Blocking Temperatures

Using the values of T_{set} and t_{set} determined previously, the blocking temperatures in MnN were measured via the York Protocol as described in chapter 3. Figure 7.22 shows the data obtained for the samples produced using magnetron sputtering.

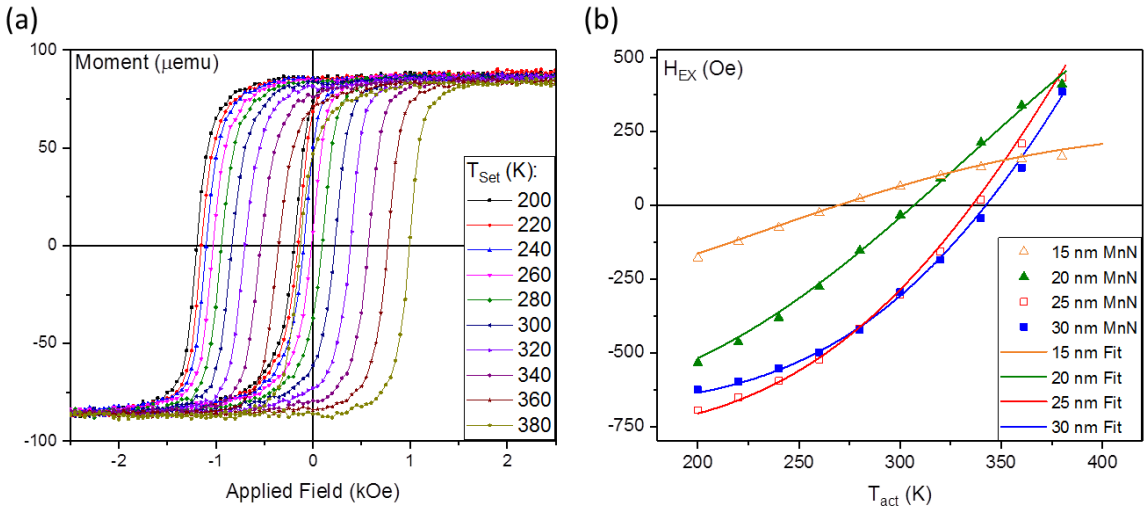

Figure 7.22 - Blocking data for samples produced using magnetron sputtering: (a) Hysteresis loops measured at 200 K after setting at incrementally higher temperatures for 100 minutes. (b) Summary of blocking data (points) with calculated fits (solid lines).

Comparing the blocking data shown in Figure 7.22(b) for the different MnN layer thicknesses, it is clear that as layer thickness increases the median blocking temperatures ($< T_B > = 269$ to 343 K). The experimental data were fitted using the following equation [58, 74]:

$$H_{EX}(T_{act}) \propto \int_{\Delta E(T_{act})}^{\Delta E(T_{set})} f(\Delta E)d(\Delta E) - \int_{\Delta E(T_{NA})}^{\Delta E(T_{act})} f(\Delta E)d(\Delta E) \qquad (7.2)$$

where ΔE is the energy barrier to reversal for a given AF grain, $f(\Delta E)$ is the distribution of energy barriers in the antiferromagnet and ΔE (T_{act}) is the critical energy barrier that determines the fraction of the antiferromagnet that will reverse at the temperature T_{act} after thermally activating for 30 minutes. ΔE (T_{set}) represents the energy barrier of the grains that cannot be set at T_{set} due to their anisotropy energy being too large and ΔE (T_{NA}) refers to the fraction that remains thermally unstable, if any, at the temperature of measurement T_{NA}. The fitting parameters used in Figure 7.22 were as follows: $f_0 = 2.1$ x 10^6 s^{-1} [99], $T_{NA} = 200$ K, $T_N = 655$ K, $T_{set} = 380$ K, $D_m = 4.83$ nm, $\sigma_D = 0.328$, $t_{act} =$ 1800 s and $t_{set} = 6600$ s. The anisotropy constant of the material (K_{AF}) was the only floating parameter.

Although a constant value of anisotropy might be expected as all samples studied had a high MnN layer thickness compared to what is commonly used in devices, the value had to be varied as a function of layer thickness to fit the data accurately. The variation of the anisotropy constant as a function of layer thickness is shown in Figure 7.23.

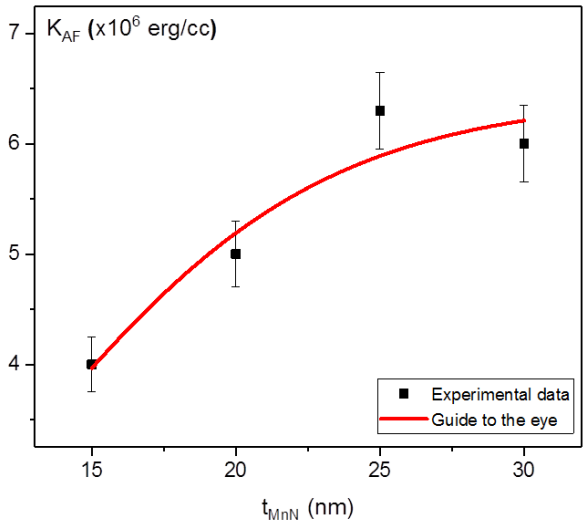

Figure 7.23 - Anisotropy constant in samples prepared using magnetron sputtering as a function of antiferromagnet layer thickness.

Values in the range 4.0 to 6.6 x 10^6 ergs/cm^3 were used for the antiferromagnetic anisotropy constant for layer thicknesses between 15 and 30 nm respectively. This variation in the anisotropy constant is probably due to structural or stoichiometric variations between the samples caused either by annealing or growth conditions given the complex phase diagram of MnN.

A similar measurement was undertaken for the larger grain MnN sample produced using the HiTUS system, the results are shown in Figure 7.24.

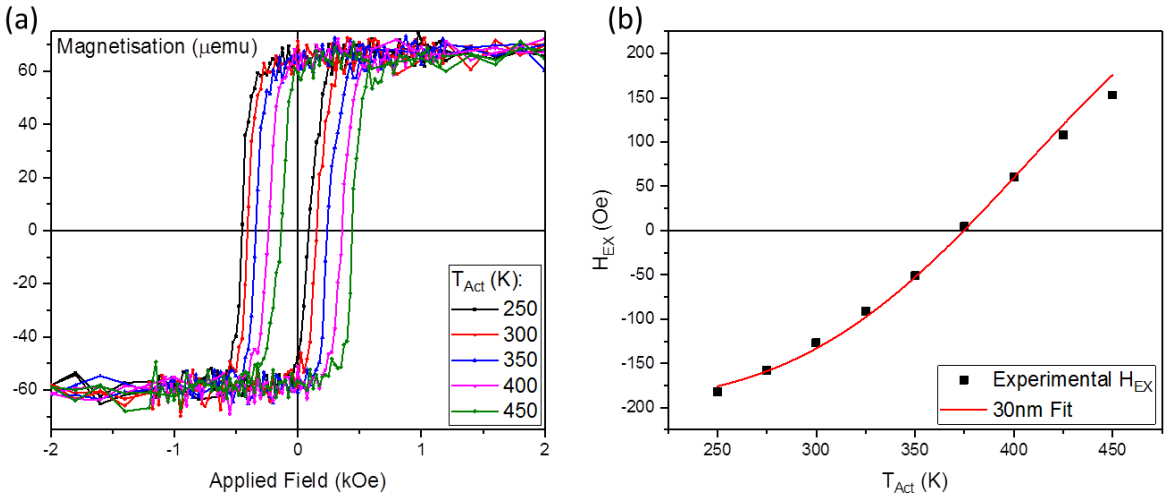

Figure 7.24 - Blocking data for sample produced using the HiTUS system: (a) Hysteresis loops measured at 200 K after setting at incrementally higher temperatures for 100 minutes (b) Summary of blocking data with calculated fit.

The fitting parameters used in Figure 7.24 (b) were as follows: $f_0 = 2.1 \times 10^6\ s^{-1}$ [99], $T_{NA} =$ 200 K, $T_N = 655$ K, $T_{set} = 450$ K, $D_m = 7.59$ nm, $\sigma = 0.26$, $t_{act} =$ 1800 s, $t_{set} = 6600$ s and $K_{AF} = 2.0 \times 10^6$ ergs/cm^3 . Even though this value of anisotropy is low compared to that of the films prepared using magnetron sputtering, the median blocking temperature obtained ($< T_B >$ = (374 ± 4) K) is higher due to the grain volume being 2.5 times larger than that in the samples prepared using magnetron sputtering.

The values obtained for the anisotropy constant for the small grain MnN prepared using magnetron sputtering are comparable to that of IrMn (2.9 x 10^7 ergs/cm^3 [108]). As demonstrated in this chapter, it is possible to produce 30 nm thick MnN films with the necessary thermal stability to allow integration into devices. Unfortunately, most current device applications require antiferromagnetic layer thicknesses below 10 nm. If it is possible to maintain the level of anisotropy measured in the 30 nm thick samples, whilst increasing the lateral grain size, it may be possible to reduce the layer thickness significantly. i.e. an 8.4nm lateral grain size in a 10 nm thick film would have an identical grain volume to that of the 30 nm thick film prepared using magnetron sputtering evaluated in this chapter. Overall, MnN shows potential as a novel antiferromagnetic material for the replacement of IrMn in existing device applications.

Chapter 8: Conclusions and Further Work

In this work, a variety of novel antiferromagnetic materials were investigated to assess their potential to replace the antiferromagnetic material IrMn in the field of spintronics. Initially several Heusler alloys were chosen for this application after a comprehensive review of existing literature. Thin film samples of the Heusler alloys Ni_2MnAl and Ru_2MnGe were prepared using both magnetron co-sputtering and the HiTUS deposition systems with researchers at partner institutions in the HARFIR project focussing on other Heusler alloy candidates.

To measure the Néel temperature of these materials, a sensitive, temperature-dependent, resistivity measurement technique was developed. This technique was based on the detection of the resistivity anomaly observed during the temperature driven magnetic phase change between antiferromagnetic and paramagnetic phases. The measurement technique developed was capable of detecting changes in resistance 6 orders of magnitude smaller than the total film resistance with temperature stability better than ± 0.1 K in the range 100 – 500 K. Preliminary measurement showed the determination of the Néel temperature in single crystal Cr was possible. The value obtained (T_N = (311 ± 3) K) agrees with values previously reported in the literature [42].

8.1 Conclusions

The first novel antiferromagnetic material investigated was Ni_2MnAl. Polycrystalline films were prepared using the HiTUS deposition system in York and epitaxial large grain samples were prepared using magnetron sputtering at Tohoku University. X-ray diffraction measurements showed crystallisation of the polycrystalline Ni_2MnAl samples after post-annealing at temperatures ≥ 673 K. Unfortunately no anomaly in the temperature-dependent resistivity was observed, this was attributed to the high intrinsic resistance of the polycrystalline films due to scattering at grain boundaries masking any variation in resistance due to magnetic phase changes. Magnetic measurements suggested partial formation of the fully ordered ferromagnetic $L2_1$ phase at higher post-annealing temperatures. When grown in contact with a 3 nm CoFe layer, no exchange bias was observed for any samples at

temperatures ≥ 100 K. These measurements did however display a substantial increase in coercivity that may be indicative of a low anisotropy antiferromagnet or intermixing of Ni_2MnAl and CoFe at the interface.

The epitaxial Ni_2MnAl samples grown on heated MgO substrates by magnetron sputtering crystallised readily with strong epitaxial texture. The presence of the B2 phase was confirmed using in-plane XRD, the absence of (111) diffraction peaks indicated no formation of the $L2_1$ phase. Using the electrical measurement technique developed, the Néel temperatures were found to vary between (264 ± 1) K and (282 ± 1) K dependent on deposition temperature. Similar to the polycrystalline samples, no exchange bias was observed when a CoFe layer was included in the sample structure at temperatures ≥ 100 K. Measurements performed on identical films by researchers at Tohoku University showed exchange bias values between 55 Oe and 11 Oe at 10 K suggesting the blocking temperature in this material is below 100 K. This low thermal stability of the antiferromagnetic B2 phase was explained by the low magnetocrystalline anisotropy of the material due to the cubic structure and the inter-atomic spin ordering in the (100) direction as shown in Figure 7.11.

Ru_2MnGe differs to Ni_2MnAl, in that it is predicted to be antiferromagnetic in its $L2_1$ structure with spin ordering in a sheet structure with the planes in the (111) direction. Films were prepared using the 2" BESTEC magnetron co-sputtering deposition system. A final composition of Ru = (50.0 ± 0.5), Mn = (25.1 ± 0.4) and Ge = (24.9 ± 0.2) was achieved after incremental refinement using XRF on films deposited on quartz glass substrates. Epitaxial samples were grown on heated MgO substrates with a lattice mismatch of 0.79% resulting in extremely high crystallinity and texture. Magnetic measurements indicated the resulting films were almost entirely thermally stable at 100 K allowing measurement of the median blocking temperature using the York Protocols for exchange bias. This resulted in a median blocking temperature of T_B = (126 ± 3) K.

These results show that it is possible to achieve stable antiferromagnetic order in Heusler alloys. What is interesting, is that the thermal stability of the exchange bias produced using these alloys is primarily dependent on their magnetocrystalline anisotropy, rather than their critical ordering temperature. Ni_2MnAl and Ru_2MnGe have comparable Néel temperatures (T_N = 313 K, 316 K respectively [141, 149]) however Ru_2MnGe displays significantly higher thermal stability due to the magnetocrystalline anisotropy present as a consequence of its

(111) sheet antiferromagnetic structure. Despite this, the blocking temperature obtained for Ru_2MnGe is too low to allow integration into spintronic devices.

After the discovery of the importance of magnetocrystalline anisotropy to the thermal stability of exchange bias, the focus of the project was shifted from Heusler alloys to MnN. Due to its tetragonal structure, MnN has a higher intrinsic anisotropy than cubic Heusler structures resulting in much higher thermal stability as initially demonstrated by Meinert et al. in 2015 [151]. A prototype sample was provided by Bielefeld University for evaluation of its thermal stability. The resulting measurements resulted in a median blocking temperature of T_B = (388 ± 2) K, which combined with the mean crystallite size obtained from Scherrer broadening, resulted in an estimate of the effective value of the anisotropy constant of $K_{AF} \cong 7 \times 10^4$ ergs/cm^3.

During this work polycrystalline MnN samples were deposited at room temperature using both magnetron sputtering and HiTUS deposition systems. The lateral grain size distribution in these films was measured using in-plane bright field TEM after sample thinning using mechanical polishing and FIB milling. The films prepared using magnetron sputtering were found to have a median grain size of (4.83 ± 0.04) nm while the films prepared using HiTUS had a grain size of (7.59 ± 0.09) nm resulting in a grain volume over twice as large in films with equal thickness.

X-ray diffraction measurements were used to determine the in and out of plane lattice constants of the MnN samples produced. For the samples produced with magnetron sputtering the mean c/a ratio was found to be 1.042 ± 0.005. Along with the crystallite size and lattice parameters, this was found to be invariant as a function of the antiferromagnet layer thickness. The samples produced using HiTUS were found to have a tetragonal distortion ratio of 1.019 ± 0.001 which was indicative of a lower magnetocrystalline anisotropy.

Before evaluating the thermal stability of exchange bias in the films, measurement parameters including the setting time, setting temperature and temperature of no activation were measured. The films produced using magnetron sputtering had a maximum setting temperature of 400 K before a decrease in the exchange bias was observed. This decrease is thought to be due to nitrogen desorption from the film. No decrease in exchange bias was observed at higher setting temperatures in the MnN films prepared using the HiTUS system. Interestingly, an increase was observed at T_{set} > 500 K however as this correlates with a

reduction in saturation magnetisation it is most likely due to a reduction in volume of the ferromagnetic CoFe layer due to intermixing.

The blocking temperatures of the MnN films prepared using magnetron sputtering showed an increase as a function of the thickness of the MnN layer. This trend was expected due to the increase in grain volume for thicker films. However, when the effective anisotropy constants were calculated, they were also found to increase with thickness. As no variation on the tetragonal distortion was observed for the samples, this variation must be due to a small change of stoichiometry which was not observed using XRD. The 30 nm thick MnN film produced using HiTUS had a higher blocking temperature than any of the films produced using magnetron sputtering, this was due to the grain volume in the film being over twice as large. Despite the higher blocking temperature, the effective anisotropy constant was around 3 times lower which is explained by reduction of the tetragonal distortion measured using XRD.

8.2 Future Work

The requirements for novel antiferromagnetic materials intended for integration into spintronic devices are now much better understood than they were prior to this work and the EU/JST HARFIR project. This work has shown that the Néel temperature cannot be used alone to predict the thermal stability of exchange bias, instead an emphasis should be placed on the magnetocrystalline anisotropy of the material. The Heusler alloys investigated in this work are unlikely to be used for any device applications due to their low thermal stability. The theoretical screening conducted by Balluff et al. has suggested a further 21 candidate Heusler alloys, of these, the alloys with spin ordering along the (111) planes and Néel temperatures above room temperature are worth further consideration.

The most obvious path forwards would be to select naturally anisotropic structures, however the number of antiferromagnetic tetragonal, orthorhombic or hexagonal materials is extremely limited. Further to this, it is not clear how antiferromagnetic order will arise in these structures. Given that magnetocrystalline anisotropy can be generated both by the magnetic spin arrangement and the structure within the material, another strategy would be to use DFT software packages such as CASTEP [216] or VASP [217] to calculate the potential anisotropy energy of candidate materials. At the time of writing, the complete origin of the effective anisotropy in IrMn and FeMn is still not understood. Hence a prerequisite to any

further work should attempt to understand the origin of the anisotropy in these materials before attempting to predict Néel temperatures and anisotropy constants in novel materials.

While MnN has limitations in its stability at higher temperatures, it has been shown to generate considerable exchange bias both in-plane and out of plane [218] and as such, continues to have significant potential for integration into devices. Currently the applications are somewhat limited due to the high antiferromagnet layer thicknesses required. Through control of the growth conditions it should be possible to reduce the layer thickness significantly by increasing the lateral grain size while maintaining or increasing the tetragonal distortion ratio.

Finally, despite years of endeavour both in York University and Spintec, Grenoble, it remains the case that the role of the interfacial spin structure is still not fully understood. Recent data (unpublished) using the IrMn/CoFe exchange bias system shows that the exchange bias observed at room temperature is increased by a factor of 50 % at 4.2 K. This indicates that the exchange stiffness at the interface is still low. There are ongoing studies to develop strategies to improve the exchange stiffness, hence it is likely that the exchange stiffness in any novel antiferromagnetic materials developed will need to be assessed and optimised.

List of Symbols

α – Lattice constant

α_s – Magnetron source tilt angle

$\alpha_1, \alpha_2, \alpha_3$ – Cosines of the angles of the magnetisation with the crystal axes

α_T – Temperature coefficient of resistance

β – X-Ray line broadening at half the maximum (FWHM) intensity

γ_m – Molecular field constant

ΔE – Energy barrier

Δe – Coupling energies

ϵ – Error

ϵ_{cry} – Crystal strain

θ – Diffraction angle

θ_{ea} – Angle between magnetisation and easy axis

2θ – Angle between incident and detector arms

θ_{ij} – Angle between spins

λ – Wavelength

μ_B – Bohr magneton

ρ – Resistivity

ρ_0 – Intrinsic Resistivity

ρ_T – Resistivity due to thermal or electron-phonon scattering

ρ_x – Resistivity due to impurities and dislocations

ρ_g – Resistivity due to grain boundary scattering

ρ_m – Resistivity due to magnetic scattering

σ_D – Standard distribution in the lognormal grain diameter

τ – Magnetic relaxation time

ϕ – In-plane detector angle

ϕ_f – Induced flux.

χ – Sample stage in plane rotation angle

χ_s – Susceptibility

χ_m – Mass susceptibility

ψ – Sample stage tilt perpendicular to $\theta/2\theta$ axis

ω – Sample stage tilt on $\theta/2\theta$ axis.

A_{AF} – Antiferromagnetic exchange stiffness

A_c – Detection coil area

A_s – Antiferromagnetic order saturation value

a – In plane lattice constant

B – Magnetic field

C – Curie Constant

c – Out of plane crystal lattice constant

D – Density

D_m – Median grain diameter

D_{cry} – Crystallite size

d_{hkl} – Crystal lattice spacing

d_{TS} – Distance between source and substrate in sputter deposition system

E – Energy

E_c – Critical energy activated at applied field H

E_K – Crystal anisotropy energy

e – Charge of an electron

e_a – Anisotropy energies

F_m – Force exerted on sample

f_0 – Oscillation attempt frequency

f_s – Dimensionless shape factor

$G(e_a, \Delta e)$ – Joint distribution function of the coupling and anisotropy energies

H – Applied / External field

H^* – Exchange field

H_K^* – Pseudo Anisotropy field

H_m – Molecular field

H_C – Coercivity

H_{EX} – Exchange bias

h – Planck's Constant

$\hbar$ - Reduced Planck's constant

$[hkl]$ – Miller indicies

J – Total angular momentum

J_1 – Exchange energy

J_2 – Perpendicular exchange energy

J_{ex} – Exchange integral

J_{int} – Interfacial exchange energy

K – Anisotropy constant

K_{AF} – Antiferromagnetic anisotropy constant

K_p, K_i, and K_d – Proportional, integral and derivative gains

K_u – Proportional gain value at which oscillations appear

k_B – Boltzmann constant

M – Magnetisation

M_R – Remanent magnetisation

M_s – Saturation magnetisation

m_e – Mass of the electron

$m(t)$ – Time-dependent surface moment

N – Charge Carrier density

N_{AF} – Number of antiferromagnetic grains

N_c – Number of coil turns

n – Diffraction order

P – Control variable

R – Resistance

r_{3d} – 3d electron shell radius

r_a – Atomic radius

$\mathrm{r_s}$ – Radius of maximum substrate size in sputter deposition system

S – Magnetic viscosity constant

S_i , S_j – Spin angular momentum

T – Temperature

T_0 – Temperature at which spontaneous magnetisation becomes 0 (Ordering parameter)

T_{act} – Activation temperature

T_B – Blocking temperature

T_C – Curie Temperature

T_{ms} – Measurement temperature

T_N – Néel Temperature

T_{NA} – Temperature at which no thermal activation occurs

T_{set} – Setting temperature

t – Time(s)

t_{AF} – Thickness of antiferromagnetic layer

t_{act} – Activation time

t_d – Derivative time constant

t_F – Thickness of ferromagnetic layer

t_i – Integral time constant

t_{ms} – Measurement time

t_{set} – Setting time

t_u – PID loop time period

V – Volume

V_F – Volume of ferromagnetic layer

v_F – Electron Fermi velocity

V_i – Induced voltage

x – Impurity concentration

z – Order of unity

List of Abbreviations

AC – Alternating Current

AF – Antiferromagnetic

AFLOW – Automatic FLOW for materials discovery

AFM – Atomic Force Microscopy

AGFM – Alternating Gradient Force Magnetometer

AMR – Anisotropic Magnetoresistance

BCC – Body Centred Cubic

CASTEP – Cambridge Serial Total Energy Package

DC – Direct Current

DFT – Density Functional Theory

DOS – Density of States

DRAM – Dynamic Random Access Memory

EDX – Energy Dispersive X-ray Spectroscopy

EU – European Union

F – Ferromagnetic

FCC – Face Centred Cubic

FCT – Face Centred Tetragonal

FIB – Focussed Ion Beam

FWHM – Full Width at Half Maximum

GMR – Giant Magnetoresistance

HARFIR – Heusler Alloy Replacement for Iridium

HCP – Hexagonal Close Packed

HDD – Hard Drive Disk

HiTUS – High Target Utilisation Sputtering

JST – Japan Science and Technology Agency

MBE – Molecular Beam Epitaxy

MOIF – Magneto-Optical Indicator Film

MR – Magnetoresistance

MRAM – Magnetic Random Access Memory

MTJ – Magnetic Tunnel Junction

NIST – National Institute of Standards and Technology

NTC – Negative Temperature Coefficient

PEEM – Photoemission Electron Microscopy

PID – Proportional, integral, derivative

PNR – Polarised Neutron Reflectometry

PRT – Platinum resistance thermometer

RA – Resistance Area

RKKY – Ruderman–Kittel–Kasuya–Yosida

RTD – Resistance temperature detector

SEM – Scanning Electron Microscope

STT – Spin Transfer Torque

TEM – Transmission Electron Microscopy

TM – Transition Metal

TMR – Tunnelling Magnetoresistance

UHV – Ultra-high Vacuum

VASP – Vienna Ab-initio Simulation Package

VBA – Visual Basic for Applications

VESTA – Visualisation for Electronic and Structural Analysis

VSM – Vibrating Sample Magnetometer

XAS – X-ray Absorption Spectra

XMCD – X-Ray Magnetic Circular Dichroism

XMLD – X-Ray Magnetic Linear Dichroism

XRD – X-ray Diffraction

XRF – X-Ray Florescence Spectroscopy

XRR – X-ray Reflectivity

YIG – Yttrium Iron Garnet

References

1. Baibich, M.N., et al., *Giant Magnetoresistance of (001)Fe/(001)Cr Magnetic Superlattices.* Physical Review Letters, 1988. **61**(21): p. 2472-2475.
2. Binasch, G., et al., *Enhanced magnetoresistance in layered magnetic structures with antiferromagnetic interlayer exchange.* Physical Review B, 1989. **39**(7): p. 4828-4830.
3. *European Comission Communication on the review of the list of critical raw materials for the EU.* 2017; Available from: https://ec.europa.eu/growth/sectors/raw-materials/specific-interest/critical_en.
4. Cullity, B.D. and C.D. Graham, *Introduction to magnetic materials*. 2011: John Wiley & Sons.
5. Ikeda, S., et al., *Tunnel magnetoresistance of 604% at 300 K by suppression of Ta diffusion in Co Fe B/ Mg O/ Co Fe B pseudo-spin-valves annealed at high temperature.* Applied Physics Letters, 2008. **93**(8): p. 082508.
6. Chappert, C., A. Fert, and F.N. Van Dau, *The emergence of spin electronics in data storage*, in *Nanoscience And Technology: A Collection of Reviews from Nature Journals*. 2010, World Scientific. p. 147-157.
7. Childress, J.R. and R.E. Fontana, *Magnetic recording read head sensor technology.* Comptes Rendus Physique, 2005. **6**(9): p. 997-1012.
8. Tehrani, S., et al., *Recent developments in magnetic tunnel junction MRAM.* IEEE Transactions on magnetics, 2000. **36**(5): p. 2752-2757.
9. *Iridium*, in *Encyclopædia Britannica*. 2016, Encyclopædia Britannica, inc.
10. InvestmentMine. [May, 2018]; Available from: http://www.infomine.com/investment/metal-prices/iridium/all/.
11. Schaller, R.R., *Moore's law: past, present and future.* IEEE Spectrum, 1997. **34**(6): p. 52-59.
12. Mark Re, Seagate Technology PLC, *HDD Areal Density*. 2015.
13. http://www.insic.org/news/2012Roadmap/12index.html. *Magnetic Storage Technology Roadmap*. 2012 [12/07/2018]; Available from: http://www.insic.org/news/2012Roadmap/12index.html.
14. Baltz, V., et al., *Antiferromagnetic spintronics.* Reviews of Modern Physics, 2018. **90**(1): p. 015005.
15. Graf, T., C. Felser, and S.S.P. Parkin, *Simple rules for the understanding of Heusler compounds.* Progress in Solid State Chemistry, 2011. **39**(1): p. 1-50.
16. Gokcen, N.A., *The Mn-N (Manganese-Nitrogen) system.* Bulletin of Alloy Phase Diagrams, 1990. **11**(1): p. 33.
17. Leineweber, A., et al., *The manganese nitrides η-MnN and θ-MnN: nuclear and magnetic structures.* Journal of Materials Chemistry, 2000. **10**(12): p. 2827-2834.

18. Suzuki, K., et al., *Neutron Diffraction Studies of the Compounds MnN and FeN.* Journal of the Physical Society of Japan, 2001. **70**(4): p. 1084-1089.

19. O'Handley, R.C., *Modern magnetic materials: principles and applications*. 2000: Wiley.

20. Néel, L., *Influence des fluctuations du champ moléculaire sur les propriétés magnétiques des corps.* Ann. Phys., 1932. **10**(18): p. 5-105.

21. Bizette, H., C. Squire, and B. Tsai, *The λ transition point of the magnetic susceptibility in the manganosite MnO.* Compt. rend, 1938. **207**: p. 449-450.

22. Shull, C.G. and J.S. Smart, *Detection of antiferromagnetism by neutron diffraction.* Physical review, 1949. **76**(8): p. 1256.

23. Meiklejohn, W.H. and C.P. Bean, *New Magnetic Anisotropy.* Physical Review, 1956. **102**(5): p. 1413-1414.

24. Meiklejohn, W.H. and C.P. Bean, *New magnetic anisotropy.* Physical Review, 1957. **105**(3): p. 904.

25. Dieny, B., *Giant magnetoresistance in spin-valve multilayers.* Journal of Magnetism and Magnetic Materials, 1994. **136**(3): p. 335-359.

26. Weiss, P., *Hypothesis of the molecular field and ferromagnetic properties.* J. phys, 1907. **6**(4): p. 661-690.

27. Heisenberg, W., *Zur theorie des ferromagnetismus.* Zeitschrift für Physik, 1928. **49**(9-10): p. 619-636.

28. Smart, L.E. and E.A. Moore, *Solid state chemistry: an introduction*. 2012: CRC press.

29. Weiss, P. and R. Forrer. *Aimantation et phénomène magnétocalorique du nickel*. in *Annales de Physique*. 1926. EDP Sciences.

30. Shull, C.G., W.A. Strauser, and E.O. Wollan, *Neutron Diffraction by Paramagnetic and Antiferromagnetic Substances.* Physical Review, 1951. **83**(2): p. 333-345.

31. Roth, W.L., *Multispin Axis Structures for Antiferromagnets.* Physical Review, 1958. **111**(3): p. 772-781.

32. Goodwin, A.L., et al., *Magnetic structure of MnO at 10 K from total neutron scattering data.* Physical review letters, 2006. **96**(4): p. 047209.

33. Sänger, I., et al., *Distribution of antiferromagnetic spin and twin domains in NiO.* Physical Review B, 2006. **74**(14): p. 144401.

34. Jauch, W., et al., *Crystallographic symmetry and magnetic structure of CoO.* Physical Review B, 2001. **64**(5): p. 052102.

35. Srinivasan, G. and M.S. Seehra, *Magnetic susceptibilities, their temperature variation, and exchange constants of NiO.* Physical Review B, 1984. **29**(11): p. 6295-6298.

36. Wang, S., W. Bailey, and C. Surgers, *Ion beam deposition and structural characterization of GMR spin valves.* IEEE transactions on magnetics, 1997. **33**(3): p. 2369-2374.

37. Seehra, M.S. and H.P.J. Wijn, *6.1.2.2 Mixed monoxides M1-pIMpIIO: Datasheet from Landolt-Börnstein - Group III Condensed Matter · Volume 27G: "Various Other Oxides" in SpringerMaterials,* Springer-Verlag Berlin Heidelberg.

38. Seike, T. and J. Nagai, *Electrochromism of 3d transition metal oxides.* Solar energy materials, 1991. **22**(2-3): p. 107-117.

39. Wang, C., et al., *Metal oxide gas sensors: sensitivity and influencing factors.* Sensors, 2010. **10**(3): p. 2088-2106.

40. Fawcett, E., *Spin-density-wave antiferromagnetism in chromium.* Reviews of Modern Physics, 1988. **60**(1): p. 209.

41. Marcus, P., S. Qiu, and V. Moruzzi, *The mechanism of antiferromagnetism in chromium.* Journal of Physics: Condensed Matter, 1998. **10**(29): p. 6541.

42. Koehler, W.C., et al., *Antiferromagnetism in Chromium Alloys. I. Neutron Diffraction.* Physical Review, 1966. **151**(2): p. 405-413.

43. Shull, C.G. and M.K. Wilkinson, *Neutron Diffraction Studies of Various Transition Elements.* Reviews of Modern Physics, 1953. **25**(1): p. 100-107.

44. Ishikawa, Y. and Y. Endoh, *Antiferromagnetism of γ-FeMn Alloys.* Journal of Applied Physics, 1968. **39**(2): p. 1318-1319.

45. Umebayashi, H. and Y. Ishikawa, *Antiferromagnetism of γ Fe-Mn alloys.* Journal of the Physical Society of Japan, 1966. **21**(7): p. 1281-1294.

46. Burkett, S., et al., *Effect of corrosion on magnetic properties for FeMn and NiO spin valves.* Journal of applied physics, 1997. **81**(8): p. 4912-4914.

47. Farrow, R.F.C., et al., *MnxPt1−x: A new exchange bias material for Permalloy.* Journal of Applied Physics, 1997. **81**(8): p. 4986-4988.

48. Pokhil, T., E. Linville, and S. Mao, *Exchange anisotropy and micromagnetic properties of PtMn/NiFe bilayers.* Journal of Applied Physics, 2001. **89**(11): p. 6588-6590.

49. Prejbeanu, I.L., et al., *Thermally assisted MRAM.* Journal of Physics: Condensed Matter, 2007. **19**(16): p. 165218.

50. Iwasaki, H., et al., *Excellent reliability of CoFe-IrMn spin valves.* IEEE Transactions on Magnetics, 1997. **33**(5): p. 2875-2877.

51. Szunyogh, L., et al., *Giant magnetic anisotropy of the bulk antiferromagnets IrMn and $IrMn_3$ from first principles.* Physical Review B, 2009. **79**(2): p. 020403.

52. Tomeno, I., et al., *Magnetic neutron scattering study of ordered Mn_3Ir.* Journal of applied physics, 1999. **86**(7): p. 3853-3856.

53. Sakuma, A., et al., *First-principles study of the magnetic structures of ordered and disordered Mn-Ir alloys.* Physical Review B, 2003. **67**(2): p. 024420.

54. Mitsumata, C., A. Sakuma, and K. Fukamichi, *Influence of the spin structure on the exchange bias of antiferromagnetic and ferromagnetic bilayer.* IEEE Transactions on Magnetics, 2003. **39**(5): p. 2738-2740.

55. Aley, N. and K. O'Grady, *Compositional dependence of antiferromagnetic anisotropy in IrMn/CoFe exchange bias systems.* Journal of Applied Physics, 2011. **109**(7): p. 07D719.

56. Tsunoda, M., et al., *L12 phase formation and giant exchange anisotropy in Mn3Ir/Co–Fe bilayers.* Journal of magnetism and magnetic materials, 2006. **304**(1): p. 55-59.

57. Emsley, J., *Nature's building blocks: an AZ guide to the elements*. 2011: Oxford University Press.

58. O'Grady, K., L. Fernandez-Outon, and G. Vallejo-Fernandez, *A new paradigm for exchange bias in polycrystalline thin films.* Journal of Magnetism and Magnetic materials, 2010. **322**(8): p. 883-899.

59. Grünberg, P., et al., *Layered magnetic structures: evidence for antiferromagnetic coupling of Fe layers across Cr interlayers.* Physical review letters, 1986. **57**(19): p. 2442.

60. Carbone, C. and S. Alvarado, *Antiparallel coupling between Fe layers separated by a Cr interlayer: dependence of the magnetization on the film thickness.* Physical Review B, 1987. **36**(4): p. 2433.

61. Heinrich, B., et al., *Ferromagnetic and antiferromagnetic exchange coupling in bcc epitaxial ultrathin Fe (001)/Cu (001) Fe (001) trilayers.* Physical review letters, 1990. **64**(6): p. 673.

62. Ruderman, M.A. and C. Kittel, *Indirect Exchange Coupling of Nuclear Magnetic Moments by Conduction Electrons.* Physical Review, 1954. **96**(1): p. 99-102.

63. Kasuya, T., *A Theory of Metallic Ferro- and Antiferromagnetism on Zener's Model.* Progress of Theoretical Physics, 1956. **16**(1): p. 45-57.

64. Yosida, K., *Magnetic Properties of Cu-Mn Alloys.* Physical Review, 1957. **106**(5): p. 893-898.

65. Parkin, S.S.P. and D. Mauri, *Spin engineering: Direct determination of the Ruderman-Kittel-Kasuya-Yosida far-field range function in ruthenium.* Physical Review B, 1991. **44**(13): p. 7131-7134.

66. Baibich, M.N., et al., *Giant magnetoresistance of (001) Fe/(001) Cr magnetic superlattices.* Physical review letters, 1988. **61**(21): p. 2472.

67. Binasch, G., et al., *Enhanced magnetoresistance in layered magnetic structures with antiferromagnetic interlayer exchange.* Physical review B, 1989. **39**(7): p. 4828.

68. Shiratsuchi, Y., et al., *Direct observations of ferromagnetic and antiferromagnetic domains in Pt/Co/Cr_2O_3/Pt perpendicular exchange biased film.* AIMS Materials Science, 2015. **2**(4): p. 484-496.

69. Arenholz, E., G. van der Laan, and F. Nolting, *Magnetic structure near the Co/NiO(001) interface.* Applied Physics Letters, 2008. **93**(16): p. 162506.

70. Chien, C.L., et al., *Hybrid domain walls and antiferromagnetic domains in exchange-coupled ferromagnet/antiferromagnet bilayers.* Physical Review B, 2003. **68**(1): p. 014418.

71. Berkowitz, A.E. and K. Takano, *Exchange anisotropy — a review.* Journal of Magnetism and Magnetic Materials, 1999. **200**(1–3): p. 552-570.

72. O'Grady, K., L.E. Fernandez-Outon, and G. Vallejo-Fernandez, *A new paradigm for exchange bias in polycrystalline thin films.* Journal of Magnetism and Magnetic Materials, 2010. **322**(8): p. 883-899.

73. Stiles, M.D. and R.D. McMichael, *Temperature dependence of exchange bias in polycrystalline ferromagnet-antiferromagnet bilayers.* Physical Review B, 1999. **60**(18): p. 12950-12956.

74. Vallejo-Fernandez, G., L.E. Fernandez-Outon, and K. O'Grady, *Measurement of the anisotropy constant of antiferromagnets in metallic polycrystalline exchange biased systems.* Applied Physics Letters, 2007. **91**(21): p. 212503.

75. Vallejo-Fernandez, G., B. Kaeswurm, and K. O'Grady, *Defect and impurity effects in exchange bias systems.* Journal of Applied Physics, 2011. **109**(7): p. 07D738.

76. Chantrell, R., et al., *Models of slow relaxation in particulate and thin film materials.* Journal of Applied Physics, 1994. **76**(10): p. 6407-6412.

77. Blomeier, S., et al., *Structural analysis of ion irradiated polycrystalline NiFe/FeMn exchange bias systems.* The European Physical Journal B - Condensed Matter and Complex Systems, 2005. **45**(2): p. 213-218.

78. Nowak, U., et al., *Domain state model for exchange bias. I. Theory.* Physical Review B, 2002. **66**(1): p. 014430.

79. Maissel, L.I. and R. Glang, *Handbook of thin film technology.* New York: McGraw-Hill, 1970, edited by Maissel, Leon I.; Glang, Reinhard, 1970.

80. Drude, P., *Zur Elektronentheorie der Metalle.* Annalen der Physik, 1900. **306**(3): p. 566-613.

81. Sommerfeld, A., *Zur elektronentheorie der metalle.* Naturwissenschaften, 1927. **15**(41): p. 825-832.

82. Mayadas, A.F. and M. Shatzkes, *Electrical-Resistivity Model for Polycrystalline Films: the Case of Arbitrary Reflection at External Surfaces.* Physical Review B, 1970. **1**(4): p. 1382-1389.

83. Mott, N.F., *The electrical conductivity of transition metals.* Proc. R. Soc. Lond. A, 1936. **153**(880): p. 699-717.

84. Grünberg, P., et al., *Layered Magnetic Structures: Evidence for Antiferromagnetic Coupling of Fe Layers across Cr Interlayers.* Physical Review Letters, 1986. **57**(19): p. 2442-2445.

85. Sarah, M.T., *The discovery, development and future of GMR: The Nobel Prize 2007.* Journal of Physics D: Applied Physics, 2008. **41**(9): p. 093001.

86. Néel, L., *Ferro-antiferromagnetic coupling in thin layers.* Ann Phys (Paris), 1967. **2**: p. 61-80.

87. Fulcomer, E. and S. Charap, *Thermal fluctuation aftereffect model for some systems with ferromagnetic-antiferromagnetic coupling.* Journal of Applied Physics, 1972. **43**(10): p. 4190-4199.

88. Mauri, D., et al., *Simple model for thin ferromagnetic films exchange coupled to an antiferromagnetic substrate.* Journal of Applied Physics, 1987. **62**(7): p. 3047-3049.

89. Malozemoff, A., *Random-field model of exchange anisotropy at rough ferromagnetic-antiferromagnetic interfaces.* Physical review B, 1987. **35**(7): p. 3679.

90. Koon, N.C., *Calculations of Exchange Bias in Thin Films with Ferromagnetic/Antiferromagnetic Interfaces.* Physical Review Letters, 1997. **78**(25): p. 4865-4868.

91. Stiles, M.D. and R.D. McMichael, *Model for exchange bias in polycrystalline ferromagnet-antiferromagnet bilayers.* Physical Review B, 1999. **59**(5): p. 3722-3733.

92. Stamps, R.L., *Mechanisms for exchange bias.* Journal of Physics D: Applied Physics, 2000. **33**(23): p. R247.

93. Nowak, U., A. Misra, and K.D. Usadel, *Domain state model for exchange bias.* Journal of Applied Physics, 2001. **89**(11): p. 7269-7271.

94. Nishioka, K., et al., *Grain size effect on ferro-antiferromagnetic coupling of NiFe/FeMn systems.* Journal of Applied Physics, 1996. **80**(8): p. 4528-4533.

95. Xi, H., *Theoretical study of the blocking temperature in polycrystalline exchange biased bilayers.* Journal of Magnetism and Magnetic Materials, 2005. **288**: p. 66-73.

96. Brown Jr, W.F., *Thermal fluctuations of a single-domain particle.* Physical Review, 1963. **130**(5): p. 1677.

97. Kneller, E., Proceedings of the International Conference on Magnetism, 1965: p. 174.

98. Dickson, D.P.E., et al., *Determination of f_0 for fine magnetic particles.* Journal of Magnetism and Magnetic Materials, 1993. **125**(3): p. 345-350.

99. Vallejo-Fernandez, G., et al., *Measurement of the attempt frequency in antiferromagnets.* Applied Physics Letters, 2010. **97**(22): p. 222505.

100. Stacey, F., *Thermally activated ferromagnetic domain wall motion.* Australian Journal of Physics, 1960. **13**: p. 599.

101. Street, R. and J.C. Woolley, *A Comparison of Magnetic Viscosity in Isotropic and Anisotropic High Coercivity Alloys.* Proceedings of the Physical Society. Section B, 1956. **69**(12): p. 1189.

102. Street, R. and J.C. Woolley, *A Study of Magnetic Viscosity.* Proceedings of the Physical Society. Section A, 1949. **62**(9): p. 562.

103. Gaunt, P., *Magnetic viscosity in ferromagnets.* The Philosophical Magazine: A Journal of Theoretical Experimental and Applied Physics, 1976. **34**(5): p. 775-780.

104. Vallejo-Fernandez, G., et al., *Control of the setting process in CoFe/IrMn exchange bias systems.* Journal of Applied Physics, 2008. **104**(3): p. 033906.

105. Aharoni, A., *Time dependence of magnetization decay in spin glasses.* Journal of Applied Physics, 1985. **57**(10): p. 4702-4705.

106. El-Hilo, M., K. O'Grady, and R.W. Chantrell, *The origin of non-linear ln(t) behaviour in the time dependence of magnetisation.* Journal of Magnetism and Magnetic Materials, 1992. **109**(2): p. L164-L168.

107. Fernandez-Outon, L.E., et al., *Interfacial spin order in exchange biased systems.* Journal of Applied Physics, 2008. **104**(9): p. 093907.

108. Aley, N., et al., *Texture effects in IrMn/CoFe exchange bias systems.* IEEE Transactions on Magnetics, 2008. **44**(11): p. 2820-2823.

109. Uyama, H., et al., *Effect of antiferromagnetic grain size on exchange-coupling field of $Cr_{70}Al_{30}/Fe_{19}Ni_{81}$ bilayers.* Applied Physics Letters, 1997. **71**(9): p. 1258-1260.

110. Vallejo-Fernandez, G., L. Fernandez-Outon, and K. O'Grady, *Antiferromagnetic grain volume effects in metallic polycrystalline exchange bias systems.* Journal of Physics D: Applied Physics, 2008. **41**(11): p. 112001.

111. Julliere, M., *Tunneling between ferromagnetic films.* Physics letters A, 1975. **54**(3): p. 225-226.

112. Fullerton, E.E. and I.K. Schuller, *The 2007 Nobel Prize in physics: Magnetism and transport at the nanoscale*. 2007, ACS Publications.

113. Sining, M., et al., *Commercial TMR heads for hard disk drives: characterization and extendibility at 300 gbit/in².* IEEE Transactions on Magnetics, 2006. **42**(2): p. 97-102.

114. Thomson, W., *W. Thomson, Proc. R. Soc. London 8, 546 (1857).* Proc. R. Soc. London, 1857. **8**: p. 546.

115. Dieny, B., et al., *Giant magnetoresistive in soft ferromagnetic multilayers.* Physical Review B, 1991. **43**(1): p. 1297.

116. Žutić, I., J. Fabian, and S. Das Sarma, *Spintronics: Fundamentals and applications.* Reviews of Modern Physics, 2004. **76**(2): p. 323-410.

117. Fert, A., et al., *The new era of spintronics.* Europhysics News, 2003. **34**(6): p. 227-229.

118. Chung, S.W., et al. *4Gbit density STT-MRAM using perpendicular MTJ realized with compact cell structure*. in *2016 IEEE International Electron Devices Meeting (IEDM)*. 2016.

119. Nguyen, V., et al. *Novel approach for nano-patterning magnetic tunnel junctions stacks at narrow pitch: A route towards high density STT-MRAM applications*. in *Electron Devices Meeting (IEDM), 2017 IEEE International*. 2017. IEEE.

120. Heusler, F., *F. Heusler, Verh. Dtsch. Phys. Ges. 5, 219 (1903).* Verh. Dtsch. Phys. Ges., 1903. **5**: p. 219.

121. Felser, C. and A. Hirohata, *Heusler Alloys*. 2015: Springer.

122. Balke, B., et al., *Rational design of new materials for spintronics: Co_2FeZ (Z= Al, Ga, Si, Ge).* Science and Technology of advanced Materials, 2008. **9**(1): p. 014102.

123. Graf, T., S.S. Parkin, and C. Felser, *Heusler compounds—A material class with exceptional properties.* IEEE Transactions on Magnetics, 2011. **47**(2): p. 367-373.

124. Acet, M., et al., *Coexisting ferro-and antiferromagnetism in Ni_2MnAl Heusler alloys.* Journal of applied physics, 2002. **92**(7): p. 3867-3871.

125. Yuya, S., et al., *Huge Spin-Polarization of $L_2$1 -Ordered Co_2MnSi Epitaxial Heusler Alloy Film.* Japanese Journal of Applied Physics, 2005. **44**(8L): p. L1100.

126. Kubota, T., et al., *Ferrimagnetism in epitaxially grown Mn_2VAl Heusler alloy investigated by means of soft x-ray magnetic circular dichroism.* Applied Physics Letters, 2009. **95**(22): p. 222503.

127. Winterlik, J., et al., *Ni-based superconductor: Heusler compound $ZrNi_2Ga$.* Physical Review B, 2008. **78**(18): p. 184506.

128. Antoni, P., M. Lluís, and A. Mehmet, *Magnetocaloric effect and its relation to shape-memory properties in ferromagnetic Heusler alloys.* Journal of Physics: Condensed Matter, 2009. **21**(23): p. 233201.

129. Li, C., J. Lian, and Q. Jiang, *Antiferromagnet topological insulators with AB_2C Heusler structure.* Physical Review B, 2011. **83**(23): p. 235125.

130. Krenke, T., et al., *Inverse magnetocaloric effect in ferromagnetic Ni–Mn–Sn alloys.* Nature materials, 2005. **4**(6): p. 450.

131. BAI, Z., et al., Data Storage: Review of Heusler Compounds. SPIN, 2012. **02**(04): p. 1230006.

132. Liu, H.-x., et al., *Giant tunneling magnetoresistance in epitaxial $Co_2MnSi/MgO/Co_2MnSi$ magnetic tunnel junctions by half-metallicity of Co_2MnSi and coherent tunneling.* Applied Physics Letters, 2012. **101**(13): p. 132418.

133. Miura, Y., K. Nagao, and M. Shirai, *Atomic disorder effects on half-metallicity of the full-Heusler alloys Co 2 ($Cr_{1-x}Fe_x$) Al: A first-principles study.* Physical Review B, 2004. **69**(14): p. 144413.

134. Picozzi, S., A. Continenza, and A.J. Freeman, *Role of structural defects on the half-metallic character of Co_2MnGe and Co_2MnSi Heusler alloys.* Physical Review B, 2004. **69**(9): p. 094423.

135. Slater, J.C., *The ferromagnetism of nickel. II. Temperature effects.* Physical Review, 1936. **49**(12): p. 931.

136. Pauling, L., *The nature of the interatomic forces in metals.* Physical Review, 1938. **54**(11): p. 899.

137. Kresse, G., *Software vasp, vienna, 1999;* Phys. Rev. B, 1996. **54**(11): p. 169.

138. Curtarolo, S., et al., *AFLOWLIB.ORG : A distributed materials properties repository from high-throughput ab initio calculations.* Computational Materials Science, 2012. **58**: p. 227-235.

139. Balluff, J., et al., *High-throughput screening for antiferromagnetic Heusler compounds using density functional theory.* Physical Review Materials, 2017. **1**(3): p. 034404.

140. Singh, D. and I. Mazin, *Electronic structure, local moments, and transport in Fe_2VAl.* Physical Review B, 1998. **57**(22): p. 14352.

141. Galanakis, I. and E. Şaşıoğlu, *Structural-induced antiferromagnetism in Mn-based full Heusler alloys: The case of Ni_2MnAl.* Applied physics letters, 2011. **98**(10): p. 102514.

142. Dong, X., et al., *Growth temperature controlled magnetism in molecular beam epitaxially grown Ni_2MnAl Heusler alloy.* Journal of crystal growth, 2003. **254**(3-4): p. 384-389.

143. Özdog, K. and I. Galanakis, *First-principles electronic and magnetic properties of the half-metallic antiferromagnet Cr_2MnSb.* Journal of Magnetism and Magnetic Materials, 2009. **321**(15): p. L34-L36.

144. Ishida, S., et al., *Magnetic and half-metallic properties of new Heusler alloys Ru_2MnZ (Z ・ Si, Ge, Sn and Sb).* Physica B: Condensed Matter, 1995. **210**(2): p. 140-148.

145. Fukatani, N., et al., *Structural and magnetic properties of antiferromagnetic Heusler Ru_2MnGe Epitaxial thin films.* Journal of the Korean Physical Society, 2013. **63**(3): p. 711-715.

146. Goldenberg, N., *Magnetism and valency: manganese compounds.* Transactions of the Faraday Society, 1940. **36**: p. 847-854.

147. Dong, X.Y., et al., *Growth temperature controlled magnetism in molecular beam epitaxially grown Ni_2MnAl Heusler alloy.* Journal of Crystal Growth, 2003. **254**(3): p. 384-389.

148. Acet, M., et al., *Coexisting ferro- and antiferromagnetism in Ni_2MnAl Heusler alloys.* Journal of Applied Physics, 2002. **92**(7): p. 3867-3871.

149. Kanomata, T., M. Kikuchi, and H. Yamauchi, *Magnetic properties of Heusler alloys Ru_2MnZ (Z= Si, Ge, Sn and Sb).* Journal of alloys and compounds, 2006. **414**(1-2): p. 1-7.

150. Wiener, G.W. and J.A. Berger, *Structure and magnetic properties of some transition metal nitrides.* JOM, 1955. **7**(2): p. 360-368.

151. Meinert, M., et al., *Large exchange bias in polycrystalline MnN/CoFe bilayers at room temperature.* Physical Review B, 2015. **92**(14): p. 144408.

152. Suzuki, K., et al., *Crystal structure and magnetic properties of the compound MnN.* Journal of Alloys and Compounds, 2000. **306**(1): p. 66-71.

153. Gokcen, N., *The Mn-N (manganese-nitrogen) system.* Bulletin of Alloy Phase Diagrams, 1990. **11**(1): p. 33.

154. Dunz, M., J. Schmalhorst, and M. Meinert, *Enhanced exchange bias in MnN/CoFe bilayers after high-temperature annealing.* AIP Advances, 2018. **8**(5): p. 056304.

155. Seagate, N.I.-P.c. 2016.

156. Bizette, H., *H. Bizette, CF Squire, and Tsai, Comptes rendus 207, 449 (1938).* Comptes rendus, 1938. **207**: p. 449.

157. Squires, G.L., *Introduction to the Theory of Thermal Neutron Scattering*. 1978: Courier Corporation.

158. Palenik, G.J., W.P. Jensen, and I.-H. Suh, *The history of molecular structure determination viewed through the Nobel prizes.* Journal of Chemical Education, 2003. **80**(7): p. 753.

159. Buffet, J., et al., *Advances in detectors for single crystal neutron diffraction.* Nuclear Instruments and Methods in Physics Research Section A: Accelerators, Spectrometers, Detectors and Associated Equipment, 2005. **554**(1-3): p. 392-405.

160. Ankner, J.F. and G.P. Felcher, *Polarized-neutron reflectometry.* Journal of Magnetism and Magnetic Materials, 1999. **200**(1): p. 741-754.

161. Leighton, C., et al., *Two-Stage Magnetization Reversal in Exchange Biased Bilayers.* Physical Review Letters, 2001. **86**(19): p. 4394-4397.

162. Fitzsimmons, M.R., et al., *Asymmetric Magnetization Reversal in Exchange-Biased Hysteresis Loops.* Physical Review Letters, 2000. **84**(17): p. 3986-3989.

163. Radu, F., et al., *Interfacial domain formation during magnetization reversal in exchange-biased CoO/Co bilayers.* Physical Review B, 2003. **67**(13): p. 134409.

164. Bergmann, A., et al., *Spin polarized neutron reflectivity measurements on Heusler [Co_2MnGe/V]n multilayers.* Superlattices and Microstructures, 2003. **34**(1): p. 137-143.

165. Bergmann, A., et al., *Antiferromagnetic dipolar ordering in Co_2MnGe multilayers.* Physical Review B, 2005. **72**(21): p. 214403.

166. Van der Pauw, L.J., *A method of measuring specific resistivity and Hall effect of discs of arbitrary shape.* Philips Res.Rep, 1958. **13**(1).

167. Bengt, S., *The Resistivity Anomaly in Chromium Near the Néel Temperature.* Physica Scripta, 1970. **2**(1-2): p. 53.

168. Hirohisa, S., et al., *Oxidization Characteristics of Some Standard Platinum Resistance Thermometers.* Japanese Journal of Applied Physics, 2008. **47**(10R): p. 8071.

169. Berry, R.J., *Effect of Pt Oxidation on Pt Resistance Thermometry.* Metrologia, 1980. **16**(3): p. 117.

170. Park, R.M.E., *Manual on the use of thermocouples in temperature measurement*. 1993, Philadelphia, PA: ASTM.

171. Steinhart, J.S. and S.R. Hart, *Calibration curves for thermistors.* Deep Sea Research and Oceanographic Abstracts, 1968. **15**(4): p. 497-503.

172. Franklin, G.F., *Feedback Control of Dynamic Systems*. 1993: Addison-Wesley Longman Publishing Co., Inc.

173. Ziegler, J.G. and N.B. Nichols, *Optimum Settings for Automatic Controllers.* Journal of Dynamic Systems, Measurement, and Control, 1993. **115**(2B): p. 220-222.

174. Ramadan, A.A., R.D. Gould, and A. Ashour, *On the Van der Pauw method of resistivity measurements.* Thin Solid Films, 1994. **239**(2): p. 272-275.

175. Koon, D.W., *Effect of contact size and placement, and of resistive inhomogeneities on van der Pauw measurements.* Review of Scientific Instruments, 1989. **60**(2): p. 271-274.

176. Schroder, D.K., *Resistivity*, in *Semiconductor Material and Device Characterization*. 2005, John Wiley & Sons, Inc. p. 1-59.

177. De Vries, J.W.C., *Temperature and thickness dependence of the resistivity of thin polycrystalline aluminium, cobalt, nickel, palladium, silver and gold films.* Thin Solid Films, 1988. **167**(1): p. 25-32.

178. Fuchs, K., *The conductivity of thin metallic films according to the electron theory of metals.* Mathematical Proceedings of the Cambridge Philosophical Society, 2008. **34**(1): p. 100-108.

179. Fischer, G., H. Hoffmann, and J. Vancea, *Mean free path and density of conductance electrons in platinum determined by the size effect in extremely thin films.* Physical Review B, 1980. **22**(12): p. 6065-6073.

180. Bridgman, P.W., *Compressibilities and Pressure Coefficients of Resistance of Elements, Compounds, and Alloys, Many of Them Anomalous.* Proceedings of the American Academy of Arts and Sciences, 1933. **68**(2): p. 27-93.

181. Corliss, L.M., J.M. Hastings, and R.J. Weiss, *Antiphase Antiferromagnetic Structure of Chromium.* Physical Review Letters, 1959. **3**(5): p. 211-212.

182. Wasa, K., *Handbook of Sputter Deposition Technology: Fundamentals and Applications for Functional Thin Films, Nano-Materials and MEMS*. 2012: Elsevier Science.

183. SemiCore. [23/10/2017]; Available from: http://www.semicore.com/what-is-sputtering.

184. BESTEC-GmbH, *User Manual v2013.05.27*.

185. Vopsaroiu, M., et al., *Novel sputtering-technology for grain-size control.* IEEE Transactions on Magnetics, 2004. **40**(4): p. 2443-2445.

186. Vopsaroiu, M., et al., *Grain size effects in metallic thin films prepared using a new sputtering technology.* Journal of optoelectronics and adavnced materials, 2005. **7**(5): p. 2713-2720.

187. Warren, B.E., *X-Ray Diffraction*. 2012: Dover Publications.

188. Culity, B.D. and S. Stock, *Elements of X-ray Diffraction*. 1978. 102.

189. Scherrer, P., *Bestimmung der Größe und der inneren Struktur von Kolloidteilchen mittels Röntgenstrahlen.* Nachrichten von der Gesellschaft der Wissenschaften zu Göttingen, Mathematisch-Physikalische Klasse, 1918.

190. Birkholz, M., *Thin Film Analysis by X-Ray Scattering : Techniques for Structural Characterization.* 2005.

191. Chu, X. and B.K. Tanner, *Double crystal x-ray rocking curves of multiple layer structures.* Semiconductor Science and Technology, 1987. **2**(12): p. 765.

192. Rigaku, *Thin Film Analysis Software: GlobalFit 2.0*. 2013.

193. Rigaku, *SmartLab Diffractometer User Manual (Second Edition)*. 2010.

194. Hammond, C., *The Basics of Crystallography and Diffraction*. 2015: OUP Oxford.

195. Lide, D.R., *CRC Handbook of Chemistry and Physics, 84th Edition*. 2003: Taylor & Francis.

196. Beckhoff, B., et al., *Handbook of Practical X-Ray Fluorescence Analysis*. 2007: Springer Berlin Heidelberg.

197. Williams, D.B. and C.B. Carter, *The transmission electron microscope*, in *Transmission electron microscopy*. 1996, Springer. p. 3-17.

198. Foner, S., *Vibrating Sample Magnetometer.* Review of Scientific Instruments, 1956. **27**(7): p. 548-548.

199. Microsense, *Model 10 v2 User Manual*

200. Grady, K.O., R.W. Chantrell, and I.L. Sanders, *Magnetic characterisation of thin film recording media.* IEEE Transactions on Magnetics, 1993. **29**(1): p. 286-291.

201. Weast, R.C. and M. Astle, *CRC.* Handbook of Chemistry and Physics. Boca Raton, Florida: Chemical Rubber Company Publishing. pp. E, 1984. **110**.

202. Zijlstra, H., *A Vibrating Reed Magnetometer for Microscopic Particles.* Review of Scientific Instruments, 1970. **41**(8): p. 1241-1243.

203. Flanders, P.J., *An alternating-gradient magnetometer (invited).* Journal of Applied Physics, 1988. **63**(8): p. 3940-3945.

204. Flanders, P.J., *A vertical force alternating-gradient magnetometer.* Review of Scientific Instruments, 1990. **61**(2): p. 839-847.

205. O'Grady, K., V.G. Lewis, and D.P.E. Dickson, *Alternating gradient force magnetometry: Applications and extension to low temperatures (invited).* Journal of Applied Physics, 1993. **73**(10): p. 5608-5613.

206. Tsuchiya, T., et al., *Exchange bias effects in Heusler alloy Ni2MnAl/Fe bilayers.* Journal of Physics D: Applied Physics, 2016. **49**(23): p. 235001.

207. Akulov, N.S., *Über das magnetische Quadrupolmoment des Eisenatoms.* Zeitschrift für Physik, 1929. **57**(3): p. 249-256.

208. Shima, H., et al., *Magnetocrystalline anisotropy energy in $L1_0$-type CoPt single crystals.* Journal of Magnetism and Magnetic Materials, 2005. **290-291**: p. 566-569.

209. Yingfan, X., W. Jian Ping, and S. Ying, *High coercivity CoCrPt-SiO_2 granular thin films for magnetic recording.* Journal of Physics D: Applied Physics, 2000. **33**(12): p. 1460.

210. Zou, J., et al., *High coercivity CoCrPt films achieved by post-deposition rapid thermal annealing.* Journal of Applied Physics, 2000. **87**(9): p. 6869-6871.

211. Mauri, D., et al., *Novel method for determining the anisotropy constant of MnFe in a NiFe/MnFe sandwich.* Journal of applied physics, 1987. **62**(7): p. 2929-2932.

212. Kato, T., et al., *Magnetic anisotropy of MBE grown $MnPt_3$ and $CrPt_3$ ordered alloy films.* Journal of Magnetism and Magnetic Materials, 2004. **272-276**: p. 778-779.

213. Yanes, R., et al., *Interfacial exchange interactions and magnetism of Ni_2MnAl bilayers.* Physical Review B, 2017. **96**(6): p. 064435.

214. Tabuchi, M., M. Takahashi, and F. Kanamaru, *Relation between the magnetic transition temperature and magnetic moment for manganese nitrides MnN_γ ($O < \gamma < 1$).* Journal of Alloys and Compounds, 1994. **210**(1): p. 143-148.

215. Choi, J.-G., H.J. Lee, and L.T. Thompson, *Temperature-programmed desorption of H2 from molybdenum nitride thin films.* 1994.

216. Segall, M., et al., *First-principles simulation: ideas, illustrations and the CASTEP code.* Journal of Physics: Condensed Matter, 2002. **14**(11): p. 2717.

217. Kresse, G. and J. Furthmüller, *Efficient iterative schemes for ab initio total-energy calculations using a plane-wave basis set.* Physical Review B, 1996. **54**(16): p. 11169-11186.

218. Zilske, P., et al., *Giant perpendicular exchange bias with antiferromagnetic MnN.* Applied Physics Letters, 2017. **110**(19): p. 192402.